THERMODYNAMIC OPTIMISATION AND EXPERIMENTAL COLLECTOR OF A DISH-MOUNTED SMALL-SCALE SOLAR THERMAL BRAYTON CYCLE

by

Willem Gabriel le Roux

Submitted in partial fulfilment of the requirements for the degree

PhD (Mechanical Engineering)

in the

Department of Mechanical and Aeronautical Engineering

Faculty of Engineering, Built Environment and Information Technology

UNIVERSITY OF PRETORIA

SOUTH AFRICA

2015

SUMMARY

THERMODYNAMIC OPTIMISATION AND EXPERIMENTAL COLLECTOR OF A DISH-MOUNTED SMALL-SCALE SOLAR THERMAL BRAYTON CYCLE

by

Willem Gabriel le Roux

The small-scale dish-mounted open solar thermal Brayton cycle (1-20 kW) with recuperator has an advantage in terms of cost and mobility and can offer an off-grid electricity solution to the people of the water-scarce southern Africa. South Africa has an advantage in terms of solar resource, but this solar resource is not used extensively due to high-cost and low-efficiency solar-to-electricity systems. The dish-mounted solar thermal Brayton cycle with recuperator offers a solution. However, heat losses and pressure losses in the cycle components can decrease the net power output of the system tremendously. In addition, the costs due to solar tracking and perfect dish optics can be high. The purpose of the study was to develop the small-scale (1-20 kW) dish-mounted open solar thermal Brayton cycle by optimising an open-cavity tubular solar receiver and counterflow plate-type recuperator with the method of total entropy generation minimisation. The optimised receiver was also tested in an experimental dish collector set-up. Modelling methods to predict the performance of the cycle and to optimise the solar receiver and recuperator were developed and tested so that the small-scale open solar thermal Brayton cycle could be developed further. SolTrace was used as ray-tracing method to determine the effects of inaccurate dish optics. An optimum concentration ratio of 0.0035 was identified for a collector with a maximum tracking error of

1° and an optical error of 10 mrad. It was shown that the open-cavity tubular solar receiver surface temperature and net heat transfer rate for heating air depended on the receiver size, mass flow rate through the receiver, receiver tube diameter, receiver inlet temperature and dish errors. Receiver efficiencies of between 43% and 70% were found for a receiver with mass flow rates of between 0.06 kg/s and 0.08 kg/s, tube diameters of between 0.05 m and 0.0833 m, air inlet temperatures of between 900 K and 1 070 K operating on a dish with 10 mrad optical error and maximum solar tracking error of 1°. With the use of Matlab and Flownex, it was shown that the small-scale open solar thermal Brayton cycle could generate a positive net power output with solar-to-mechanical efficiencies in the range of 10-20% with much room for improvement. The maximum receiver surface temperature was restricted to 1 200 K and the recuperator weight was restricted to 500 kg. An experimental set-up with a 4.8 m diameter parabolic dish with rim angle of 45° on a two-axis tracking system was constructed to test the receiver. An optimised open-cavity stainless steel tubular receiver with tube diameter of 88.9 mm was tested in the experiment. The experimental results showed the challenges regarding the design and construction of a solar thermal Brayton cycle collector. It was found that the insulation arrangement around the large receiver tube diameter influenced the heat loss due to convection and conduction. Results showed that with further research, the small-scale open solar thermal Brayton cycle could be a competitive small-scale solar energy solution to the people of South Africa.

ACKNOWLEDGEMENTS

_____

I thank God for good health and an injury-free research period.

JOURNAL PUBLICATIONS

_____

The following articles were published from this work:

1. Le Roux, W.G., Bello-Ochende, T., Meyer, J.P., 2011. Operating conditions of an open and direct solar thermal Brayton cycle with optimised cavity receiver and recuperator. *Energy*, Vol. 36, pp. 6027-6036.

2. Le Roux, W.G., Bello-Ochende, T., Meyer, J.P., 2012. Thermodynamic optimisation of the integrated design of a small-scale solar thermal Brayton cycle. *International Journal of Energy Research*, Vol. 36, pp. 1088-1104.

3. Le Roux, W.G., Bello-Ochende, T., Meyer, J.P., 2012. Optimum performance of the small-scale open and direct solar thermal Brayton cycle at various environmental conditions and constraints. *Energy*, Vol. 46, pp. 42-50.

4. Le Roux, W.G., Bello-Ochende, T., Meyer, J.P., 2013. A review on the thermodynamic optimisation and modelling of the solar thermal Brayton cycle. *Renewable and Sustainable Energy Reviews*, Vol. 28, pp. 677-690.

5. Le Roux, W.G., Bello-Ochende, T., Meyer, J.P., 2014. The efficiency of an open-cavity solar receiver for a small-scale solar thermal Brayton cycle. *Energy Conversion and Management*, Vol. 84, pp. 457-470.

PEER-REVIEWED CONFERENCE PAPERS

_____

The following papers were presented at conferences from this work:

1. Le Roux, W.G., Bello-Ochende, T., Meyer, J.P., 2011. Optimum performance of the small-scale open and direct solar thermal Brayton cycle at various environmental conditions and constraints. In: Proceedings of the International Green Energy Conference (IGEC-VI), 5-9 June, Eskisehir, Turkey.

2. Le Roux, W.G., Bello-Ochende, T., Meyer, J.P., 2011. Optimum operating conditions of the small-scale open and direct solar thermal Brayton cycle at various steady-state conditions. In: Proceedings of the 8th International Conference on Heat Transfer, Fluid Mechanics and Thermodynamics (HEFAT2011), 11-13 July, Mauritius.

3. Le Roux, W.G., Bello-Ochende, T., Meyer, J.P., 2011. Maximum net power output of the recuperative open and direct solar thermal Brayton cycle. In: Proceedings of the 5th International Conference on Energy Sustainability (ASME, ES 2011), 7-10 August, Washington, USA.

4. Le Roux, W.G., Bello-Ochende, T., Meyer, J.P., 2012. Optimum small-scale open and direct solar thermal Brayton cycle for Pretoria, South Africa. In: Proceedings of the 1st Southern African Solar Energy Conference (SASEC 2012), 21-23 May, Stellenbosch, South Africa.

5. Le Roux, W.G., Bello-Ochende, T., Meyer, J.P., 2012. Optimum small-scale open and direct solar thermal Brayton cycle for Pretoria, South Africa. In: Proceedings of the 6th International Conference on Energy Sustainability (ASME, ES 2012-91135), 23-26 July, San Diego, California, USA.

6. Le Roux, W.G., Mwesigye, A., Bello-Ochende, T., Meyer, J.P., 2014. Tracker and collector for an experimental setup of a small-scale solar thermal Brayton cycle. In: Proceedings of the 2nd Southern African Solar Energy Conference (SASEC 2014), 27-29 January, Port Elizabeth, South Africa.

7. Le Roux, W.G., Bello-Ochende, T., Meyer, J.P., 2014. Optimisation of an open rectangular cavity receiver and recuperator used in a small-scale solar thermal Brayton cycle with thermal losses. In: Proceedings of the 10th International Conference on Heat Transfer, Fluid Mechanics and Thermodynamics (HEFAT2014), 14-16 July 2014, Orlando, Florida, USA.

8. Le Roux, W.G., Meyer, J.P., Bello-Ochende, T., 2015. Experimental testing of a tubular cavity receiver for a small-scale solar thermal Brayton cycle (SASEC 2015), 11-13 May, Skukuza, Kruger National Park, South Africa.

TABLE OF CONTENTS

_____

LIST OF FIGURES

_____

xiv

LIST OF TABLES

_____

NOMENCLATURE

_____

a	Constant
a	Receiver aperture side length or recuperator channel width, m
A	Area, m^2
A'	Area ratio (A_{ap}/A_{conc})
b	Recuperator channel height, m
B	Constant
B	Function of Θ
BSR	Blade speed ratio
c	Specific heat, J/kgK
c_1	Constant used in linear equation
c_2	Constant used in linear equation
c_{p0}	Constant pressure specific heat, J/kgK
Cr	Capacity ratio
C_s	Gas velocity, m/s
d	Receiver tube diameter, m
D	Diameter, m
e	Specific exergy, J/kg
E	Constant
E	Exergy, J
f	Friction factor
f_c	Focal length, m
F	View factor
g	Gravitational constant, m/s^2
Gr	Grashof number
h	Specific enthalpy, J/kg
h	Heat transfer coefficient, W/m^{2}K
H	Recuperator height, m
H	Dish height, m
I	Direct normal solar irradiance, W/m^2
k	Gas constant (c_p / c_v)

k	Thermal conductivity, W/mK
K	Friction loss coefficient
L	Length, m
m	Mass of the receiver, kg
m_1	Slope of linear equation
m_2	Slope of linear equation
$\dot{m}$	Mass flow rate, kg/s
M	Mass of recuperator, kg
MT	Micro-turbine number
n	Number of recuperator flow channels in one direction
N	Number of tube sections
N	Speed, rpm
NTU	Number of transfer units
Nu	Nusselt number
P,p	Pressure, Pa
P	Net heat transfer rate at the receiver, W
Pr	Prandtl number
$\dot{q}$	Heat flux rate, W/m^2
Q	Heat transfer, W
$\dot{Q}$	Heat transfer rate, W
$\dot{Q}_{net}$	Net heat transfer rate, W
$\dot{Q}*$	Rate of available solar heat at receiver cavity, W
$\dot{Q}_{loss}$	Rate of heat loss, W
r	Pressure ratio
R	Gas constant, J/kgK
R	Thermal resistance, K/W
R	Dish radius
Ra	Raleigh number
Re	Reynolds number
S	Available solar power, W
S	Entropy, J/K
s	Specific entropy, J/kgK
$\dot{S}_{gen}$	Entropy generation rate, W/K

$\dot{S}$	Entropy rate, W/K
t	Thickness, m
t	Time, s
T	Temperature, K
$T*$	Apparent exergy source sun temperature, K
T_0	Environment temperature, K
T_s	Apparent blackbody temperature of the sun, K
U	Overall heat transfer coefficient, W/m^{2}K
U	Rotor inlet blade tip speed, m/s
V	Velocity, m/s
w	Wind constant
$\dot{W}$	Power, W
x	Distance in x-direction, m
X	Dimensionless position
y	Distance in y-direction, m
Z	Height, m

Greek symbols

β	Coefficient of volume expansion, 1/K
γ	Solar tracking error
δ	Error
ε	Heat exchanger effectiveness
ε	Emissivity of receiver
ε	Recuperator effectiveness
ζ	Dish slope
η	Efficiency
θ	Elevation of tracking system (sun's elevation from horizontal)
Θ	Dimensionless temperature difference
λ	Dimensionless parameter for longitudinal conduction
ν	Kinematic viscosity, m^2/s
ρ	Density, kg/m^3
σ	Stefan Boltzmann constant, W/m^{2}K^4
τ	Shadow displacement, m

υ	Volume, m^3
χ	Dimensionless external heat load
ψ_{rim}	Rim angle of the dish
ω	Error, mrad

Subscripts

0	Initial inlet to receiver
0	Surrounding/Loss
0	Zero pressure (ideal gas) for c_p
1 - 11	Refer to Fig. 2.1
1	At State 1
2	At State 2
2ndLaw	As determined with the second law of thermodynamics
∞	Environment
∞	Surrounding area/Free stream
a	Dead (reference) state
air	Of the air
ap	Receiver aperture
ave	Average
b	At heat transfer boundary
BC	Brayton cycle
BH	Bahnke and Howard
bottom	At the bottom
c	Based on the cold side
c	Compressor
cav	For the cavity
CF	Corrected flow
col	Overall for the collector
combined	Combined
conc	Concentrator
cond	Due to conduction
conv	Due to convection
cv	Control volume

D	Destruction
e	Exit
eff	Effective
f	Fluid
forced	Due to forced convection
gen	Generation
h	Based on the hot side
i	Inlet
in	At the inlet
inner	On the inside
ins	Insulation
j	Component number
L	Based on the length
l	Loss
loss	Loss into the environment
max	Maximum
min	Minimum
n	Tube section number
natural	Due to natural convection
net	Net
opt	Optimum
optical	Optical
out	At the outlet
outer	On the outside of the insulation
p	For constant pressure
prop	At which the properties are evaluated
r	Receiver
R	Reversible
rad	Due to radiation
REC	For the receiver including optical efficiency
rec	Receiver
refl	Due to concentrator reflectivity
reg	Recuperator

s	Surface
side	At the side
side1	At the sides of the receiver in parallel with the wind direction
side2	At the sides of the receiver normal to the wind direction
slope	Slope
solar	Direct normal irradiance from the sun
specularity	Specularity
STBC	Solar thermal Brayton cycle
t	Turbine
t	Time
top	At the top
total	Total
v	For constant volume

Superscripts:

*	Solar
.	Time rate of change
CH	Chemical

CHAPTER 1
INTRODUCTION

_____

1.1 Background

Solar power generation holds endless opportunities for the people of southern Africa. Figure 1.1 shows the long-term average direct normal irradiance of the sun on a world map (GeoModel Solar, 2014). Photovoltaic panels and solar water heaters are perhaps the most popular small-scale solar systems in South Africa at present.
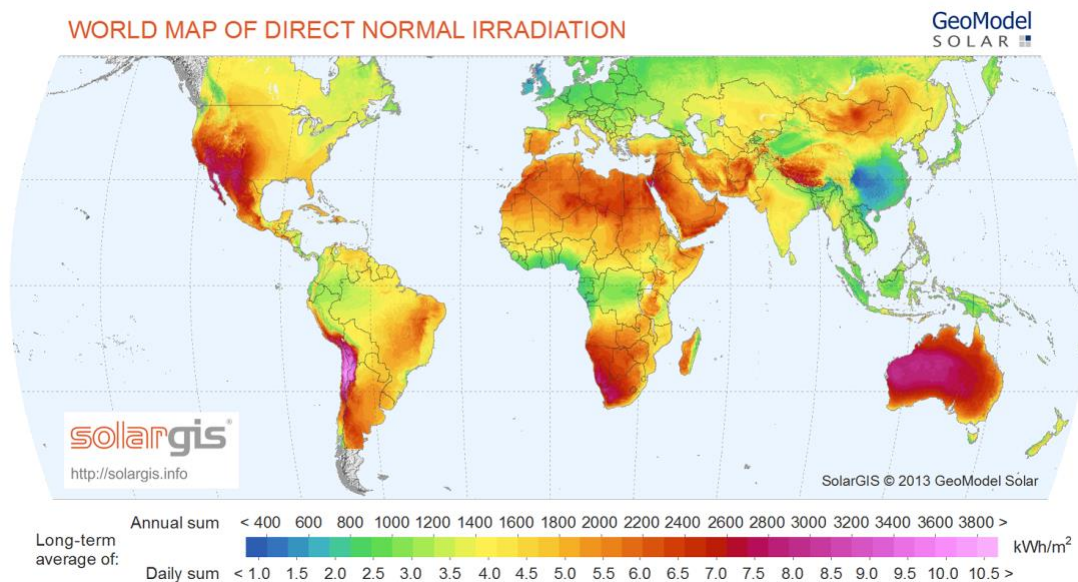
Figure 1.1 Long-term average of direct normal solar irradiance on a world map showing the potential of solar power generation in southern Africa (GeoModel Solar, 2014).

Concentrated solar power systems use the concentrated power of the sun from a heliostat field, reflective dish or a lens to increase the temperature of a fluid which can be used in a power cycle to generate electricity. Different types of solar thermal power cycles exist. The open solar thermal Brayton cycle uses air as working fluid, which makes this cycle very attractive for use in water-scarce countries, such as South Africa. In this cycle, air is heated in a solar receiver by concentrated solar power. The air is also the working fluid in the power cycle. The addition of a recuperator in the cycle allows for higher cycle efficiencies and a less complex receiver, which operates at lower pressure.

1

Figure 1.2 Parabolic dish concentrator for a Stirling engine (Image extracted from Pitz-Paal, 2007).

Figure 1.3 A typical micro-turbine (the GT1241) as available from Honeywell, Garrett proposed for the small-scale solar thermal Brayton cycle (Image extracted from Garrett, 2014).

According to Chen et al. (2007), the Brayton cycle is definitely worth studying when comparing its efficiency with those of other power cycles. Perhaps the most well-known small-scale dish-mounted solar power generation system currently is the Stirling engine (Fig. 1.2). Mills (2004) predicted that small-scale Brayton micro-turbines might become more popular due to high Stirling engine costs. An advantage of small-scale solar power generation systems is mobility, which means they can provide electricity for small communities with limited or no access to the national electricity grid. Small-scale systems also have cost benefits when manufactured in bulk. For a small-scale solar thermal Brayton cycle, various micro-turbines are already available off the shelf in South Africa thanks to the application of

2

micro-turbines as turbochargers in the stationary market, for example, those produced by Garrett (2014) (Fig. 1.3). The small-scale solar thermal Brayton cycle therefore has an advantage in terms of cost.

Many applications of the technology are yet to be discovered. The small-scale open solar thermal Brayton cycle can be supplemented with natural gas as a hybrid system so that it can either aid the micro-turbine cycle when solar radiation levels are low, or to act as the power source at night as envisioned for the 21st century by McDonald and Rodgers (2002). Storage systems such as packed rock bed thermal storage (Allen, 2010), cryogenic liquid air storage (Swift, 1993) and lithium fluoride storage (Cameron et al., 1972) can be coupled to the solar thermal Brayton cycle. With the use of ceramic materials, much higher operating temperatures could be reached in the future, which would further increase the efficiency of the solar thermal Brayton cycle. The rotating shaft of the solar thermal Brayton cycle can also be used for any power application, not only for electricity generation. A hidden advantage of the open solar thermal Brayton cycle is that the hot exhaust air coming from the recuperator can be close to 100 °C. This heat can be used to heat water or to run an absorption chiller. When this heat is utilised, it makes the system very efficient and highly competitive.

1.2 Literature

The Brayton cycle and the optimisation thereof have been studied by many authors; however, not many have studied the solar thermal Brayton cycle. Zhang et al. (2007), for example, studied the performance of a closed solar thermal Brayton cycle without a recuperator. Very few authors have done exergy analysis and entropy generation minimisation of specifically the open solar thermal Brayton cycle with recuperator. This was done, for example, by Jubeh (2005) and Le Roux et al. (2011).

To obtain the maximum net power output of the open solar thermal Brayton cycle with recuperator, a combined effort of heat transfer, fluid mechanics and thermodynamic thought is required. Bejan (1982a) suggests that the method of entropy generation minimisation combines these thoughts. Various studies such as Bejan et al. (1996) have emphasised the importance of the optimisation of the global performance of a system, instead of optimising components individually. Many different solar receivers and recuperators have been designed and optimised individually for the Brayton cycle and the solar thermal Brayton cycle. These include more recent studies by Stevens and Baelmans (2008), Hischier et al. (2009) and Neber and Lee (2012). The operation of a dish-mounted solar thermal Brayton cycle receiver

3

can be studied with computer software and algorithms as described by Ho (2008) and Bode and Gauché (2012).

There is an ongoing search to achieve higher air temperatures and higher efficiencies in a solar receiver. Significant contributions are being made by the DLR (German Aerospace Centre), the Weizmann Institute of Science, the NREL (National Renewable Energy Laboratory) and Sandia National Laboratories, to name but a few.

1.3 Problem

More than three quarters of South Africa's primary energy needs are currently provided by coal, according to South Africa's Department of Energy (DoE, 2014). Fluri (2009) shows that transmission lines have to cross vast stretches of land to bring electricity to isolated areas. More efficient and cost-effective small-scale solar-to-electricity technologies are required to make solar power more competitive so that all South Africans can harness their solar resource. Thus far, the world's solar leaders are not necessarily the sunniest countries, but rather the ones that can afford to pay extra for solar power (Johnson, 2009). The small-scale (1-20 kW) dish-mounted open solar thermal Brayton cycle with recuperator as a cost-effective solution for the people of South Africa should be developed further. The solar dish can dictate the majority of the total cost of a dish-mounted solar thermal Brayton cycle, where the more accurate the optics of the dish, the more expensive it becomes. Solar thermal cycles are often tested in a laboratory and the errors due to solar concentration are neglected. The effects of optical errors on the performance of a dish-mounted solar thermal Brayton cycle receiver should be investigated. When designing a system such as a small-scale open solar thermal Brayton cycle, there is always a compromise between allowing effective heat transfer and keeping pressure losses in the components small. Many studies have been published on the components needed in a typical solar thermal Brayton cycle and their optimisation, although these components are often optimised individually and not as part of a whole system with system performance as objective function.

1.4 Purpose of the study

The small-scale (1-20 kW) dish-mounted open solar thermal Brayton cycle has not been studied before and this study aims to develop the technology further. The purpose of the study is to develop the small-scale dish-mounted open solar thermal Brayton cycle by optimising its solar receiver and recuperator with the method of total entropy generation minimisation and to test the optimised receiver.

4

1.5 Objectives

The objective of the study is to apply the second law of thermodynamics, entropy generation minimisation and ray-tracing software to optimise the geometries of an open-cavity tubular receiver and a plate-type recuperator in a small-scale dish-mounted open solar thermal Brayton cycle such that the system produces maximum net power output at steady state. Simplicity and cost are deciding factors in the study. Modelling methods to predict the performance and to optimise the system are developed and tested. The optimised solar receiver is tested on an experimental solar dish to determine the convection heat transfer coefficient in the cavity receiver. The work investigates and includes the challenges and errors associated with the dish concentrator. The maximum allowable tracking error and concentration ratio are determined.

1.6 Scope

Thermodynamic optimisation is used to optimise the dish-mounted small-scale open solar thermal Brayton cycle in the 1-20 kW range. Off-the-shelf micro-turbines (Garrett, 2014) in this range are considered and chosen for low cost, high availability and reliability. The optimum geometries of a stainless steel open-cavity tubular receiver and stainless steel counterflow plate-type recuperator are optimised for a system with a 4.8 m diameter parabolic solar dish with 45° rim angle. A maximum receiver surface temperature of 1 200 K and a maximum recuperator weight of 500 kg are considered. SolTrace is used as ray-tracing software. The optimised solar receiver is tested on an experimental parabolic solar dish with diameter of 4.8 m, 45° rim angle and two-axis solar tracking.

1.7 Overview of the thesis

A literature study regarding the components of the small-scale dish-mounted open solar thermal Brayton cycle is given in Chapter 2 with an emphasis on the importance of the optimisation of components for a common goal. In Chapter 3, the modelling and optimisation of the receiver, recuperator and micro-turbine in the cycle are discussed. The analytical and optimisation results of models developed in Chapter 3 are shown in Chapter 4 together with numerical results. The testing of the optimised tubular solar cavity receiver on an experimental set-up is presented in Chapter 5, whereafter the concluding remarks are made in Chapter 6.

5

CHAPTER 2
LITERATURE STUDY

_____

2.1 Introduction

In this work, a small-scale receiver for a small-scale open solar thermal Brayton cycle is required. The accuracy of the dish and tracking system used is often an important factor in the total cost of the system. Since the development of the solar thermal Brayton cycle in the 1960s, many attempts have been made to improve the efficiency of the cycle and the solar receiver. A high solar receiver efficiency, however, does not necessarily mean that the receiver will perform well in a solar thermal Brayton cycle. A literature study is conducted to identify the different attempts of optimisation, modelling and development of the solar thermal Brayton cycle and its components. Different solar receiver and recuperator designs are investigated in the study. The importance of the optimisation of components for a common goal is emphasised. Optimisation using the method of total entropy generation minimisation is shown to be a holistic optimisation approach.

2.2 Solar thermal Brayton cycle

The closed Brayton cycle was developed in the 1930s for power applications, according to Pietsch and Brandes (1989). The technology was adapted to the design and development of solar thermal Brayton cycles for space power in the 1960s, with the success of lightweight and high-performance gas turbines for aircraft. According to Pietsch and Brandes (1989), experimental testing of the solar thermal Brayton cycle proved high reliability and efficiencies above 30% with turbine inlet temperatures of between 1 033 K and 1 144 K. Dickey (2011) also presented experimental test results of a solar thermal Brayton cycle (20-100 kW), an initiative from HelioFocus Ltd. and Capstone Microturbine at the Weizmann Institute. A proprietary pressurised volumetric solar receiver was used in the experiment. A system efficiency of 11.76% was achieved with turbine inlet temperature of 1 144 K. The system generated 24.04 kW of electricity with the micro-turbine spinning at 96 000 rpm.

The open and direct solar thermal Brayton cycle with recuperator, which is studied in this work, is shown in Fig. 2.1. The parabolic dish concentrator is used to reflect and concentrate the sun's rays onto the receiver aperture so that the solar heat can be absorbed by the inner walls of the receiver. The heat is then transferred to the working fluid, which is air. The

6

compressor increases the air pressure before the air is heated in the receiver. The compressed and heated air expands in the turbine, which produces rotational power for the compressor and the electric load.
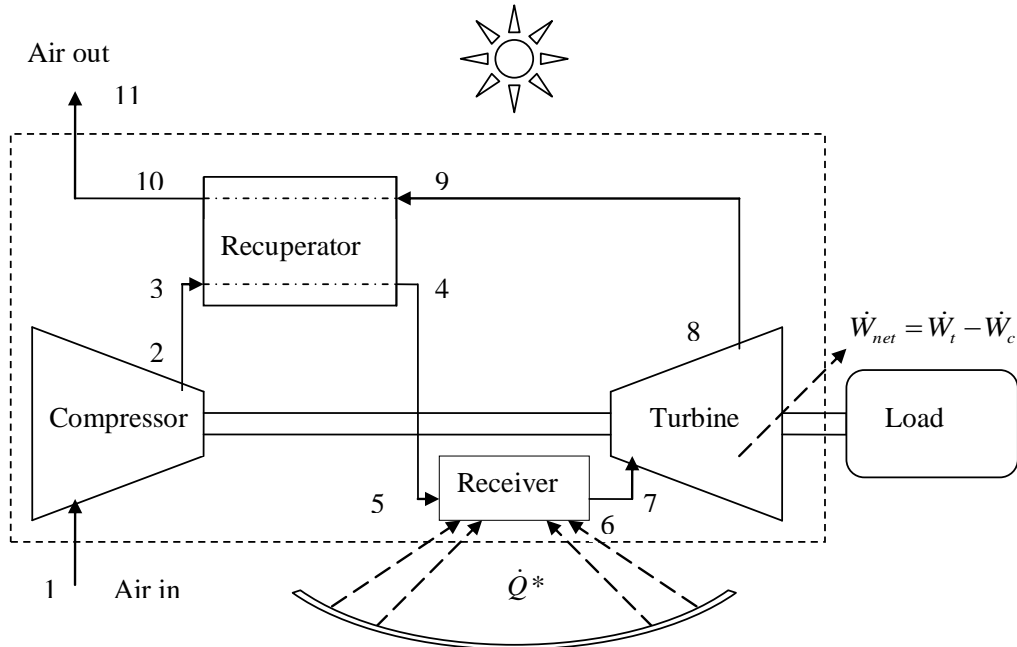
Figure 2.1 The open and direct solar thermal Brayton cycle.
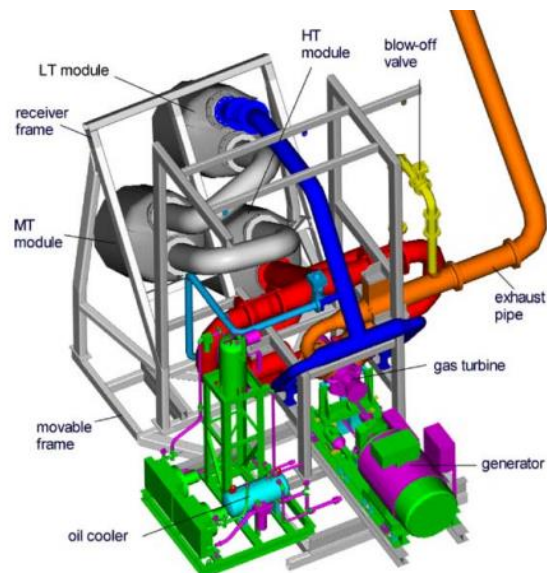
Figure 2.2 Test set-up of a solar thermal Brayton cycle (Image extracted from Heller et al., 2006).

A micro-turbine's air compressor, turbine and generator are usually mounted on a single shaft and all spin at the same rate (Willis and Scott, 2000; Shiraishi and Ono, 2007). It is simple,

7

robust and easy to maintain. According to Willis and Scott (2000), the generator also operates as the starter motor, running off battery power to bring the turbine up to speed to begin operation. This eliminates the need for a separate starter and simplifies design. According to Willis and Scott (2000), micro-turbines use a high-rpm DC generator coupled to a DC-AC power converter with efficiency of 96% to 97% mechanical to electrical DC.

A test set-up of an open solar thermal Brayton cycle without a recuperator is shown in Fig. 2.2, tested by Heller et al. (2006). In the recuperator, hot exhaust air preheats the colder air before it enters the receiver. According to Pietsch and Brandes (1989), high recuperator effectiveness is mostly chosen to maximise efficiency. The recuperator in the cycle assists the receiver in heating the air from ambient temperature. A recuperated solar thermal Brayton cycle allows for lower compressor pressure ratios, higher efficiency and a less complex solar receiver. The highest-efficiency Brayton cycles are recuperative cycles with low compressor pressure ratios. If recuperation is not used, high compressor pressure ratios are required to provide high efficiency (Stine and Harrigan, 1985).

According to Mills (2004), solarised Brayton micro-turbines are adapted from the small stationary gas turbine market, which allows for lower costs due to high production quantities in this market. Chen et al. (2007) showed that the Brayton cycle is definitely worth studying when comparing its efficiency with that of other power cycles. The efficiency of a closed recuperative solar thermal Brayton cycle with helium as working fluid has also been analysed thermodynamically by Gandhidasan (1993). An open solar thermal Brayton cycle uses air as working fluid, which makes this cycle very attractive for use in water-scarce countries. Bejan et al. (1996) state that the solar heat source is more suitable than the isotope and nuclear heat sources when the power plant size is in the range of 2-100 kW.

A solar receiver might be designed for high efficiency; however, when coupled to a Brayton cycle, it might not perform well, due to it not being optimised to achieve a common goal together with the other components. The importance of optimising the components of the solar thermal Brayton cycle for a common goal is emphasised in this work.

2.3 Solar collector

For large-scale systems, a heliostat field is typically used to focus the sun's rays onto a receiver. For the small-scale solar thermal Brayton cycle, however, a solar dish can be used to track the sun and to reflect the solar radiation onto the receiver. A solar dish is thus considered in this work as it is more practical for a small-scale set-up. A solar dish, however, has its own problems and limitations as discussed in this section. When a dish with a specific

8

diameter, focal length and rim angle is used to focus the sun's rays onto a receiver, the net rate of heat absorbed by the working fluid in the receiver depends, among others, on the aperture diameter of the receiver. Due to the sun's rays not being truly parallel and due to concentrator errors, the reflected rays from the dish form an image of finite size centred on its focal point. The aperture area of the solar receiver will determine the amount of intercepted heat, but also the amount of heat lost due to convection and radiation. The larger the cavity aperture, the more heat can be lost due to convection and radiation but also, the more heat can be intercepted. For a fixed dish concentrator area, the amount of heat available for the working fluid, which is the intercepted heat minus the heat lost due to radiation, convection and conduction, is a function of the cavity aperture diameter. The receiver aperture area can thus be sized optimally for a fixed dish concentrator area. For example, Stine and Harrigan (1985) presented such a receiver-sizing algorithm.

The factors contributing to the temperature profile and net heat transfer rate on the receiver wall can be divided into two components: geometry-dependent and temperature-dependent. The geometry-dependent factors include the concentrator dish with its optics: tracking error, specularity error, slope error, reflectance, spillage and shadowing. For a specific ratio of receiver aperture area versus concentrator area, A', the solar heat flux available at the different wall positions in the open-cavity receiver can be determined, irrespective of receiver temperature. The temperature-dependent factors include radiation heat loss to the environment, re-radiation from the inner-cavity walls, convection heat loss and conduction heat loss. These factors depend on the surface temperatures at the different parts of the receiver.

2.3.1 Solar tracking error

Two-axis solar tracking is required to ensure that the sun's rays stay focused on the receiver aperture throughout a typical day. Typical solar tracking errors of $0.1° – 0.3°$ (Helwa et al., 2000), $0.2°$ (Brooks, 2005), $0.4°$ (Naidoo and Van Niekerk, 2011), $0.6° – 0.7°$ (Chong and Wong, 2009), less than $1°$ (Al-Naima and Yaghobian, 1990), $1°$ (Argeseanu et al., 2009) and $±1° - 2°$ commercially (Stafford et al., 2009) were identified. Error due to wind loading is also a measurable quantity (Stafford et al., 2009). The accuracy of the tracking system is often an important factor in the total cost of a system. It is also important to note that this accuracy is much dependent on sensor alignment, base-level alignment, momentum of the moving dish and also, according to Stine and Harrigan (1983), drive non-uniformity and receiver alignment. Pattanasethanon (2010) describes the use of a digital solar positioning

9

sensor for solar tracking. In his work, a phototransistor configuration with screens and shades was employed as a detector of solar beam radiation. The height of the screen determined the sensitivity operation or period of tracking in the solar tracker.

During the research period, the author developed a simple and cost-effective tracking sensor based on the screens and shades idea described by Pattanasethanon (2010). This sensor is described in detail in Le Roux et al. (2014a). Figure 2.3 shows the measured azimuth angle versus the real angle determined from SunEarthTools (2014) as a function of time while testing and adjusting the sensitivity of the sensor during a sunny day. The tracking error found was mostly a lagging error. It was found that the tracking error can be decreased by either increasing the height of the wall, increasing the input voltage of the sensor or increasing the distance between sensors. It was also found that it is important to have the azimuth axis aligned to be parallel with the zenith axis, as was also noted by Chong and Wong (2009).
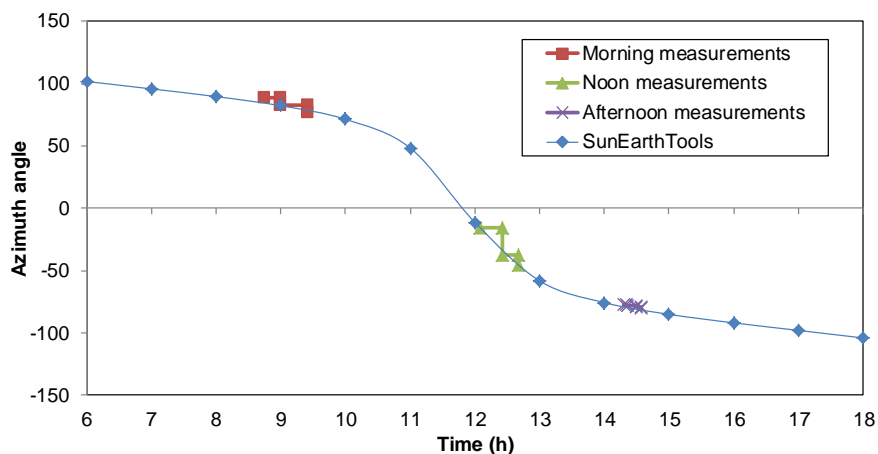
Figure 2.3 Measured angle of tracking system versus real azimuth angle of the sun.

From Le Roux et al. (2014a), it was concluded that it would be possible to get the sensor to operate within 2° tracking accuracy. This accuracy compares well with commercial trackers.

2.3.2 Reflectance, slope error and specularity error

A concentrator dish has to reflect the sun's rays onto the receiver. The rim angle of the parabolic dish determines where its focal point is. Dish manufacturing and installation errors can change the position of the focal point. For a solar concentrator, good reflectance and specular reflection of the entire terrestrial solar spectrum are important (Janecek and Moses, 2008; BASF, 2007; Stine and Harrigan, 1985). According to Janecek and Moses (2008),

10

specular (mirror-like) reflection occurs when a surface is very smooth. Good reflectivity does not mean that a material has specular reflectivity. For example, titanium dioxide paint has very good reflectivity but it has diffuse reflection. Diffuse reflection is produced from rough surfaces and is characterised by the light being reflected through a broad distribution of angles. According to Stine and Harrigan (1985) and BASF (2007), not all materials exhibiting high specular reflectance reflect equally well at all wavelengths.
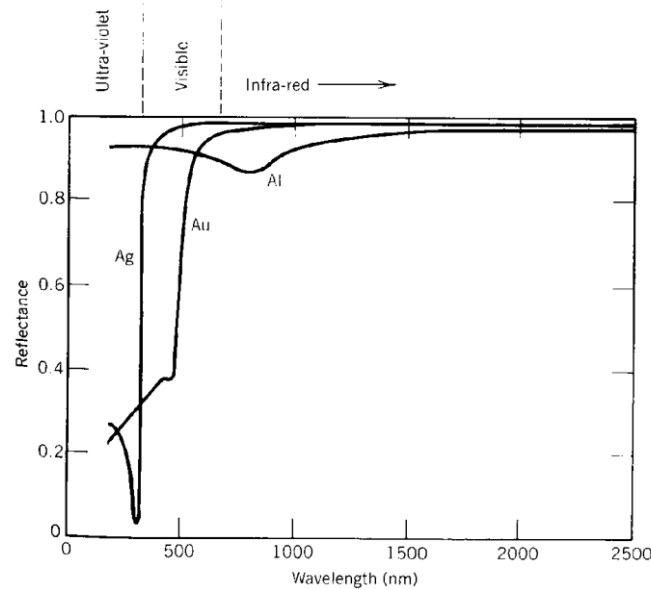
Figure 2.4 Specular reflectance of silver, aluminium and gold (Image extracted from Stine and Harrigan, 1985).

Figure 2.4 shows the specular reflectance of several materials as a function of wavelength over the solar radiation spectrum (Stine and Harrigan, 1985). According to Stine and Harrigan (1985), polished aluminium is a good material with its 91% specular reflectance. According to Paul Schertz et al. (1991), the reflectivity of mill-finished aluminium is about 55%. According to Stine and Harrigan (1985), the specular reflectance of any material is a function of time, regardless of the reflector (Fig. 2.5).

According to Stine and Harrigan (1985), a typical total effective collector error is 6.7 mrad. According to Grossman et al. (1991), a typical slope error for a stretched membrane dish is abount 3 mrad. Typical slope errors are 1.75, 3 and 5 mrad, while specularity errors range between 0 and 3.84 mrad (Gee et al., 2010). According to SolarPaces (2011), 3 mrad is a typically acceptable value for a specularity error of a parabolic trough mirror material.

11
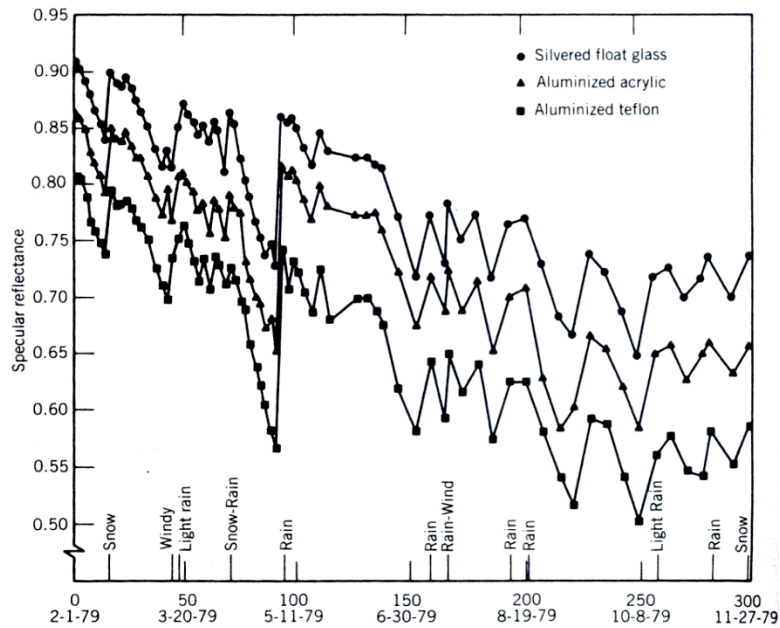
Figure 2.5 Specular reflectance of reflectors as a function of time (Image extracted from Stine and Harrigan, 1985).

2.3.3 Modelling the collector

Computer software and algorithms as described by Ho (2008) and Bode and Gauché (2012) are available to compute the solar heat flux on a receiver as reflected from a reflector. SolTrace is a software tool developed at the National Renewable Energy Laboratory (NREL) to model concentrating solar power optical systems and analyse their performance. SolTrace is recommended by Bode and Gauché (2012) as a free and readily available plant performance code for solar receiver research. The geometry-dependent factors contributing to the temperature profile and net heat transfer rate on the receiver wall include the concentrator dish with its optics: tracking error, specularity error, slope error, reflectance, spillage and shadowing. The effects of these factors can be found with SolTrace.

2.3.4 Constructing the collector

A parabolic profile is often used for a solar concentrator as shown in Fig. 2.6. A rim angle of 45° is paramount for concentrators with focal plane receivers (Stine and Harrigan, 1985). According to Stine and Harrigan (1985), the aperture area of a parabolic dish is defined by Eq. (2.1).

12

$$A_s = 4\pi f_c^2 \frac{\sin^2 \psi_{rim}}{\left(1 + \cos \psi_{rim}\right)^2}$$

(2.1)

Thus, the focal length can be calculated with Eq. (2.2).

$$f_c = \sqrt{\frac{\left(1 + \cos \psi_{rim}\right)^2 \pi R^2}{4\pi \sin^2 \psi_{rim}}}$$

(2.2)
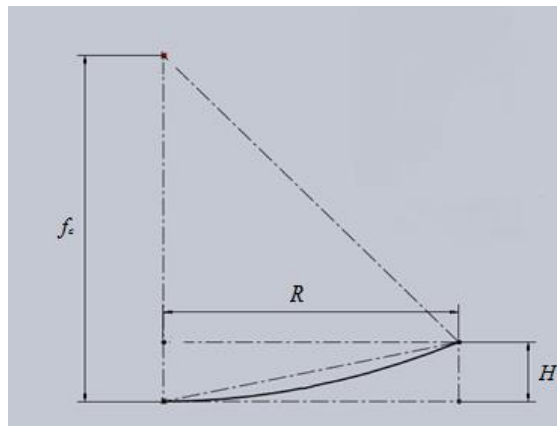
Figure 2.6 The parabolic shape of the concentrator dish segment.

For a parabola, $y = ax^2$, and thus

$$a = H / R^2$$

(2.3)

The slope at position x along the dish radius is calculated with

$$\zeta = \tan^{-1}\left(dy / dx\right) = \tan^{-1}\left(2ax\right).$$

(2.4)

2.4 Solar cavity receiver

A solar cavity receiver is used to capture the solar radiation coming from the dish concentrator (Fig. 2.1). Solar receivers can be divided into tubular, volumetric and particle receivers. A chronological review of the volumetric solar receivers of most interest for electricity production in the 10 MW – 200 MW range was published by Ávila-Marín (2011). A summary of the latest volumetric, particle and tubular receivers studied for central receiver

13

(tower) plants is available from Ho and Iverson (2014). These receivers are mostly for large-scale applications. In this work, a small-scale receiver for a small-scale open solar thermal Brayton cycle is studied (1-20 kW). Equation (2.5) shows how the overall efficiency of the open solar thermal Brayton cycle is calculated:

$$\eta_{STBC} = \eta_{col}\eta_{BC} = \eta_{refl}\eta_{REC}\eta_{BC}$$

(2.5)

where

$$\eta_{REC} = \eta_{rec}\eta_{optical}$$

(2.6)

Most Brayton cycles are not self-sustaining at operating temperatures below 480 °C (Stine and Harrigan, 1985). For the open and direct solar thermal Brayton cycle, the maximum receiver surface temperature and turbine inlet temperature are very important. According to Le Roux et al. (2012a), the higher these temperatures, the better the Brayton cycle will perform, but also the more heat will be lost to the environment. According to Garrett (2014) and Shah (2005), the maximum turbine inlet temperature of commercial turbochargers is more or less 950 °C. McDonald and Rodgers (2008) describe the concept of a ceramic micro-turbine with turbine inlet temperature of 1 170 °C. However, the higher the turbine inlet temperature, the less receiver material choices are available. Steinfeld and Schubnell (1993) presented a semi-empirical method to determine the optimum aperture size and operating temperature of a solar cavity receiver for maximum energy conversion efficiency. They found that for inaccurate concentrators, with Gaussian flux density distribution at the focal plane, the optimum operating temperature varied in the range of 527 °C to 1 027 °C.

According to Harris and Lenz (1985), for open-cavity receivers, overall collector efficiencies of between 60% and 70% are attainable with state-of-the-art systems operated in the temperature range of 500 °C – 900 °C with an optimum area ratio of $0.0004 \leq A' \leq 0.0009$. A number of high-temperature and high-efficiency receivers are available from the literature. These receivers are mostly not optimised to perform well in a small-scale open solar thermal Brayton cycle with recuperator. Typical receiver efficiencies and experimental data that have been obtained with pressurised volumetric receivers and tubular receivers are shown in Table 2.1. These receivers mostly operate at higher pressures than those which are studied in

14

this work. The receiver efficiency found in this work can be compared with the efficiencies of the state-of-the art receivers shown in Table 2.1. The receiver efficiency is defined as

$$\eta_{rec} = \dot{Q}_{net} / \dot{Q}* = \dot{m} c_{p0} (T_{out} - T_{in}) / \eta_{optical} \eta_{refl} \dot{Q}_{solar} \tag{2.7}$$

Table 2.1 Efficiencies of different solar receivers.

Receiver type	Reference number or model	η_{rec}	T_{out} (K)	T_{in} (K)	P (kPa)	$\dot{m}$ (kg/s)	Working fluid	ΔP (Pa)
Pressurised volumetric	PLVCR-5 (Ávila-Marín, 2011)	71%	1 323	-	420	-	Air	-
	PLVCR-500 (Ávila-Marín, 2011)	57%	1 233	300	415	-	Air	-
	DIAPR (Karni et al., 1997), (Ávila-Marín, 2011)	79%	1 477	308	1 800	0.0222	Air	25 000
	REFOS (Buck et al. 2002), (Ávila-Marín, 2011)	67%	1 073	-	1 500	-	Air	1 800
	Dickey, 2011	88%	871	542	273	0.409	Air	2 900
Tubular	Cameron et al., 1972	51%*	1 089	865	370	0.73	He-Xe	7 000
	Kribus et al., 1999	-	1 023	300	1 600 - 1 900	0.01	Air	40 000
	Heller et al., 2006	-	823	573	650	-	Air	10 000
	Neber and Lee, 2012	82%	1 500**	-	760	0.0093	Air	40
	Amsbeck et al., 2010	43%	1 076	876	384	0.526	Air	7 330
	Amsbeck et al., 2010	39.7%	1 055	871	375	0.516	Air	7 400
	Solugas (Quero et al., 2013)	-	873	598	850	5.6	Air	
	*calculated by author **proposed							

2.4.1 Solar receiver types

2.4.1.1 Particle receiver

A particle receiver is demonstrated by Hunt (1979). Bertocchi et al. (2004) describe the heating of air temperatures to far more than 1 000 °C, using a high-temperature solar particle receiver. Kim et al. (2009) and Miller and Koenigsdorff (1991) also describe the features and modelling of a particle receiver (Fig. 2.7). Kim et al. (2009) found many experimental results

15

including an increase in the opacity of the particle curtain with mass flow rate up to a constant value near the terminal velocity. Miller and Koenigsdorff (1991) found that the main loss from the receiver was reflection from the window, followed by emission and reflection from inside the receiver.
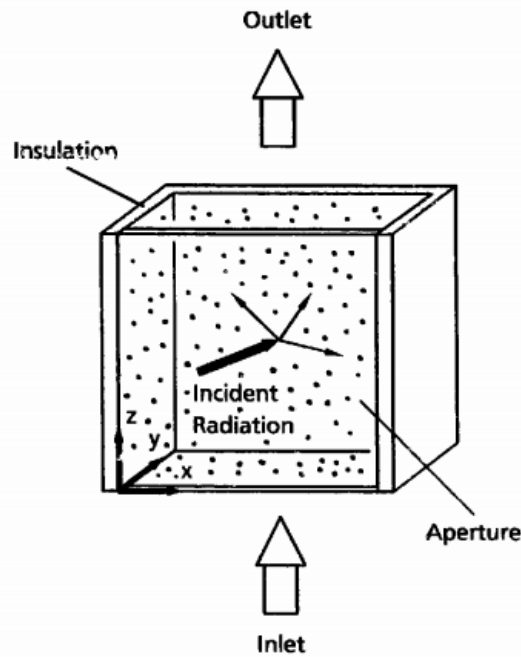
Figure 2.7 A particle receiver (Image extracted from Miller and Koenigsdorff, 1991).
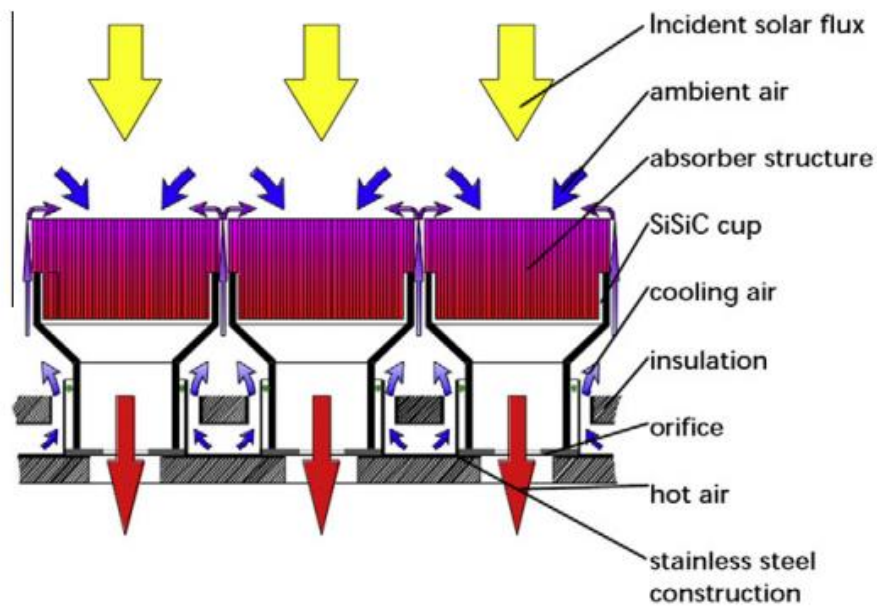
Figure 2.8 An open volumetric receiver – HiTRec (Image extracted from Ávila-Marín, 2011).

2.4.1.2 Open volumetric receiver

Open volumetric receivers are described by Ávila-Marín (2011) and Karni et al. (1998). An open volumetric receiver is shown in Fig. 2.8 (Ávila-Marín, 2011). Karni et al. (1998) present a "porcupine" volumetric solar receiver and its ability to withstand a solar flux of up to about 4 MW/m^2 while producing gas exit temperatures of up to 940 °C. This receiver consists of an array of pin-fins or elongated heat transfer elements, implanted in a base plate.

2.4.1.3 Closed volumetric receiver

For a volumetric solar receiver coupled to the Brayton cycle, a pressurised (closed) volumetric receiver is required and thus a window cover must be used for such a configuration. A closed volumetric receiver is shown in Fig. 2.9 (Buck et al., 2002). Heller et al. (2006) demonstrate that pressurised (closed) volumetric receivers are able to produce air of 1 000 °C. Pressurised volumetric receivers and its modelling are described in the literature (Hischier et al., 2009; Garcia et al., 2012; Kretzschmar and Gauché, 2012). Hischier et al. (2009) recommend that a minimisation of the cavity wall thickness in relation to its strength to withstand the operating pressures should be performed.
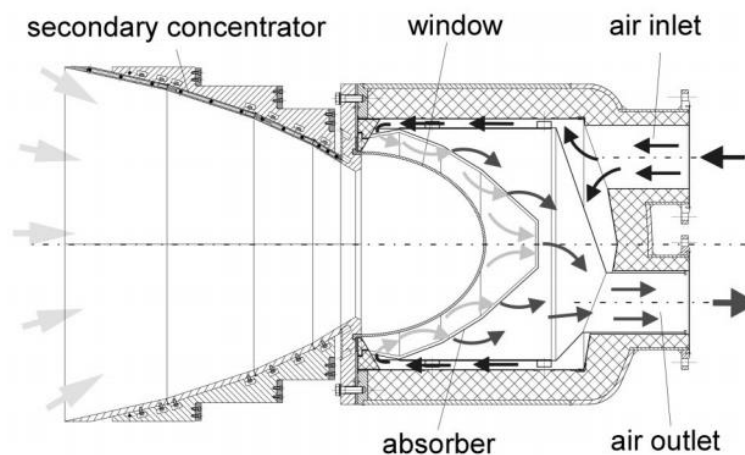
Figure 2.9 A closed volumetric receiver, REFOS (Image extracted from Buck et al., 2002).

According to Ávila-Marín (2011), many studies have demonstrated that the window poses a difficult design problem. The problems are related to optical properties, mechanical strength, sealing and cooling capabilities, variable working temperatures and stress-free installation. However, a novel pressurised volumetric air cavity receiver without a glass window is

17

presented by Hischier et al. (2009). The receiver has an outlet temperature of 1 000 °C at 10 bar, with predicted thermal efficiency of 78%.

2.4.1.4 Tubular receiver

In this work, the tubular cavity receiver is chosen for the small-scale open solar thermal Brayton cycle since its design is the least complex.

In a tubular receiver, one or more tubes are heated with solar radiation and the captured heat is transferred to a working fluid on the inside of the tube. An open-cavity tubular solar receiver as a heat source for an 11 kWe closed recuperative Brayton cycle using Cb-1Zr-alloy together with Li-F heat storage with 1 120 K as melting temperature was successfully tested in 1972 (Cameron et al., 1972). A mixture of helium and xenon was used as working fluid. Such a receiver with heat storage was also modelled by Cui et al. (2003). In this tubular receiver, the flow was divided into smaller tubes flowing across the length of the receiver cavity as shown in Fig. 2.10 (Amsbeck et al., 2008). The design of tubular air receivers can be challenging due to the combined effects of thermal oxidation, material creep, pressure-induced stress, daily thermal cycling and thermal shocks (Fork et al., 2012). A lifetime study was done by Fork et al. (2012) for a 4 MW solar receiver made of Inconel 617 operating at 900 kPa. According to Fork et al. (2012), a turbine inlet temperature of 1 120 K is a necessary upper limit for tube reliability.
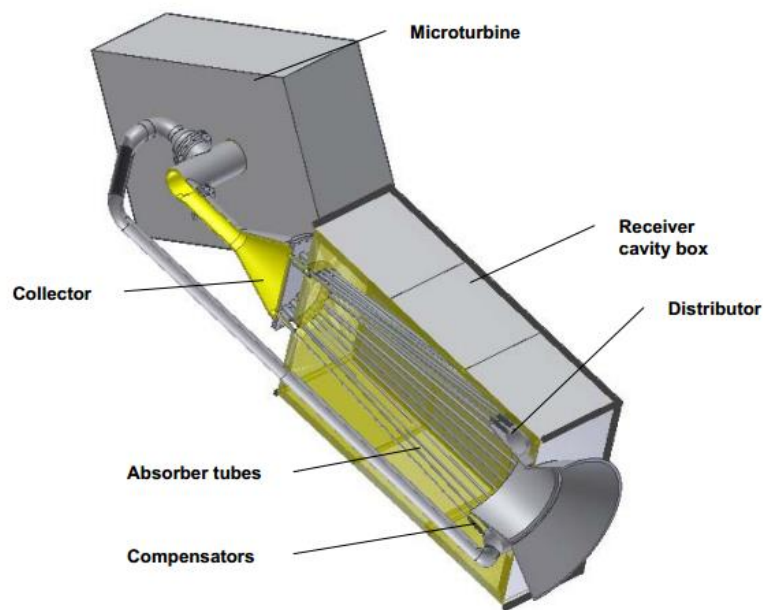
Figure 2.10 A longitudinal tubular receiver (Image extracted from Amsbeck et al., 2008).

18

According to Heller et al. (2006), the bent tube in a receiver coil is very flexible and thus reduces mechanical stresses due to thermal expansion of the tube material. Inconel 600 was used for a coiled tubular solar receiver by Kribus et al. (1999), supplying air of about 700 °C as a preheater for a secondary solar receiver (Fig. 2.11).
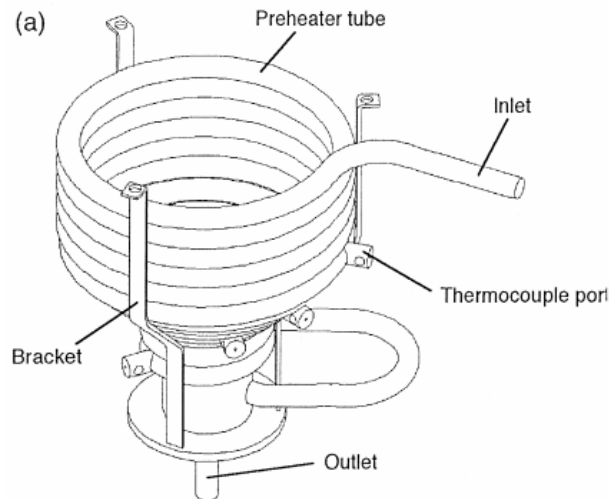
Figure 2.11 A coiled tubular receiver (Image extracted from Kribus et al., 1999).

It was found by Kribus et al. (1999) and Hischier et al. (2009) that, for a tubular receiver, as the flow rate increased, the receiver output power (and therefore efficiency) increased, while the air exit temperature decreased.

A surface coating and different materials are often used on high-temperature solar receivers to create low emissivity for low radiation heat loss. A small-scale Brayton tubular silicon-carbide receiver with an aperture diameter of 72 mm and a 17 m^2 dish area was proposed by Neber and Lee (2012). The receiver was designed to heat air up to 1 500 K.

From the literature, many different metal coatings are available (Lampert, 1979; Hutchins, 1979; Bogaerts and Lampert, 1983; Ambrosini et al., 2010). Most of these coatings cannot operate at the high temperatures studied in this work. The use of black chromium (with high absorptivity and low emissivity) is not recommended on components subject to temperatures in excess of 700 °C (Mandich and Snyder, 2010).

For steel containing high chromium, emissivity is usually lower because of the chromium oxide protection layer. The emissivity value becomes fairly constant after an initial three-hour heating during which the surface oxidation becomes fully developed, according to Wen

19

(2010). Thus, when a polished stainless steel tube is exposed to high temperatures, it will eventually become highly oxidised and have emissivity of 0.7 or lower (Bogaard et al., 1993; Richmond and Stewart, 1959). The emissivity of polished stainless steel is 0.17-0.3; for lightly oxidised stainless steel, it is 0.3-0.4 and for heavily oxidised stainless steel, the emissivity is 0.7-0.8, according to Çengel (2006). According to the NDI (2014), types 309, 310 or 446 stainless steels are most suitable for high operating temperatures. Types 310 and 314 are also recommended by Outukumpu (2013) as they offer good scaling resistance. According to Spisz et al. (1969), the absorptance of high-purity stainless steel sheet at lower temperatures is about 40%. The absorptance of stainless steel exposed to high temperatures and oxidised can be in the region of 0.85-0.9 and is independent of temperature while the emittance is in the region of only 0.1-0.2 at 100 °C, according to Valkonen and Karlsson (1982). The absorptance and emissivity of stainless steels depend very much on the surface finish and the operating temperature as well as the temperatures it has been exposed to previously. Absorptivity and emissivity of different stainless steels at different temperatures are available from the literature (Wen, 2010; Cao et al., 2013; Otsuka et al., 2005; Jones and Nisipeanu, 1996; Kobayashi et al., 1999).

2.4.2 Shape and design

The investigation and modelling of tubular cavity receivers are available from the literature (Shuai et al., 2008; Harris and Lenz, 1985; Steinfeld and Schubnell, 1993). The performance of different cavity receiver shapes and designs has been investigated by various authors (Shuai et al., 2008; Prakash et al., 2009; Sendhil Kumar and Reddy, 2008). According to Harris and Lenz (1985) and Shuai et al. (2008), for the same receiver cavity aperture and insulation thickness, cavity geometry has almost no effect on system efficiency. Shuai et al. (2008) investigated different classical cavity geometries and found that the shape of the cavity (geometry) had a significant effect on the overall distribution of the radiation flux in the cavity receiver. The primary effects of cavity geometry and concentrator rim angle are to vary the flux distribution on the inner-receiver walls. According to Shuai et al. (2008), manufacturing and assembly errors and unideal sunlight create a bigger solar spot in the focal region of a dish and a non-uniformity of heat flux distribution or local overheating in the cavity receiver. An upside-down pear-shaped cavity receiver would be the best to prevent local overheating in the cavity receiver, according to Shuai et al. (2008). Their study included the effects of slope error and sun shape but excluded the effects of solar tracking error and specularity error.

According to Harris and Lenz (1985), the use of a closed-cavity receiver with an aperture window may be questionable since radiation and convection heat losses can be in the neighbourhood of 12% of the energy entering the cavity, while a fused quartz or other high-temperature window will have an overall transmittance in the neighbourhood of 90%. In addition, there will still be radiation and conduction heat losses associated with the aperture window. The use of a window may thus only introduce an additional system cost. It should be noted that the optimum receiver aperture sizes found by Harris and Lenz (1985) were very small, since more accurate optics and tracking were considered. In an open Brayton cycle using air as working fluid and with less accurate optics, however, a larger receiver is required and therefore the radiation and convection heat losses can be much higher. The use of a window may be beneficial, especially as the receiver aperture size increases. The use of a glass window with a specific coating often works well at lower temperatures. However, at the high receiver temperatures required for the open solar thermal Brayton cycle, these coatings are often not available and the glass window will increase the complexity of the receiver. In this work, a glass window is thus not considered. A study of a receiver with a quartz glass cover was done by Cui et al. (2013). In their work, a maximum temperature of 1 073 K was investigated.

2.4.3 Heat loss models

The different methods of modelling heat losses from an open-cavity receiver are available (McDonald, 1995; Jilte et al., 2013; Xin and Le Quéré, 2006; Nogueira et al., 2011; Prakash, 2013; Clausing, 1981; Sendhil Kumar and Reddy, 2008; Vasseur and Robillard, 1982; Saitoh and Hirose, 1989; Harris and Lenz, 1985) in the form of conduction, convection and radiation heat loss.

Heat losses from a cavity receiver with frontal and side winds were investigated by Ma (1993) and Prakash et al. (2009). For a modified cavity receiver, numerical investigations regarding natural convection heat losses (Reddy and Sendhil Kumar, 2009) and radiation heat losses (Reddy and Sendhil Kumar, 2008) were presented for the modified cavity receiver. Le Roux et al. (2011, 2012a, 2012b) describe the modelling of a modified solar cavity receiver in detail.

The heat loss models presented in the above-mentioned literature are mostly not valid for high-temperature receivers as required in the open solar thermal Brayton cycle. According to McDonald (1995), the operating temperature range used by the Koenig and Marvin heat loss model for natural convection heat loss is considerably higher (valid up to 900 °C) than any

other heat loss model in their study. The convection heat loss rate from an open-cavity receiver of an open solar thermal Brayton cycle can therefore be determined according to the Koenig and Marvin heat loss model (Harris and Lenz, 1985), because it was designed to model heat loss from higher-temperature receivers.

The convection heat transfer coefficient for a cavity receiver will depend on its shape, the orientation of the aperture with respect to the wind direction, the wind speed as well as skirting or baffling placed around the aperture (Harris and Lenz, 1985). With no attempt to suppress forced convection, heat loss due to convection may be as much as three (Ma, 1993) to four (Harris and Lenz, 1985) times the magnitude of natural convection heat loss in a 4.5 m/s – 11 m/s wind depending on the receiver temperature. If a wind skirt is used, forced convection heat loss may be roughly twice the magnitude of the natural convection heat loss (Harris and Lenz, 1985). Natural convection heat loss is the highest when the receiver aperture face is in the vertical plane and negligible when the aperture is facing straight down. Overall, the effects of wind on convection heat loss are the greatest for wind blowing parallel to the aperture and the smallest for wind blowing directly into the aperture (Ma, 1993). When the aperture faces opposite to the wind direction, convection heat loss is not much higher than for natural convection heat loss (Harris and Lenz, 1985).

2.5 Recuperator

In the solar thermal Brayton cycle, a recuperator can be used to preheat air going to the solar receiver by extracting heat from the turbine exhaust air (Fig. 2.1). Different designs are available for the Brayton cycle recuperator. In solar applications, the recuperator is often designed as integral to the micro-turbine. Heat exchangers are required to be efficient, safe, economical, simple and convenient (Yilmaz et al., 2001). Heat transfer and pressure losses as well as the optimisation of cost, weight and size should be considered while designing the heat exchanger (Oğulata et al., 2000). According to Bejan (1982a), heat exchanger irreversibilities can be decreased by slowing down the fluid which is travelling through the heat exchanger. Also, for a fixed-area heat exchanger, the irreversibility can be reduced by allocating the area correctly (Bejan, 1982a).

Kreith and Kreider (1978) and Hesselgreaves (2000) suggest that counterflow heat exchangers should be used in solar thermal power systems and that parallel-flow heat exchangers should be avoided. According to Bejan (1982a), counterflow heat exchangers are often used in recuperative heating associated with the Brayton cycle. Shah (2005) also suggests that counterflow plate-type heat exchangers can be used as compact recuperators

22

with micro-turbines. Shah (2005) gives design criteria for micro-turbine recuperators. Criteria such as high performance with minimum cost, high exchanger effectiveness, compactness, 40 000-hour operation life without maintenance and low pressure loss ($< 5\%$) are given. According to Shah (2005), these criteria translate into a thin foil primary surface recuperator where flow passages are formed with stamping, folding and welding side edges by an automated operation. Such a recuperator is discussed by McDonald (2000; 2003).
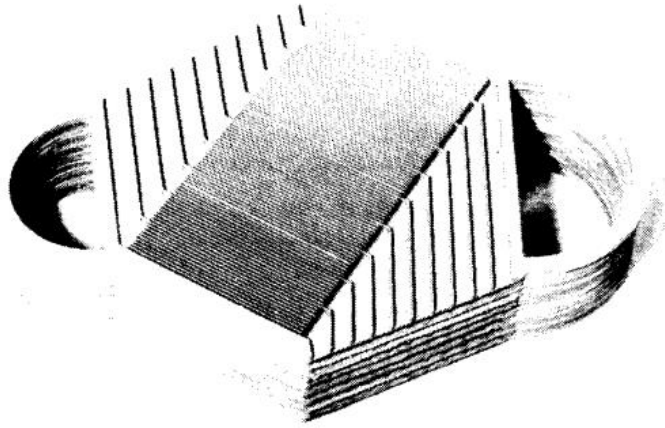
Figure 2.12 A ceramic counterflow plate-type recuperator (Image extracted from Pietsch and Brandes, 1989).

Pra et al. (2008) describe printed circuit technology and plate fin technology for recuperators while Tsai and Wang (2009) investigated the design and analysis of a Swiss-roll recuperator. Le Roux et al. (2011, 2012a, 2012b) describe the modelling of a plate-type recuperator. Traverso and Massardo (2005) discuss the furnace-brazed plate-fin type and the welded primary surface-type recuperators. Ultiainen and Sundén (2002) reviewed a recuperator with cross-corrugated or chevron pattern heat transfer surfaces. Different recuperator designs (Rogiers et al., 2006) and the effects of recuperator channel geometries (Burrow, 1969) are available from the literature. A high-temperature ceramic recuperator is described by Pietsch and Brandes (1989) and is shown in Fig. 2.12. A stainless steel counterflow plate-type recuperator is chosen for this study.

2.6 Optimisation and the second law of thermodynamics

The method of total entropy generation minimisation is discussed in this section. Firstly, the second law of thermodynamics and the basics of exergy analysis and entropy generation

minimisation are revisited. This is followed by the application of this method to the optimisation of the open solar thermal Brayton cycle.

2.6.1 Background

2.6.1.1 The second law of thermodynamics and exergy analysis

Equation (2.8) shows an exergy balance for a control volume according to Bejan et al. (1996) and Sonntag et al. (2003). The definition of specific exergy transfer at inlets and at outlets is given in Eq. (2.9) (Bejan et al., 1996). There is a fundamental difference between energy and exergy: exergy, unlike energy, uses the environment as its reference point. The exergetic approach is useful, since one would like to know what the optimal possibilities are for us as inhabitants of this environment instead of inhabitants of infinite space. Equation (2.10) (Sonntag et al., 2003) gives the expression for the balance of entropy for a control volume. For the entropy change of an ideal gas, Eq. (2.11) (Sonntag et al., 2003) can be used with constant specific heat.

$$\frac{dE_{cv}}{dt} = \sum_j \left(1 - \frac{T_0}{T_j}\right)\dot{Q}_j - \left(\dot{W}_{cv} - p_0\frac{d\upsilon_{cv}}{dt}\right) + \sum_i \dot{m}_i e_i - \sum_e \dot{m}_e e_e - \dot{E}_D \tag{2.8}$$

$$e = (h - h_0) - T_0(s - s_0) + \frac{1}{2}V^2 + gZ + e^{CH} \tag{2.9}$$

$$\frac{dS_{cv}}{dt} = \sum \dot{m}_i s_i - \sum \dot{m}_e s_e + \sum \frac{\dot{Q}_{cv}}{T} + \dot{S}_{gen} \tag{2.10}$$

$$s_2 - s_1 = c_{p0}\ln\frac{T_2}{T_1} - R\ln\frac{P_2}{P_1} \tag{2.11}$$

Exergy analysis is often applied to measure the performance of a system as was done by Karsli (2007) and Gomez et al. (2010). The total entropy generation rate for a system is found by summing the entropy generation rates from various entropy generation mechanisms in the system. Jubeh (2005) did an exergy analysis for an open regenerative Brayton cycle with isothermal heat addition and an isentropic compressor and turbine. Jubeh (2005) emphasises that first and second law analysis together are crucial for understanding and explaining the effect of any parameter on the performance of a thermal system.

24

2.6.1.2 The Gouy-Stodola theorem

The Gouy-Stodola theorem in Eq. (2.12) states that the lost available work, $\dot{E}_D$, in Eq. (2.8) is directly proportional to the entropy generation in a system (Bejan et al., 1996; Bejan, 1982a; Bejan, 1997). This theorem allows an analyst to describe a quantity to be maximised, such as the power output of a system, in terms of the total entropy generation rate in a system.

$$\dot{E}_D = T_0 \dot{S}_{gen} \qquad (2.12)$$

According to Holmberg et al. (2009), using the theory of Lampinen and Wikstén (2006),

$$\dot{E}_D = \dot{W}_{net,R} - \dot{W}_{net} = T_{eff} \dot{S}_{gen} \qquad (2.13)$$

where

$$T_{eff} = \frac{h_2 - h_{2R}}{s_2 - s_{2R}} \qquad (2.14)$$

Or, if the specific heat capacity and pressure remain constant,

$$T_{eff} = \frac{T_2 - T_{2R}}{\ln \dfrac{T_2}{T_{2R}}} \qquad (2.15)$$

where, for a system, h_2 is the specific enthalpy of the flow at the outlet and s_2 the specific entropy at the outlet and where h_{2R} and s_{2R} represent states of the enthalpy and entropy after a reversible process, respectively.

The choice of the control volume boundary is very important in the thermodynamic analysis of the solar thermal Brayton cycle and it defines whether Eq. (2.12) or Eq. (2.13) should be used in an analysis. For the analysis of a system, Eq. (2.12) can be used. Note that the heat losses from components should then be calculated as the heat loss up to the temperature, T_0. When calculating lost available work for a single component, Eqs. (2.14) and (2.15) can be used to calculate the boundary temperature. Le Roux et al. (2013) discuss this in more detail.

25

2.6.1.3 The sun as an exergy source

The solar input for the solar thermal Brayton cycle can be modelled in different ways. Throughout the literature (Reddy et al., 2012; Farahat et al., 2009; Moynihan, 1983; Torchia-Nunez et al., 2008), the absorbed solar radiation exergy rate, considering the Petela theorem (Petela, 1964), is given by

$$\dot{E} = \dot{Q}*\left(1 - \frac{4}{3}\left(\frac{T_a}{T_s}\right) + \frac{1}{3}\left(\frac{T_a}{T_s}\right)^4\right) \tag{2.16}$$

where T_s is the apparent blackbody temperature of the sun and $\dot{Q}*$ is the total solar power input crossing a control volume boundary.

According to Bejan (1982a), when doing an exergy analysis on a solar thermal system, the sun can be considered as an exergy-rich source and as a high-temperature fuel. Bejan (1996a) shows that the exergy rate of the sun is given as:

$$\dot{E} = \dot{Q}*\left(1 - \frac{T_0}{T*}\right) \tag{2.17}$$

where $T*$ is the apparent sun's temperature as an exergy source and $\dot{Q}*$ is the solar heat rate crossing a control volume boundary. This method was adopted for the exergy inflow of solar collectors by various authors (Kalogirou, 2004; Karsli, 2007; Hepbasli, 2008; Kalogirou, 2003; Hu et al., 2011). Equation (2.17) was also used to describe the exergy inflow for heliostat surfaces by Li et al. (2012) and Xu et al. (2011). The above-mentioned authors mostly adopted the value $T*$, as suggested by Petela (1964), being approximately equal to $0.75T_s$ (Bejan, 1982b; Bejan et al., 1981). T_s is the apparent blackbody temperature of the sun, which is about 6 000 K, or 5 762 K (Ozturk, 2010; Izquierdo Millan et al., 1996). Therefore, $T*$ is considered to be close to 4 500 K (Bejan, 1982b; Bejan, et al., 1981).

According to Onyegegbu and Morhenne (1993), the expression for the exergy flux which has the widest acceptability is the expression,

$$\dot{E} = \dot{Q}*\left(1 - \frac{4}{3}\left(\frac{T_a}{T_s}\right)\right) \qquad (2.18)$$

The selection of the control volume around the analysed system and the selection of $\dot{Q}*$, or the term in front of the bracket in Eqs. (2.16) – (2.18) is very important. $\dot{Q}*$ depends on which boundary is referred to in the analysis. For example, Eqs. (2.16) – (2.18) can be used to describe the incoming exergy from the sun or the incoming exergy from a reflector as shown in Fig. 2.13. $\dot{Q}*$ can thus be the beam irradiance, in the case where the incoming exergy is from a reflector, or $\dot{Q}*$ can be the global solar radiation with a boundary somewhere in the atmosphere or even in space.
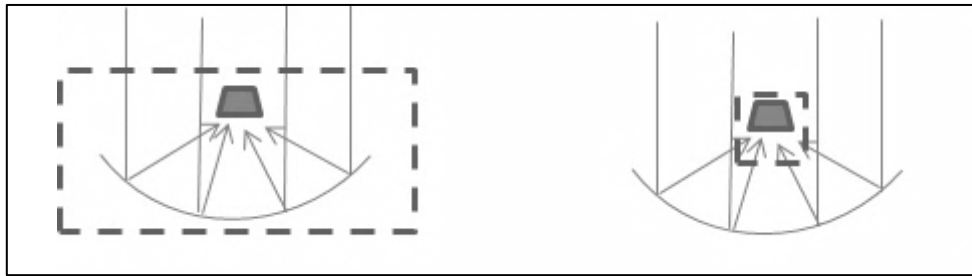
Figure 2.13 Control volume boundary including or excluding the solar reflector.

The available solar radiation per unit area from the sun varies according to days, months and environmental conditions. The best database for solar irradiance would be the long-term measured data at the site of the proposed solar system (Wong and Chow, 2001). A meteorological database can also be used such as given by Remund et al. (1999).

In this thesis, Eq. (2.17) is used in the analysis of the open solar thermal Brayton cycle with $T*$ as the apparent sun temperature and equal to 75% of the blackbody temperature of the sun. Also, I is the measured DNI and $\dot{Q}* = \eta_{refl}\eta_{optical}\frac{\pi D_{conc}^2}{4}I$. The dish reflector is thus not included in the control volume for thermodynamic analysis. Le Roux et al. (2013) discuss the sun as an exergy source in more detail.

2.6.1.4 Entropy generation minimisation

Thermodynamic optimisation or entropy generation minimisation (EGM) can be applied to an exergy analysis to optimise the performance of a system. Maximising the power output of

27

a power plant is equivalent to minimising the total entropy generation rate associated with the power plant (Bejan, 2002; Kalogirou, 2004; Keenan, 1951; Bejan, 1988; Bejan, 1996c). According to Bejan (1996b), EGM experienced astounding growth during the 1980s and 1990s in both the engineering and physics fields. The EGM method relies on the simultaneous application of heat transfer and engineering thermodynamics. It accounts for the inherent irreversibility due to heat, mass and fluid flow processes of devices and installations (Bejan, 1996b). EGM has been applied in various fields. The first power generation field to use EGM simulations frequently was that of solar power plants. It was found that an optimum coupling between a solar receiver and power cycle exists, so that the power output is a maximum (Bejan, 1996b).

According to Salamon et al. (2001), minimising the rate of entropy generation and maximising the power both push an operation towards minimum wastefulness, while minimum entropy generation and maximum power output are the opposite when considering frugality. Therefore, minimum entropy generation is considered as the objective of the conservationist and maximum power as the objective of the industrialist when, for example, managing an existing power plant or driving a motor vehicle (Salamon et al., 2001). In this thesis, however, the term entropy generation minimisation refers rather to the optimisation of geometries of a specific design in such a way that a system performs optimally. For example, the geometries of the power-producing parts of the engine of a motor vehicle can be designed in such a way that it produces maximum power output when a specific amount of fuel is available.

2.6.2 Optimisation of the solar thermal Brayton cycle

2.6.2.1 Results from the literature and influencing factors

The Brayton cycle and its optimisation have often been investigated in the literature. A variety of parametric studies have been conducted on different variations of the Brayton cycle and the solar thermal Brayton cycle. Some of these studies are noted in this section. A parametric study on the closed recuperative Brayton cycle was conducted (Kaushik and Tyagi, 2002). A closed recuperative Brayton cycle with intercooling (Tyagi et al., 2005) and with both intercooling and reheat (Tyagi et al., 2006) were also modelled and parametric studies were conducted. The efficiency and power output of these cycles were optimised. Chen et al. (1997) give the power output and the efficiency of a regenerative and closed Brayton cycle as functions of pressure ratios, reservoir temperatures, heat exchanger effectiveness, compressor and turbine efficiencies and working fluid thermal capacitance

rates. They found that the maximum power output of the system was strongly dependent on the effectiveness of the recuperator and that the maximum power output was attained when the effectiveness of the system's hot and cold side was arranged in a particular way. Wu et al. (1996) studied the performance of an endoreversible regenerative Brayton heat engine with focus on minimising irreversibilities at the hot- and cold-side heat exchangers of the system (for example, the solar receiver and the radiator) and the recuperator. They found maximum net power output of the system when the hot- and cold-side heat exchangers and the recuperator were ideal. However, these conditions require infinitely large components, making the system impractical.

Stevens et al. (2004) and Stevens and Baelmans (2008) state that a recuperator is often used to improve the overall cycle efficiency of a standard gas turbine and that a high heat exchanger effectiveness and low pressure drop are required to achieve maximum cycle efficiency. According to these authors, finding a compromise between these conflicting requirements is the main challenge in recuperator design. Stevens and Baelmans (2008) found that for maximum cycle efficiency, the cold- and hot-side pressure drops of a micro-recuperator used in a gas turbine cycle were uniquely connected, since their ratio depended primarily on the compressor pressure ratio. Stevens et al. (2004) also found that the recuperator effectiveness should be as high as possible and that the pressure drop should be preferably located at the cold side of the recuperator. Thus they concluded that the hot channels should be larger than the cold channels. They also concluded that for a fixed recuperator volume optimisation, the recuperator should be as short as possible with an as high as possible cross-sectional area.

Roco et al. (1997) present a general theoretical framework for a recuperative gas turbine cycle with external and internal irreversibilities in order to study the maximum power output, maximum efficiency, efficiency at maximum power, power at maximum efficiency and optimum pressure ratios. The optimal operating conditions were investigated in terms of the isentropic efficiencies of the compressor and turbine, pressure drops in the hot and cold streams and effectiveness of the heat exchangers. They found that the maximum efficiency and maximum power operating points were coincident at a recuperator efficiency of 50%.

Cheng and Chen (2000) used thermodynamic optimisation to optimise the power output of an endoreversible intercooled Brayton cycle coupled to two heat reservoirs with infinite thermal capacitance rates. The effects of intercooling on the maximum power of an endoreversible Brayton cycle were examined. They found that an endoreversible intercooled Brayton cycle was better than an endoreversible simple Brayton cycle without lowering the thermal

29

efficiency. A similar work was done by Wang et al. (2005). They found that there existed an optimal intercooling pressure ratio for maximum power.

Zhang et al. (2007) established a model in which the heat losses of the solar collector and the external and internal irreversibilities of a solar-driven Brayton heat engine were taken into account. This model was done for a solar thermal Brayton cycle without a recuperator. It was found that the performance characteristics of an irreversible solar thermal Brayton heat engine were different from those of a solar-driven heat engine consisting of an endoreversible Brayton heat engine. It was found that the larger the heat losses in the solar collector, the lower the optimum operating temperature of the solar collector and the smaller the maximum overall efficiency of the system.

2.6.2.2 Optimisation using EGM and geometry optimisation

The method of total entropy generation minimisation as applied to the solar thermal Brayton cycle is discussed in this section. However, in most of the above-mentioned analyses using EGM (or minimisation of irreversibilities), geometry optimisation was not done (except, for example, Stevens et al., 2004). The effects of component geometries were thus not included. The many factors influencing the performance of the system can be much better understood with the use of entropy generation minimisation and the optimisation of geometries for each unique case of the solar thermal Brayton cycle.

Geometric optimisations for the open solar thermal Brayton cycle with recuperator using thermodynamic optimisation were done by Le Roux et al. (2011, 2012a, 2012b). Le Roux et al. (2011) found that the optimised systems' irreversibilities were spread throughout the system in such a way that the internal irreversibility rate was almost three times the external irreversibility rate. The geometries of a modified cavity receiver and plate-type recuperator in an open and direct solar thermal Brayton cycle were optimised using EGM.

2.6.2.3 Effect of weather conditions

Various preliminary studies were done (Le Roux et al., 2012a; 2012c; 2012d) to model the effect of weather conditions on the performance of the open solar thermal Brayton cycle with fixed optimised components. In these results, the receiver was modelled as described in Le Roux et al. (2012a, 2012c, 2012d). Figure 2.14 shows that the net power output of a small-scale open and direct solar thermal Brayton cycle with concentrically wound tube cavity receiver and 4.8 m diameter dish depends on the maximum receiver surface temperature, net absorbed heat rate and micro-turbine operating point. Figure 2.14 shows lines of

constant net absorbed heat rate (depending on weather condition) and constant maximum receiver surface temperature (depending on compressor pressure ratio). Thus for any net absorbed heat rate available at the cavity receiver, the maximum net power output and optimum operating point can be determined from Fig. 2.14 for a specific allowable maximum receiver surface temperature. The maximum net power output is found at the intersection of the line of net absorbed heat rate with the line of allowable maximum receiver surface temperature. Figure 2.14 is specific to the micro-turbine used in the analysis.
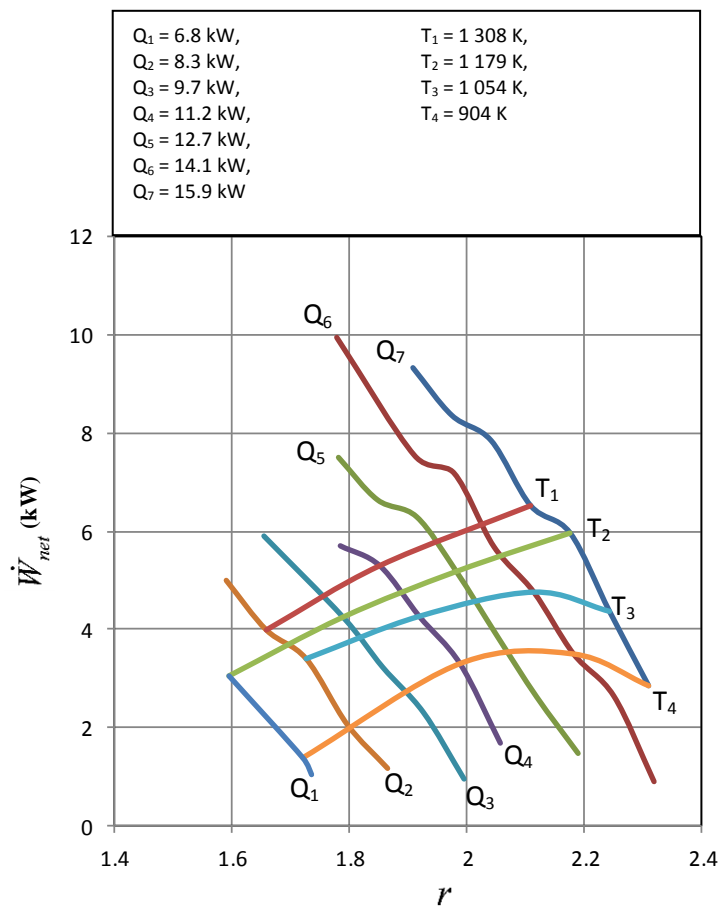
Figure 2.14 Performance map of a small-scale open solar thermal Brayton cycle with fixed optimised geometries in various weather conditions.

The performance map shows that the system can perform optimally at any weather condition and at any allowable maximum receiver surface temperature. When the net absorbed heat rate increases, the optimum system mass flow rate or compressor pressure ratio increases. For a system with fixed receiver and recuperator geometries, it was found that the weather would influence the net power output of the system.

31

2.7 Summary

The performance of the small-scale open solar thermal Brayton cycle with recuperator can be modelled and optimised. A literature study of the solar thermal Brayton cycle, its components and its optimisation was given in this chapter. The method of total entropy generation minimisation was found to be a holistic optimisation approach whereby the components of the cycle could be optimised. The factors contributing to the temperature profile and net heat transfer rate on the receiver wall can be divided into two components: geometry-dependent and temperature-dependent. It was found that the specular reflectance of any reflector was a function of time and that the errors due to the solar collector could be modelled with SolTrace, a ray-tracing algorithm. The Koenig and Marvin heat loss model was identified to model the convection heat loss rate from an open-cavity receiver. An open-cavity tubular stainless steel solar receiver and a counterflow plate-type stainless steel recuperator were identified as cost-effective and low-complexity solutions for the open solar thermal Brayton cycle. With the literature available, the modelling and optimisation of the small-scale open solar thermal Brayton cycle can be introduced.

CHAPTER 3
MODELLING AND OPTIMISATION

_____

3.1 Introduction

The modelling and optimisation of the components used in the small-scale dish-mounted open solar thermal Brayton cycle are discussed in this chapter. In SolTrace, the effects of optical errors and tracking errors on the solar receiver's performance are investigated so that an optimum ratio of receiver aperture area versus concentrator area can be found. To maximise the net power output of the cycle, an objective function, based on the method of total entropy generation minimisation, is presented in terms of the geometry variables of an open-cavity tubular solar receiver and counterflow plate-type recuperator. A method to determine the receiver tube surface temperatures and net heat transfer rates along the length of the receiver tube is presented. The modelling of the open solar thermal Brayton cycle in Flownex is also discussed.

3.2 Structuring the objective function for solar thermal Brayton cycle optimisation

When taking a control volume around an open and direct solar thermal Brayton system and assuming steady state, it can be determined where exergy is crossing the boundary. An exergy analysis was conducted for the system shown in Fig. 3.1 with reference to Fig. 2.1.
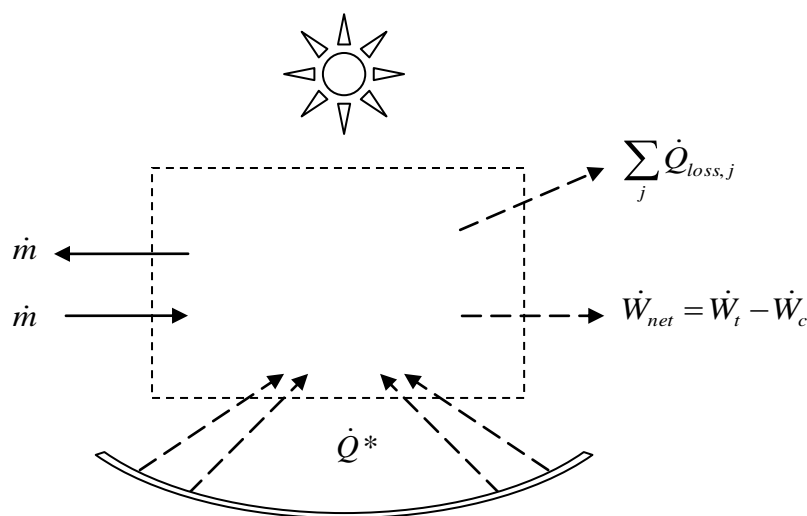
Figure 3.1 Control volume for the open solar thermal Brayton cycle.

The following equations arise, which can be used as objective function:

33

$$T_0 \dot{S}_{gen} = \dot{m}e_i - \dot{m}e_e + \left(1 - \frac{T_0}{T*}\right)\dot{Q}* - \left(1 - \frac{T_0}{T_{b,j}}\right)\dot{Q}_{loss,j} - \dot{W}_t + \dot{W}_c$$

$$\therefore T_0 \dot{S}_{gen} = \dot{m}\left[h_i - h_e - T_0(s_i - s_e) + \frac{1}{2}\left(V_i^2 - V_e^2\right) + g(Z_i - Z_e)\right] + \left(1 - \frac{T_0}{T*}\right)\dot{Q}* - \left(1 - \frac{T_0}{T_{b,j}}\right)\dot{Q}_{loss,j} - \dot{W}_{net}$$

(3.1)

or

$$\dot{W}_{net} = -T_0 \dot{S}_{gen} + \frac{\dot{m}}{2}\left(V_i^2 - V_e^2\right) + \left(1 - \frac{T_0}{T*}\right)\dot{Q}* - \left(1 - \frac{T_0}{T_{b,j}}\right)\dot{Q}_{loss,j} + \dot{m}c_{p0}(T_1 - T_{11}) - \dot{m}T_0 c_{p0}\ln\left(\frac{T_1}{T_{11}}\right)$$

(3.2)

Furthermore, the total internal entropy generation rate of the system can be written in terms of the sum of the entropy generation rate of each component and duct in the system. The entropy generation rate of each component is, in turn, a function of geometry variables. Thus, we have the total internal entropy generation rate as:

$$\dot{S}_{gen} = \sum \dot{S}_{gen,j} = \dot{S}_{gen(compressor)} + \dot{S}_{gen(duct23)} + \dot{S}_{gen(recuperator)}$$
$$+ \dot{S}_{gen(duct45)} + \dot{S}_{gen(receiver)} + \dot{S}_{gen(duct67)} + \dot{S}_{gen(turbine)} + \dot{S}_{gen(duct89)} + \dot{S}_{gen(other)}$$

(3.3)

Equation (3.3) can then be substituted into Eq. (3.2) to get the net power output for the open solar thermal Brayton cycle. The net power output is then written in terms of the total entropy generation rate of each of the components and ducts in the system. This equation can, in turn, be written in terms of all the geometry variables in the system. This equation for the net power output is the objective function, which should be maximised by optimising the geometry variables that describe the temperatures and pressures at each point in the system, subject to global constraints.

Note that for the analysis of the cycle, it is assumed that $T_8 = T_9$ and $T_2 = T_3$ with reference to Fig. 2.1 (the recuperator and micro-turbine are close to each other). It is also assumed that $P_2 = P_3$ and $P_8 = P_9$. Note that $T_1 = 300$ K and $P_1 = P_{10} = P_{11} = 86$ kPa (see Fig. 2.1). Also note that $T_{10} = T_{11}$ as it is assumed that the control volume boundary is very close to the hot stream exit of the recuperator. The temperatures and pressures in the system can be found with iteration using the isentropic efficiencies of the compressor and turbine as well as the

34

recuperator and receiver efficiencies. In this work, Matlab is used to determine the maximum net power output of the system as well as the optimum receiver and recuperator geometries. In the following sections, the modelling of these components, and thus the building blocks for structuring the objective function, is discussed. The many factors influencing the performance of an open solar thermal Brayton cycle can be understood much better with the use of the method of total entropy generation minimisation.

3.3 Solar collector

The factors contributing to the temperature profile and net heat transfer rate on the receiver wall can be divided into two components: geometry-dependent and temperature-dependent. The geometry-dependent factors include the concentrator dish with its optics: tracking error, specularity error, slope error, reflectance, spillage and shadowing. The optimum ratio of receiver aperture area versus concentrator area, A', can be determined with SolTrace. The radiation heat flux from the inner walls of the receiver onto the other walls is temperature-dependent and cannot be modelled with SolTrace. The temperature-dependent factors when modelling the solar receiver are discussed in Section 3.4.
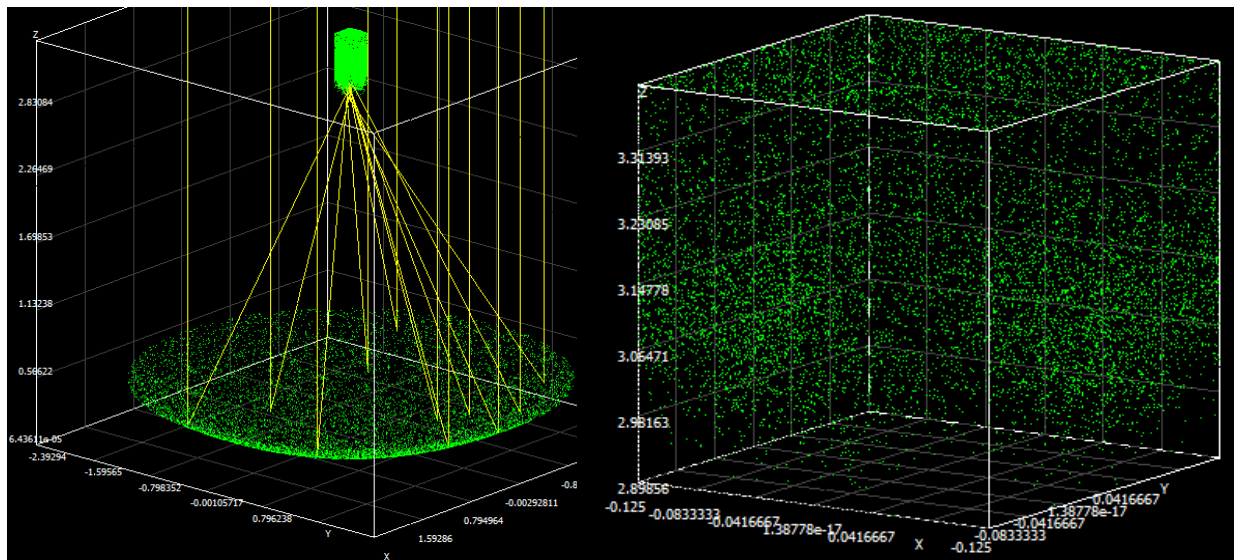
Figure 3.2 Example of an analysis done in SolTrace for the solar dish and receiver. A zoomed-in view of the solar receiver is shown on the right.

Figure 3.2 shows an example of the use of SolTrace to model the collector of a solar thermal Brayton cycle. A parabolic dish rim angle of 45° is investigated. In SolTrace, optical errors in the range of 0 to 50 mrad and tracking error in the range of 0° to 2° are investigated to

35

determine the effect on the performance of the open-cavity receiver. According to SolTrace, the optical error of the dish is determined from the slope error and specularity error as shown in Eq. (3.4).

$$\omega_{optical} = \left(4\omega_{slope}^2 + \omega_{specularity}^2\right)^{1/2}$$

(3.4)

A pillbox sunshape is assumed in the SolTrace analysis since a Gaussian sunshape is not recommended for highly accurate systems. The parameter for the pillbox, being a flat distribution, is simply the half-angle width, chosen as 4.65 mrad. SolTrace also includes the effect of the shade of the receiver on the concentrator. SolTrace is used to get the solar power available at different sizes of receiver apertures. It is also used to get the solar heat flux available at the inner walls of the receiver. The reflectance of sunlight from the cavity walls is accounted for in SolTrace so that the solar heat flux at the final intersection of the receiver can be determined.

3.4 Solar receiver

3.4.1 Solar receiver entropy generation

There are three main features that cause irreversibilities in the operation of any solar receiver: heat transfer from the sun to the receiver, heat loss from the receiver to the environment and the internal irreversibility in the receiver (Bejan, 1982a). The entropy generation rate of a solar receiver can be written as Eq. (3.5) (Kalogirou, 2004; Bejan, 1997; Rayegan and Tao, 2011), where the solar receiver receives solar radiation at the rate, $\dot{Q}*$.

$$\dot{S}_{gen} = \frac{\dot{Q}_0}{T_0} + \frac{\dot{Q}_r}{T_r} - \frac{\dot{Q}*}{T*}$$

(3.5)

$T*$ is the apparent sun temperature as an exergy source, T_0 is the ambient temperature, and T_r is the surface temperature of the absorber or receiver temperature. For a non-isothermal receiver and neglecting pressure loss (Torres-Reyes et al., 2001; Bejan, 1982a; Kalogirou, 2004):

$$\dot{S}_{gen} = \frac{\dot{Q}_0}{T_0} + \dot{m}c_p \ln\frac{T_{out}}{T_{in}} - \frac{\dot{Q}*}{T*}$$

(3.6)

36

The entropy generation rate in the open-cavity receiver of a solar thermal Brayton cycle for an ideal gas where the pressure loss is included is determined with Eq. (3.7):

$$\dot{S}_{gen} = -\frac{\dot{Q}*}{T*} + \frac{\dot{Q}_{loss,receiver}}{T_{s,ave}} + \dot{m}c_{p0}\ln\left(\frac{T_{out}}{T_{in}}\right) - \dot{m}R\ln\left(\frac{P_{out}}{P_{in}}\right) \qquad (3.7)$$

Note that in Eq. (3.7), $T_{s,ave} = T_b$, which is the temperature of the boundary across which the heat is being transferred. Equation (3.7) can be substituted in Eq. (3.2) and Eq. (3.3). Note the cancellation of the terms $(T_0/T_{s,ave})\dot{Q}_{loss,receiver}$ and $(T_0/T*)\dot{Q}*$ in the objective function when the entropy generation term is substituted into Eq. (3.2). From Eq. (3.7), it is shown that the net absorbed heat rate, heat loss rate, inlet and outlet temperatures and inlet and outlet pressures are required to calculate the entropy generation rate of a solar receiver. These values will depend on the time of day, month and year as well as the receiver type and receiver design.

The second law efficiency is defined as the efficiency of conversion of an exergy source. The second law efficiency in Eq. (3.8) gives a good indication of how the receiver will perform in the open solar thermal Brayton cycle. Note that the denominator is the rate of solar exergy source available at the receiver aperture and the numerator is the rate of exergy source minus the irreversibility rate. The irreversibility rate is available from the entropy generation rate in Eq. (3.7).

$$\eta_{2ndLaw} = \frac{\left(1 - \frac{T_0}{T*}\right)\dot{Q}* + \frac{T_0\dot{Q}*}{T*} - \frac{T_0\dot{Q}_{loss}}{T_{s,ave}} - T_0\dot{m}c_{p0}\ln\left(\frac{T_{out}}{T_{in}}\right) + T_0\dot{m}R\ln\left(\frac{P_{out}}{P_{in}}\right)}{\left(1 - \frac{T_0}{T*}\right)\dot{Q}*} \qquad (3.8)$$

3.4.2 Solar receiver modelling

A simple open-cavity tubular receiver is considered as receiver to be optimised in a small-scale open solar thermal Brayton cycle. Air travels through the inside of the tube and captures the net available heat. The receiver and its heat loss model are shown in Fig. 3.3 and Fig. 3.4 respectively.

37
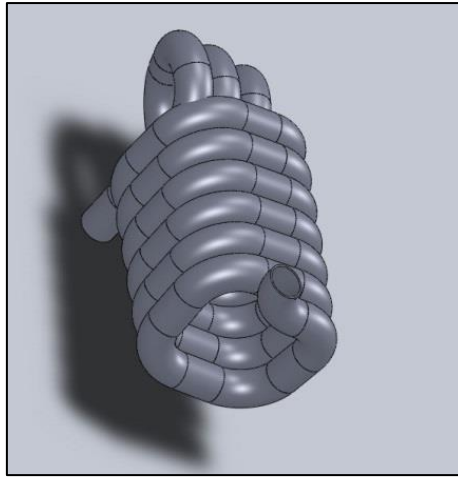
Figure 3.3 A rectangular open-cavity solar receiver.
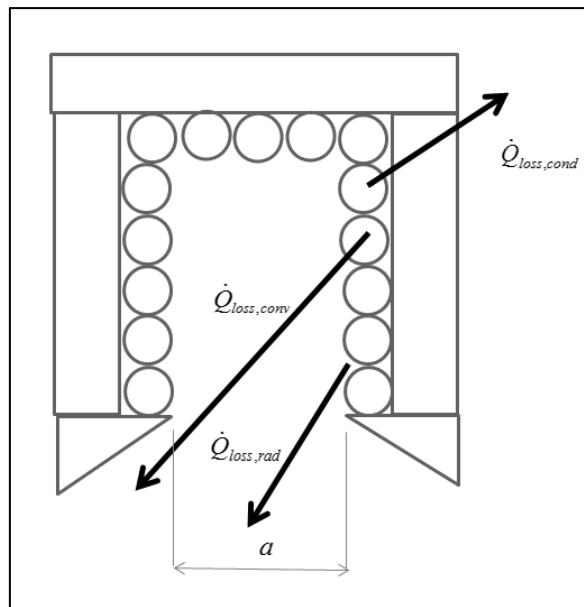
Figure 3.4 Heat loss from the open-cavity receiver.

A stainless steel tube with diameter, d, is coiled to form a solar cavity. This diameter can be optimised in the objective function in Eq. (3.2). Sunlight is absorbed on the inside of the cavity. The reflectance of the tube is assumed to be 15% (oxidised stainless steel). The receiver should be able to operate at a maximum surface temperature of 1 200 K. The receiver (Fig. 3.3) is covered with insulation. The heat loss from the receiver consists of convection, radiation and conduction heat loss. For ease of manufacturing, a rectangular cavity receiver is studied. For the rectangular cavity receiver studied, the depth of the receiver is equal to $2a$. The net heat transfer rate at the receiver tube is

$$\dot{Q}_{net} = \dot{Q}* - \dot{Q}_{loss,rad} - \dot{Q}_{loss,cond} - \dot{Q}_{loss,conv} \qquad (3.9)$$

3.4.2.1 Conduction heat loss from the solar receiver

For the receiver insulation, a high-temperature ceramic fibre is used. The conduction heat loss rate is calculated with Eq. (3.10) by assuming an average wind speed of 2.5 m/s for Pretoria. Note that an average surrounding temperature of 300 K and atmospheric pressure of 86.6 kPa is assumed.

$$\dot{Q}_{loss,cond} = A(T_{s,ave} - T_\infty)/R_{total} = (T_{s,ave} - T_\infty)/(1/h_{outer}A + t_{ins}/k_{ins}A) \qquad (3.10)$$

An insulation thickness of $t_{ins} = 0.1$ m is assumed for the receiver insulation. An average insulation conductivity of 0.061 W/mK at 550 °C is assumed, according to Harris and Lenz (1985). The convection heat transfer coefficient on the outside of the insulation is determined by assuming a combination of natural convection and forced convection due to wind. It is assumed that the receiver will be operating at an average angle of 45° for most of its lifetime in Pretoria and that the wind will mostly be either from the side or the back, since the dish will be shielding the receiver from wind. It is assumed that the effect of wind on the insulation is similar to forced convection on a flat plate for two sides of the receiver and for the receiver top, and similar to a rectangular shape in forced convection for the other two sides of the receiver. The Nusselt number for forced convection for the combined laminar and turbulent flow over the receiver insulation on the sides in parallel with the wind direction is (Çengel, 2006):

$$Nu = h_{side1}L/k = (0.037\,\mathrm{Re}_L^{0.8} - 871)\,\mathrm{Pr}^{1/3} \qquad (3.11)$$

The Nusselt number for forced convection on the other sides of the receiver is (Zukauskas, 1972):

$$Nu = h_{side2}L/k = 0.102\,\mathrm{Re}^{0.675}\,\mathrm{Pr}^{1/3} \qquad (3.12)$$

The Nusselt number for natural convection on the vertical sides of the receiver is (Churchill and Chu, 1975):

$$Nu = 0.59 Ra_L^{1/4} \tag{3.13}$$

It is assumed that the Nusselt number for natural convection on the upper tilted side of the receiver is the same as the Nusselt number on the lower tilted side (Çengel, 2006):

$$Nu = 0.59 Ra_L^{1/4} (\cos \theta)^{1/4} \tag{3.14}$$

where Θ is 45°.

For the combined natural and forced convection, the Nusselt number is (Çengel, 2006; Lloyd and Sparrows, 1970):

$$Nu_{combined} = \left(Nu_{forced}^{3.5} + Nu_{natural}^{3.5} \right)^{1/3.5} \tag{3.15}$$

From these equations, Eq. (3.16) was found for small-scale applications, in the range of receiver apertures of up to 2 m diameter, assuming an average heat transfer coefficient over the whole receiver (Le Roux et al., 2014b).

$$(1/h_{outer} + t_{ins}/k_{ins}) \approx 1.86 \tag{3.16}$$

The emissivity of the ceramic fibre insulation is assumed to be 0.9 at normal temperatures, according to Wallis (1989). For the purpose of this study, the heat loss from the receiver insulation outer surface due to radiation is neglected as the surface temperature of the insulation is assumed to be close to the environment temperature.

3.4.2.2 Radiation heat loss from the solar receiver

The total radiation heat loss rate from the receiver aperture is calculated with Eq. (3.17).

$$\dot{Q}_{loss,rad} = \varepsilon \sigma A_{ap} \left(T_{s,ave}^4 - T_\infty^4 \right) \tag{3.17}$$

When calculating the temperature profile along the length of the receiver tube, the radiation heat loss rate and heat gain rate at different sections of the inner wall are determined with the use of Eq. (3.18). The view factor is important when determining the temperature profile on the receiver tube.

$$\dot{Q}_n = A_n \sum_{j=1}^{N} F_{n-j} \left(\varepsilon_n \sigma T_{s,n}^4 - \varepsilon_j \sigma T_{s,j}^4 \right) \tag{3.18}$$

3.4.2.3 Convection heat loss from the solar receiver

The convection heat loss rate from the open-cavity receiver is determined according to the Koenig and Marvin heat loss model (Harris and Lenz, 1985), because it was designed to model heat loss from higher temperature receivers, as discussed in Chapter 2. The convection heat loss rate is determined as follows:

$$Nu_{cav} = hL/k = 0.52 B(\theta)(Gr_L \Pr)^{1/4} \tag{3.19}$$

where

$$B(\theta) = \cos^{3.2}\theta \text{ if } 0° \leq \theta \leq 45°, \quad B(\theta) = 0.707 \cos^{2.2}\theta \text{ if } 45° \leq \theta \leq 90° \tag{3.20}$$

and

$$Gr_L = L^3 g\beta(T_s - T_\infty)/v^2 \tag{3.21}$$

with

$$L = \sqrt{\frac{2a^2}{\pi}} \tag{3.22}$$

$$\beta = 1/T_{prop} \tag{3.23}$$

$$T_{prop} = 11/16 T_s + 3/16 T_\infty \tag{3.24}$$

The convection heat loss rate from the open-cavity receiver aperture is calculated with Eq. (3.25) where w is the wind factor, assumed 2 for 2.5 m/s wind when considering the literature study.

$$\dot{Q}_{loss,conv} = 9hwA_{ap}\left(T_{s,ave} - T_\infty\right)$$

(3.25)

Similarly, the convection heat loss rate from each tube section is calculated with Eq. (3.26).

$$\dot{Q}_{loss,conv,n} = h_n wA_n\left(T_{s,n} - T_\infty\right)$$

(3.26)

3.4.2.4 Solar receiver pressure drop

For a fixed receiver aperture area, the larger the receiver tube diameter, the shorter the tube length will be and the smaller the pressure drop. A larger receiver tube diameter will also result in a smaller pressure drop due to bends, because less bends or corners will be required to construct the receiver. The pressure drop through the tube is calculated as (White, 2005; Çengel, 2006):

$$\Delta P = \frac{\rho V_{ave}^2}{2}\left(f\frac{L}{d} + \sum_y K_y\right)$$

$$\Delta P = \frac{\rho\left(\frac{4\dot{m}}{\rho\pi d^2}\right)^2}{2}\left(f\frac{L}{d} + \sum_y K_y\right)$$

$$\Delta P = \frac{8\dot{m}^2}{\rho\pi^2 d^4}\left(f\frac{L}{d} + \sum_y K_y\right)$$

(3.27)

where f is determined from the Colebrook (1939) equation for rough stainless steel and the K-values are determined from White (2005) for standard 90° bends, available for the specific tube diameter being studied.

3.4.2.5 Method of determining receiver tube surface temperatures and net heat transfer rates

The temperature profile on the inner-cavity walls, which is the receiver tube surface, is determined by dividing the tube into a number of equally sized sections. The temperature

42

profile on the receiver walls depends on the size of the receiver and concentrator. The temperature profile and net heat transfer rate through the tube can be determined as follows:

$$\dot{Q}_{net,n} = \frac{\left(T_{s,n} - \sum_{i=1}^{n-1}\left(\frac{\dot{Q}_{net,i}}{\dot{m}c_{p0}} \right) - T_{in,0} \right)}{\left(\frac{1}{hA_n} + \frac{1}{2\dot{m}c_{p0}} \right)}$$

(3.28)

since the fluid temperature at the centre of a control volume under consideration is

$$T_{f,n} = T_{in,n} + \frac{T_{out,n} - T_{in,n}}{2} = T_{in,n} + \frac{\dot{Q}_{net,n}}{2\dot{m}c_{p0}}$$

(3.29)

and

$$\dot{Q}_{net,n} = hA_n\left(T_{s,n} - T_{f,n} \right)$$

(3.30)

where $T_{in,0}$ is the temperature of the air at the inlet of the receiver. $T_{in,n}$ is calculated from the heat gained at the previous tube sections. The following set of equations is also required to solve the surface temperatures and the rates of heat transfer into the tube at the different sections of the tube's length. Using Eqs. (3.28) and (3.31), an equal number of equations and variables are available to be solved.

$$\dot{Q}_{net,n} = \dot{Q}^*{}_n - A_n \varepsilon_n \sigma\left(m_1 T_{s,n} + c_1 \right) + A_n \sum_{j=1}^{N} F_{n-j}\varepsilon_j \sigma\left(m_1 T_{s,j} + c_1 \right)$$
$$- A_n \varepsilon_n \sigma F_{n-\infty} T_\infty^4 - A_n\left(m_2 T_{s,n} + c_2 \right) - \frac{A_n}{R_{cond}}\left(T_{s,n} - T_\infty \right)$$

(3.31)

since

$$\dot{Q}_{net,n} = \dot{Q}^*{}_n - \dot{Q}_{loss,rad,n} - \dot{Q}_{loss,conv,n} - \dot{Q}_{loss,cond,n}$$

(3.32)

43

and

$$\dot{Q}_{net,n} = \dot{Q}*_n - A_n \sum_{j=1}^{N} F_{n-j} \left(\varepsilon_n \sigma T_{s,n}^4 - \varepsilon_j \sigma T_{s,j}^4 \right) - A_n F_{n-\infty} \left(\varepsilon_n \sigma T_{s,n}^4 - \varepsilon_j \sigma T_\infty^4 \right)$$
$$- h_n w A_n \left(T_{s,n} - T_\infty \right) - A_n \left(T_{s,n} - T_\infty \right) / R_{cond}$$

(3.33)

Using Gaussian elimination and Matlab, the surface temperatures ($T_{s,n}$) and net heat transfer rates ($\dot{Q}_{net,n}$) can be obtained. For radiation heat loss to other tube sections, it is assumed that, in the range of temperatures between 1 000 K and 1 300 K, $T_{s,n}^4$ (see Eq. (3.33)), is a linear function of $T_{s,n}$ (see Fig. 3.5) in the form of $m_1 T_{s,n} + c_1$ (see Eq. (3.31)). For convection heat loss from surface temperatures between 900 K and 1 350 K, a linear function for the heat loss rate was also determined and used in the analysis. The largest error in making these assumptions was $R^2 = 0.988$. These heat loss functions had to be linearised so that simple Gaussian elimination could be used to determine the unknown surface temperatures and net heat transfer rates at each section of the receiver tube wall.
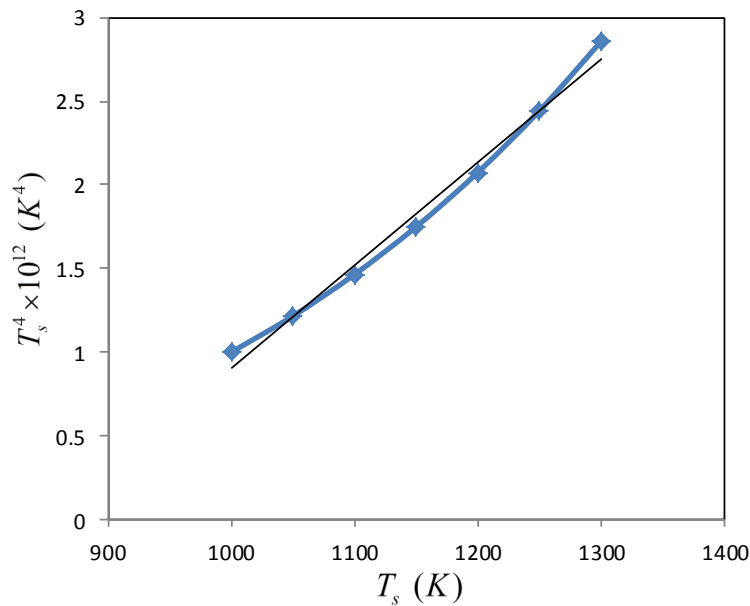
Figure 3.5 Regression line for T_s^4 with R^2-value of 0.988.

The conductivity of the stainless steel tube at the considered temperatures is assumed to be 30 W/mK (Outukumpu, 2013), and thus the thermal resistance due to conductivity through the tube wall of 2 mm thickness is neglected.

44

3.5 Recuperator

3.5.1 Recuperator entropy generation

To model the recuperator entropy generation, the inlet and outlet temperatures and pressures and the heat loss from the recuperator are required. The entropy generation rate in the recuperator is shown in Eq. (3.34) for an ideal gas (see Fig. 3.6). This equation or a similar version is also used in the literature by various authors (Bejan et al., 1996; Bejan, 1982a; Jubeh, 2005; Oğulata et al., 2000; Yilmaz et al., 2001; Hesselgreaves, 2000; Ordóñez and Bejan, 2000).

$$
\begin{aligned}
\dot{S}_{gen} &= \dot{m}c_{p0}\ln\left(T_2/T_1\right) + \dot{m}c_{p0}\ln\left(T_4/T_3\right) \\
&+ \dot{m}c_{p0}\ln\left[\left(P_2/P_1\right)^{(1-k)/k}\right] + \dot{m}c_{p0}\ln\left[\left(P_4/P_3\right)^{(1-k)/k}\right] + \frac{\dot{Q}_{loss,reg}}{T_b}
\end{aligned}
\tag{3.34}
$$

The fluid going from Position 1 to Position 2 is the cold stream and the fluid going from Position 3 to Position 4 is the hot stream in the heat exchanger as shown in Fig. 3.6.
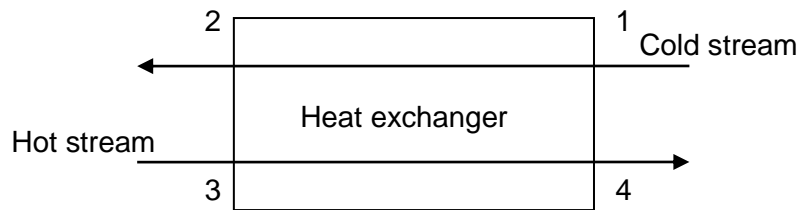
Figure 3.6 Heat exchanger with cold stream (1-2) and hot stream (3-4).

According to Ordóñez and Bejan (2000), entropy is also generated due to the discharge at the recuperator in an open cycle, hence Eq. (3.35). The equation to be used in an analysis depends on the definition of the boundaries of the control volumes of the recuperator and the system.

$$
\begin{aligned}
\dot{S}_{gen} &= \dot{m}c_{p0}\ln\left(T_2/T_1\right) + \dot{m}c_{p0}\ln\left(T_4/T_3\right) + \dot{m}c_{p0}\left[\frac{T_2-T_0}{T_0}\right] \\
&+ \dot{m}c_{p0}\ln\left[\left(P_2/P_1\right)^{(1-k)/k}\right] + \dot{m}c_{p0}\ln\left[\left(P_4/P_3\right)^{(1-k)/k}\right] + \frac{\dot{Q}_{loss,reg}}{T_b}
\end{aligned}
\tag{3.35}
$$

45

Equation (3.35) should not be used when the entropy generation due to the exhaust of the open system (warm air outlet) is already added as a separate entropy generation mechanism as in Eq. (3.2). Eq. (3.34) is thus used in conjunction with the objective function in Eq. (3.2).

3.5.2 Recuperator modelling
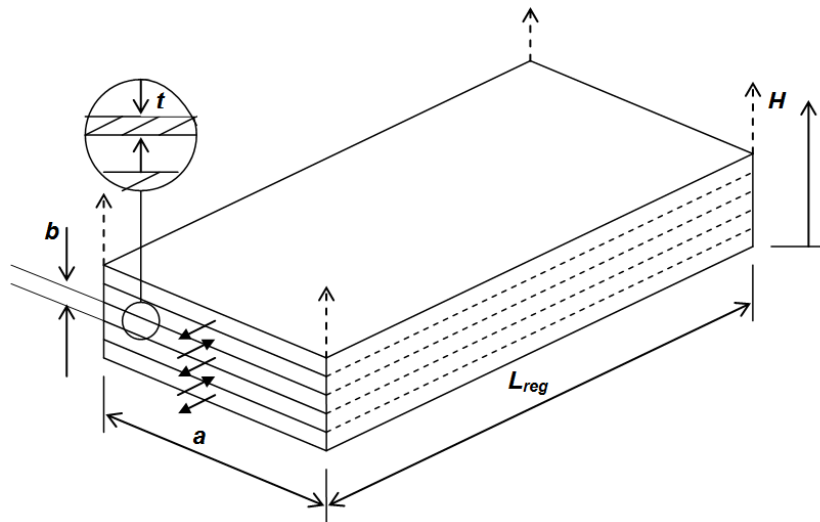
Figure 3.7 Recuperator geometry.
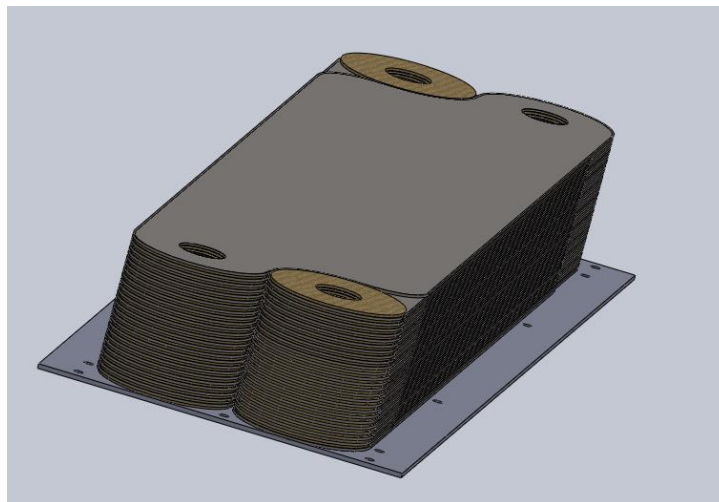
Figure 3.8 Recuperator design in SolidWorks.

A counterflow plate-type recuperator is used as shown in Fig. 3.7 and Fig. 3.8. The channels with length, L_{reg}, and aspect ratio, a/b, are shown. These channel dimensions and the number of channels can be optimised in the objective function in Eq. (3.2). The thickness of the material between the hot and cold stream, t, is 1 mm. The pressure drop through the

46

recuperator is calculated with the friction factor for fully developed laminar flow or with the Colebrook (1939) equation, depending on the Reynolds number. Hesselgreaves (2000), Oğulata et al. (2000) and Ordóñez and Bejan (2000) suggest that the ε-*NTU* (effectiveness – number of transfer units) method, based on the second law of thermodynamics, can be used to get the outlet temperatures and the total heat transfer rate from the hot fluid to the cold fluid. This is shown in the literature, for example, by Haugwitz (2002).

The heat loss to the environment from the surface of the recuperator can be a significant factor and it is recommended that it is included in the solar thermal Brayton cycle analysis. In this work, an updated version of the ε-*NTU* method is used (Nellis and Pfotenhauer, 2005), which includes heat loss from the recuperator because the recuperator is operating at a very high temperature and heat loss from the recuperator cannot be assumed negligible. The updated version of the ε-*NTU* method, according to Nellis and Pfotenhauer (2005), as applied in this work is shown below. The hot-side and cold-side efficiencies of the recuperator can be calculated with

$$\varepsilon_h = \begin{cases} 1-\Theta_{X=1}, Cr_h < 1 \\ Cr_h\left(1-\Theta_{X=1}\right), Cr_h > 1 \end{cases}$$

(3.36)

$$\varepsilon_c = \begin{cases} \dfrac{1-\Theta_{X=0}}{Cr_h}, Cr_h < 1 \\ 1-\Theta_{X=0}, Cr_h > 1 \end{cases}$$

(3.37)

where

$$\Theta_{X=0} = \frac{B+\left(\chi_h+Cr_h\chi_c\right)\left(1-e^E\right)}{\left(Cr_h-1\right)\left(e^E-\dfrac{1}{Cr_h}\right)}$$

(3.38)

$$\Theta_{X=1} = NTU_h\left(\chi_c+\chi_h\right)+\frac{\left(\Theta_{X=0}-1\right)}{Cr_h}+1$$

(3.39)

and

$$B = \left(NTU_h\left(\chi_c+\chi_h\right)+\frac{Cr_h-1}{Cr_h}\right)\left(Cr_h-1\right)$$

(3.40)

47

$$E = NTU_h\left(Cr_h - 1\right) \tag{3.41}$$

$$Cr_h = \frac{\dot{m}_h c_{p0,h}}{\dot{m}_c c_{p0,c}} \tag{3.42}$$

$$NTU_h = \frac{UA}{\dot{m}_h c_{p0,h}} \tag{3.43}$$

$$\chi_h = \frac{\dot{Q}_{loss,h}}{UA\left(T_{h,in} - T_{c,in}\right)} \tag{3.44}$$

$$\chi_c = \frac{\dot{Q}_{loss,c}}{UA\left(T_{h,in} - T_{c,in}\right)} \tag{3.45}$$

For the recuperator, the heat loss rate from the hot side and cold side of the recuperator is calculated with

$$\dot{Q}_{loss,h} = \frac{\dot{Q}_{loss,top,h}}{n} + \dot{Q}_{loss,side,h} \tag{3.46}$$

$$\dot{Q}_{loss,c} = \frac{\dot{Q}_{loss,bottom,c}}{n} + \dot{Q}_{loss,side,c} \tag{3.47}$$

where

$$\dot{Q}_{loss,top,h} = \frac{\left(T_9 + T_{10}\right)/2 - T_\infty}{R_{top,h}} \tag{3.48}$$

$$\dot{Q}_{loss,side,h} = \frac{\left(T_9 + T_{10}\right)/2 - T_\infty}{R_{side,h}} \tag{3.49}$$

48

$$\dot{Q}_{loss,bottom,c} = \frac{(T_3 + T_4)/2 - T_\infty}{R_{bottom,c}}$$

(3.50)

$$\dot{Q}_{loss,side,c} = \frac{(T_3 + T_4)/2 - T_\infty}{R_{side,c}}$$

(3.51)

and

$$R_{top,h} = \frac{1}{h_h aL} + \frac{t_{ins}}{k_{ins} aL} + \frac{1}{h_{out} aL}$$

(3.52)

$$R_{bottom,c} = \frac{1}{h_c aL} + \frac{t_{ins}}{k_{ins} aL} + \frac{1}{h_{out} aL}$$

(3.53)

$$R_{side,h} = \frac{1}{h_h bL} + \frac{t_{ins}}{k_{ins} bL} + \frac{1}{h_{out} bL}$$

(3.54)

$$R_{side,c} = \frac{1}{h_c bL} + \frac{t_{ins}}{k_{ins} bL} + \frac{1}{h_{out} bL}$$

(3.55)

In many counterflow heat exchangers, the heat flow through the material in the longitudinal direction is neglected in determining the temperature profile over the heat exchanger. Equation (3.56) (Bahnke and Howard, 1964, cited in Lerou et al., 2005) is a dimensionless parameter that shows whether longitudinal conduction can be neglected or not, where k is the thermal conductivity of the heat exchanger material and A the cross-sectional area. The longitudinal conduction cannot be neglected if $\lambda_{BH} > 10^{-2}$ (Lerou et al., 2005).

$$\lambda_{BH} = \frac{kA}{L\dot{m}c_{p,\min}}$$

(3.56)

3.6 Compressor and turbine

The geometry variables of the compressor and turbine are not considered for optimisation in this work. However, various off-the-shelf micro-turbines are considered as parameter in the objective function. Radial flow turbines are mostly used in small-scale power cycles and

49

therefore standard off-the-shelf micro-turbines from Honeywell (Garrett, 2014) are considered.

3.6.1 Compressor and turbine entropy generation

Equations (3.57) and (3.58) show the equations for the entropy generation rates for the compressor and turbine in the case of an ideal gas. These equations were also given by Jubeh (2005) and Bejan (1982a). The control volumes of the compressor and turbine are shown in Fig. 3.9 and Fig. 3.10 respectively. Equations (3.57) and (3.58) are formulated in terms of pressures and temperatures, which could be described by the isentropic efficiencies. The definitions of these efficiencies are commonly available, for example, from Weston (2000), Dixon (2005) and Haugwitz (2002). The calculation of the entropy generation rate for these components at different temperatures and pressures is important in the derivation of the objective function in Eq. (3.2). The pressures and temperatures can thus be written in terms of the geometry variables of the receiver and recuperator.

$$\dot{S}_{gen,c} = \dot{m}c_{p0i-e}\ln(T_e/T_i) - \dot{m}R\ln(P_e/P_i) + \frac{\dot{Q}_{loss,c}}{T_b} \tag{3.57}$$
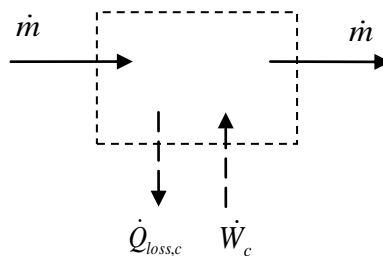
Figure 3.9 Control volume for the compressor.
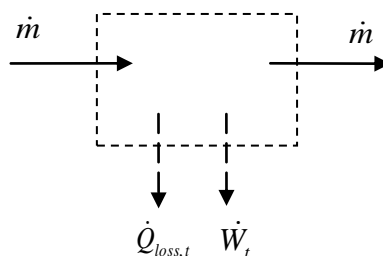
Figure 3.10 Control volume for the turbine.

50

$$\dot{S}_{gen,t} = \dot{m}c_{p0i-e}\ln(T_e/T_i) - \dot{m}R\ln(P_e/P_i) + \frac{\dot{Q}_{loss,t}}{T_b}$$

<div align="right">(3.58)</div>

3.6.2 Compressor and turbine modelling

When considering geometric optimisation of components in a system using a turbomachine, the compressor or turbine pressure ratio can be chosen as a parameter (Wilson and Korakianitis, 1998; Snyman, 2009; Lidsky et al., 1991). In this work, for a specific micro-turbine, the turbine operating point (turbine corrected mass flow rate and turbine pressure ratio) is chosen as parameter. The turbine corrected mass flow rate and turbine pressure ratio can be modelled with the use of the turbine map when considering experimental results for turbines and their mass flow rates (Zhuge et al., 2009). Note that the turbine corrected mass flow rate is a function of the turbine pressure ratio. The turbine operating point is thus used as parameter in the objective function so that the maximum of the objective function can be found at different parameter values.

3.6.2.1 Compressor modelling

The compressor isentropic efficiency, compressor corrected mass flow rate, compressor pressure ratio and rotational speed are intrinsically coupled to each other and are available from the compressor map (Garrett, 2014). The compressor should operate within its compressor map range, otherwise flow surge or choking can occur. These maps are mostly fitted with functions to make the modelling easier as shown by Haugwitz (2002) and Frei (2004), or fitted using software such as GTPower or TCMAP or as shown by Westin (2005). Methods to model the compressor, based on its geometry, are also available (Zhuge et al., 2009). Wahlström and Eriksson (2011) also present methods of compressor modelling. Le Roux et al. (2013) describe different compressor modelling techniques in detail.

In this work, however, the compressor isentropic efficiency and shaft speed are obtained with interpolation. The corrected compressor mass flow rate can be calculated with Eq. (3.59) since the mass flow rate through the compressor is equal to the mass flow rate through the turbine. Note that P_1 and T_1 are in psi and degrees Fahrenheit respectively (Garrett, 2014).

$$\dot{m}_{cCF} = \frac{\dot{m} \times \sqrt{(T_1 + 460)/545}}{P_1/13.95}$$

<div align="right">(3.59)</div>

<div align="center">51</div>

3.6.2.2 Turbine modelling

The turbine map shows the turbine corrected flow as a function of the turbine pressure ratio. The mass flow rate can be calculated using Eq. (3.60), where P_7 is in psi and T_7 in degrees Fahrenheit respectively (Garrett, 2014).

$$\dot{m}_t = \frac{\dot{m}_{tCF} \times P_7 / 14.7}{\sqrt{(T_7 + 460)/519}} \tag{3.60}$$

Turbine maps are not as available as compressor maps and even if they are available, the turbine efficiency is not always shown on the map; rather, a maximum efficiency is given. This often makes the modelling of the turbine efficiency difficult. According to Watson and Janota (1982) and experimental results by Westin (2005), Haugwitz (2002) and Zhuge et al. (2009), it can be assumed that the turbine efficiency is a function of the pressure ratio and the speed of the shaft and that a maximum efficiency exists for each speed line. The modelling techniques described by Westin (2005) and Reuter et al. (2010) are shown by Le Roux et al. (2013).

According to Westin (2005), Renberg (2008), Watson and Janota (1982) and Moraal and Kolmanovsky (1999), steady flow theory states that if the data in an original turbine map, showing a curve on axes of pressure ratio versus mass flow rate, is plotted as efficiency versus blade speed ratio (U/C_s or BSR), all data points would fall onto a parabolic curve, with a definite peak. This peak should be positioned at $U/C_s = 0.707$ if the ratio of expansion between turbine rotor and housing (reaction) is 50%, which seems to be common for vaneless radial turbines. This is also found in the doctoral thesis of Shaaban (2004), who suggests that the blade speed ratio is the most commonly used parameter to define the turbine efficiency. This phenomenon, when plotting efficiency versus BSR, is also found from turbocharger testing and research results (Newton et al., 2012). It is debatable how the turbine works under unsteady flow - Westin (2005) shows that the blade speed ratio at maximum efficiency can stray away from the standard value of 0.707, at non-steady conditions. According to Watson and Janota (1982), the problem can be treated as quasi-steady flow, meaning that the turbine performs under non-steady flow in the same way as it would if those sudden flow conditions were steady. Evidence on the error introduced by this assumption is not entirely consistent and it is commonly believed that the error will not exceed 5% (Watson and Janota, 1982). Capobianco and Marelli (2011) show the errors due to this assumption. The blade speed ratio

can be determined as (Westin, 2005; Wahlström and Eriksson, 2011; Batteh and Newman, 2008)

$$BSR = \frac{\dfrac{2\pi N}{60}\left(\dfrac{D_t}{2}\right)}{\left[2h_i\left(1 - r_t^{\frac{1-k}{k}}\right)\right]^{1/2}}$$

(3.61)

so that when it is assumed that the maximum efficiency is found at $BSR = 0.707$, r_t can be found for a specific speed (N). The points of maximum turbine efficiency for each speed line can be plotted on the given turbine map (mass flow rate versus pressure ratio). This maximum efficiency is also given on the turbine map. When considering experimental results by Westin (2005), Zhuge et al. (2009) and Haugwitz (2002), it is assumed that the turbine efficiency can be presented, with pressure ratio on the x-axis, by plotting curves for each speed line which goes through the point of maximum efficiency. The efficiency can be modelled as a parabolic function of the blade speed ratio (Frei, 2004; Zhuge et al., 2009; Wahlström and Eriksson, 2011; Jung et al., 2002):

$$\eta_t = \eta_{t,\max}\left(1 - \left(\frac{BSR - 0.6}{0.6}\right)^2\right)$$

(3.62)

According to Guzzella and Onder (2010), simplified closed-form descriptions of the turbine's efficiency can be approximated by

$$\eta_t(BSR) = \eta_{t,\max}\left(\frac{2BSR}{BSR_{opt}} - \left(\frac{BSR}{BSR_{opt}}\right)^2\right)$$

(3.63)

where, in automotive applications, typical values are $\eta_{t,max} \approx 0.65$ to 0.75 and $BSR_{opt} \approx 0.55$ to 0.65. Thus, Eqs. (3.62) and (3.63) are essentially the same.

From the above, it is concluded that from a basic turbine map, the turbine efficiency can be calculated as a function of pressure ratio and speed with the use of the blade speed ratio.

53

3.7 Other entropy generation mechanisms

Other entropy generation mechanisms occurring in the open solar thermal Brayton cycle, considered in this work, include entropy generation due to pipes and pipe bends. The entropy generation due to these mechanisms when assuming an ideal gas flow can be calculated with

$$\dot{S}_{gen} = \frac{\dot{Q}_{loss}}{T_b} + \dot{m}c_{p0}\ln\left(\frac{T_e}{T_i}\right) - \dot{m}R\ln\left(\frac{P_e}{P_i}\right)$$

(3.64)

The modelling of fluid flow in straight pipes, bent pipes and flow splits is discussed in the literature (Renberg, 2008; Haugwitz, 2002). Other typical flow restrictions can be modelled as shown by Frei (2004).

Often, the bearings of turbomachines are cooled using oil or water. The entropy generated from such a system can be described as shown in Eq. (3.65) and included in an objective function. The cooling flow loop can also be modelled separately or as the heat loss in Eqs. (3.57-3.58).

$$\dot{S}_{gen} = \frac{\dot{Q}_{loss}}{T_b}$$

(3.65)

When a solid or a liquid crosses the control volume boundary of the system, the entropy change can be modelled with Eq. (3.66) instead of Eq. (2.11).

$$s_e - s_i = c\ln\frac{T_e}{T_i}$$
(3.66)

3.8 Flownex modelling

Flownex is an integrated systems CFD code. Flownex is used for the design, simulation and optimisation of complete thermal fluid systems. Standard components are linked together to build flow systems. Flownex has an easy-to-use graphical user interface and results are presented in a graphical output. As validation, the complete integrated open solar thermal Brayton cycle with fixed components is modelled in Flownex at steady state. Figure 3.11 shows an example of how the system was modelled in Flownex for this study.
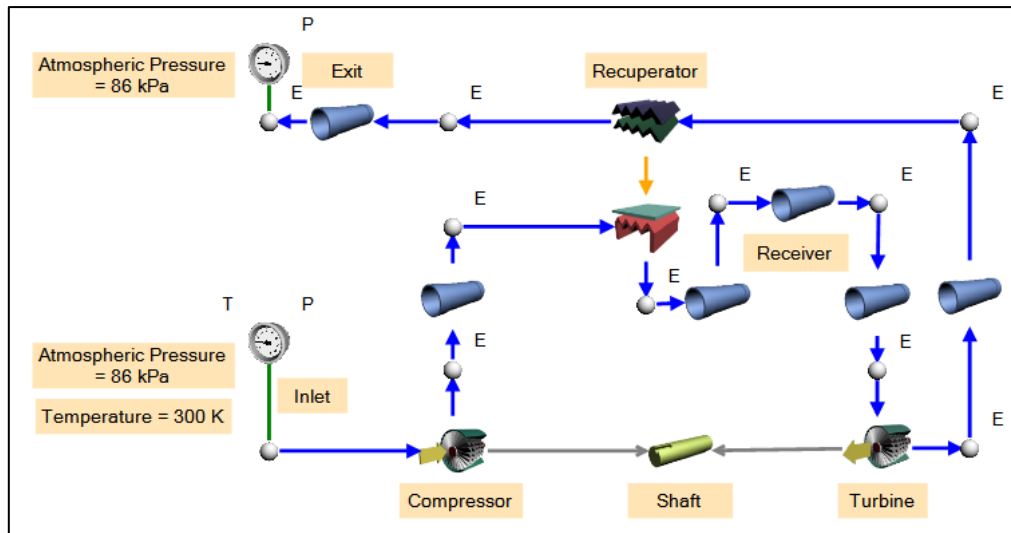
Figure 3.11 Flownex modelling of the small-scale open solar thermal Brayton cycle.

3.9 Summary

The modelling and optimisation of the components in a small-scale open solar thermal Brayton cycle were described in this chapter. The building blocks for an objective function for the net power output of the cycle were discussed. With the use of the presented models and iteration in Matlab, the net power output and temperatures and pressures can be determined for the cycle. The net power output of the cycle can be maximised by choosing different micro-turbines and their operating points and by optimising the geometries of the receiver and the recuperator. The factors contributing to the temperature profile and net heat transfer rate on the receiver wall were divided into geometry-dependent and temperature-dependent components. The heat available at the tubular solar cavity receiver was modelled with SolTrace and heat loss models from the literature were used to determine the heat loss. A method to determine the net heat transfer rate and surface temperatures on the receiver tube was presented. The efficiency of the counterflow plate-type recuperator was modelled with an updated *ε-NTU* method, which included heat loss to the environment. It was shown that the turbine efficiency of the micro-turbine can be modelled by determining the blade speed ratio of the turbine. The modelling and optimisation method described in this chapter is used in Chapter 4 to determine the optimum concentrator-to-receiver-area ratio, optimum receiver tube diameter and optimum recuperator geometries.

55

CHAPTER 4
ANALYTICAL RESULTS

_____

4.1 Introduction

The receiver surface temperature and net heat transfer rate for heating air will depend on the receiver size, mass flow rate through the receiver, receiver tube diameter, receiver inlet temperature and dish errors. The cost of the dish and tracking system of an open solar thermal Brayton cycle depends on the precision of the dish and tracking system. In this chapter, the maximum allowed dish-to-receiver-area ratio is found for the open solar thermal Brayton cycle with a tracking error of 1° and an optical error of 10 mrad. The optimum receiver tube size, recuperator geometry and micro-turbine to be used in a small-scale open solar thermal Brayton cycle for maximum net power output are determined. The analytical and numerical results of the performance of a dish-operated small-scale recuperated open solar thermal Brayton cycle are given and discussed. The results of the cycle's performance as calculated analytically and numerically are compared for validation.

4.2 Analytical results

4.2.1 Receiver performance

4.2.1.1 Preliminary results

Firstly, the effect of reflectivity and optical errors on the intercepted heat rate of an open-cavity receiver is investigated. Figures 4.1-4.3 show the optical efficiency of the receiver as a function of area ratio, A' (A_{ap}/A_{conc}), as determined with SolTrace. The optical efficiency is the solar power available at the aperture of a rectangular open-cavity receiver, relative to the solar power available after being concentrated at the dish, thus $\eta_{optical} = \dot{Q}*/\left(\eta_{refl}\dot{Q}_{solar}\right)$. Figures 4.1-4.3 show the optical efficiency when the tracking error is 0°, 1° and 2° respectively. The results show that, for small optical errors, the optimum area ratio increases as the tracking error increases. Note that the optical error should be multiplied with the reflectivity of the concentrator dish and $\dot{Q}_{solar}$ to determine the available solar power, $\dot{Q}*$, at the receiver aperture. These results are thus valid for all sizes of dish collectors.

By assuming an average receiver surface temperature of 1 150 K in the preliminary study, the heat losses from the receiver due to conduction, radiation and convection were determined with the heat loss models as described in Chapter 3. Figures 4.4-4.7 show the overall receiver

56

efficiency, which is the product of the optical efficiency and the receiver efficiency as shown in Eq. (2.6). Note that the overall receiver efficiency should be multiplied with the reflectance of the concentrator dish surface and $\dot{Q}_{solar}$ to determine the total net heat transfer rate in the receiver, $\dot{Q}_{net}$.
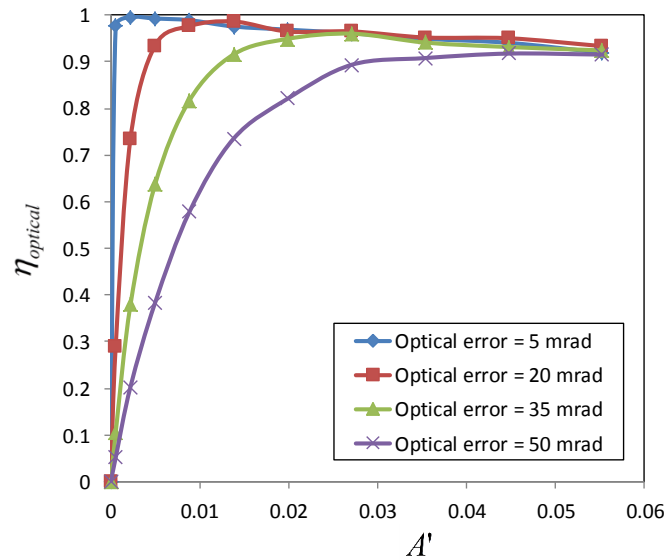
Figure 4.1 Optical efficiency of a solar dish and receiver with a tracking error of 0°.
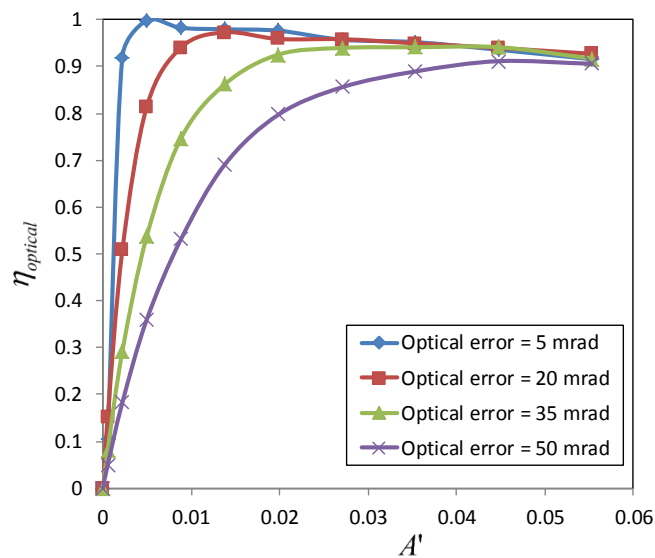
Figure 4.2 Optical efficiency of a solar dish and receiver with a tracking error of 1°.

Figure 4.6 shows the tremendous effect of surface emissivity. It shows that a much higher overall receiver efficiency could be expected if a high-temperature surface coating was available with emissivity of only 0.2 as compared with 0.7 in Fig. 4.5. It is recommended that

57

a cost-effective high-temperature receiver coating for low emissivity should be developed as such a coating would be very beneficial for the performance of the open solar thermal Brayton cycle.
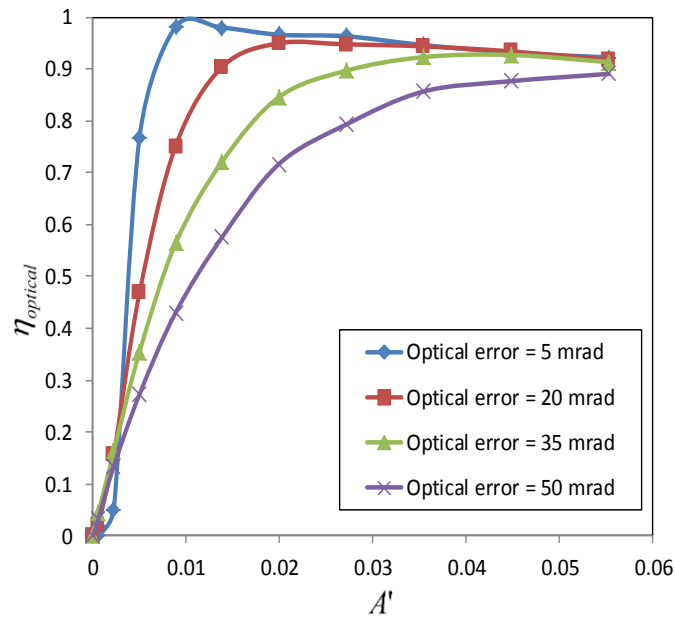
Figure 4.3 Optical efficiency of a solar dish and receiver with a tracking error of 2°.
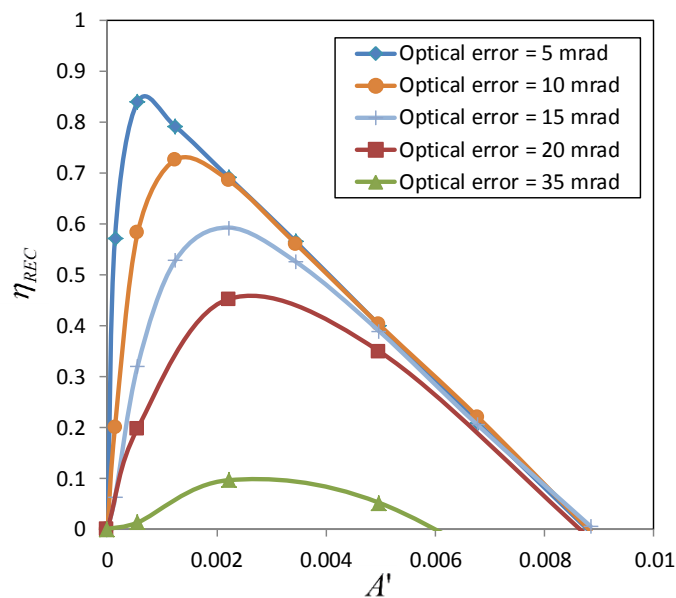
Figure 4.4 Overall receiver efficiency for a tracking error of 0° with receiver surface emissivity of 0.7.

58
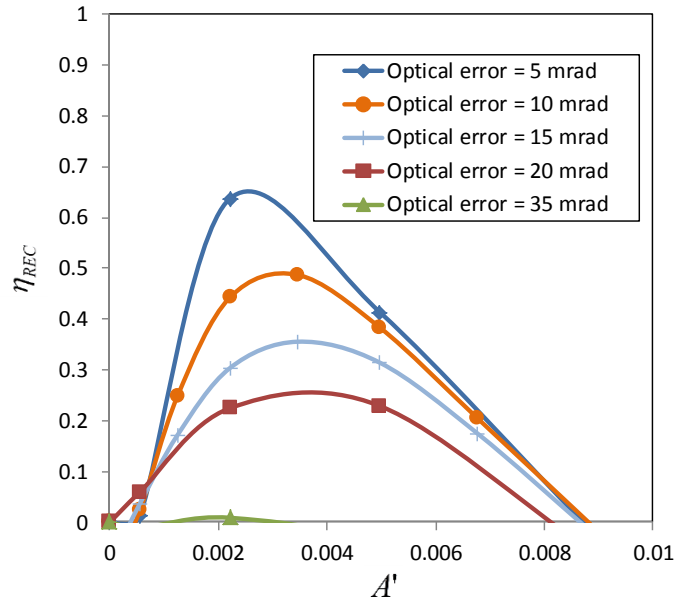
Figure 4.5 Overall receiver efficiency for a tracking error of 1° with receiver surface emissivity of 0.7.
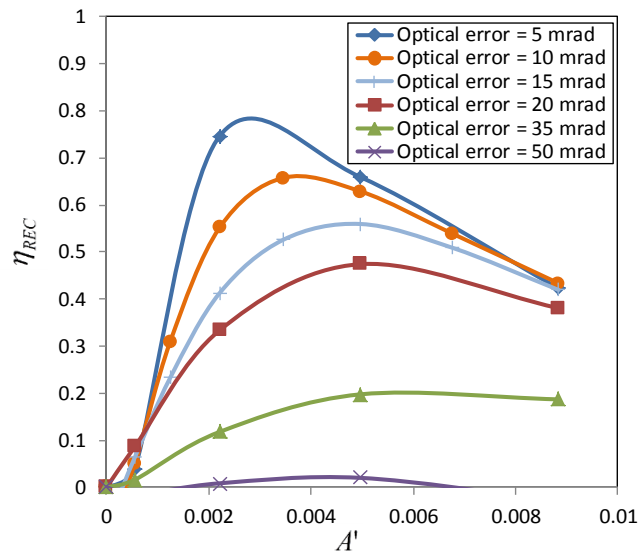
Figure 4.6 Overall receiver efficiency for a tracking error of 1° with receiver surface emissivity of 0.2.

When considering the literature, a specularity error and slope error of 4.5 mrad each are fairly large errors. These errors would translate to an optical error of 10 mrad, according to Eq. (3.4). This larger optical error would allow the dish and collector set-up to be less expensive. For an optical error of 10 mrad and a tracking error of 1°, an optimum ratio of $A' \approx 0.0035$ is identified from Fig. 4.5, where the accompanying optical efficiency is 92.3% (see Fig. 4.1). Note that A' is the optimum ratio of receiver aperture area to concentrator

59

aperture area. A receiver used in a collector with this optimum area ratio will be used for further analysis in the following sections. Also note that this is an optimum area ratio for a system with concentrator rim angle of 45°, tracking error of 1°, optical error of 10 mrad, average receiver surface temperature of 1 150 K, receiver surface emissivity of 0.7, 0.1 m ceramic fibre insulation thickness and an assumed average wind speed of 2.5 m/s. This optimum area ratio is, however, also valid for a surface emissivity of 0.2 (see Fig. 4.6) and for optical errors in the range of 5 mrad to 20 mrad.

The optimum ratio can be compared with the optimum ratios of $A' \approx 0.0007$ (Steinfeld and Schubnell, 1993), $0.0004 \leq A' \leq 0.0009$ (Harris and Lenz, 1985) and $A' \approx 0.00024$ (Neber and Lee, 2012) found in the literature. The optimum ratios found by Harris and Lenz (1985) and Steinfeld and Schubnell (1993) were much smaller than those found in this work because of more accurate optics assumed in their studies – tracking error was not included in their studies, thus the tracking error was 0°. The results found by Harris and Lenz (1985) do, however, compare well with the optimum area ratio found in Fig. 4.4 for a tracking error of 0° and an optical error of 5 mrad. Neber and Lee (2012) also found a much smaller optimum ratio, since their silicon carbide receiver operated at a much higher temperature, which would intensify heat loss significantly.
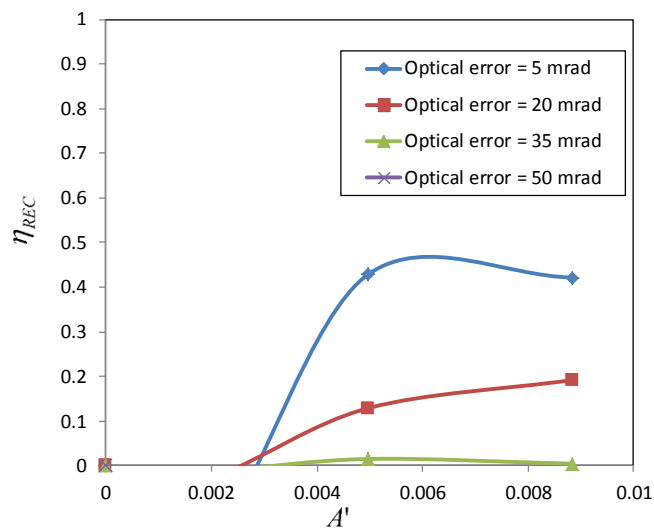
Figure 4.7 Overall receiver efficiency for a tracking error of 2° with receiver surface emissivity of 0.2.

Figure 4.7 shows the effect of a tracking error of 2° with a surface emissivity of 0.2. For a surface emissivity of 0.7 and 2° tracking error, the overall receiver efficiency is very low

60

(less than 20%) and is not shown. A tracking error of more than 1° is thus not favourable, even with very low receiver surface emissivity.
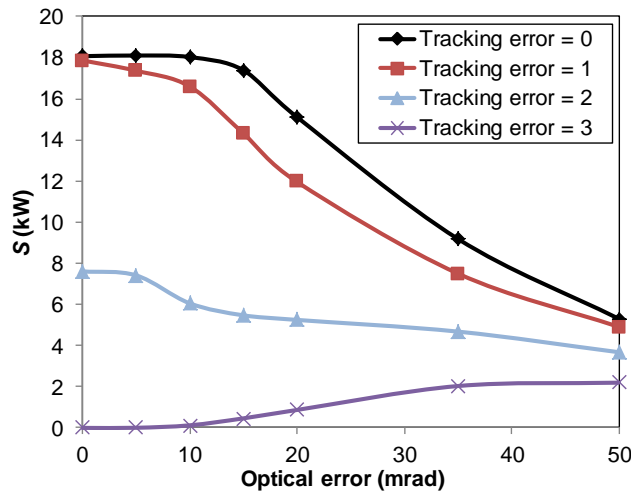
Figure 4.8 Available solar power at the aperture of the open-cavity receiver.
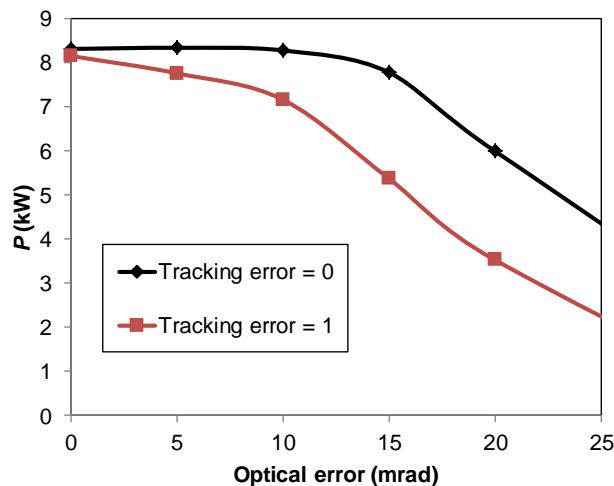
Figure 4.9 The net heat transfer rate at the open-cavity receiver inner walls.

For the fixed area ratio of $A' = 0.0035$, the available solar power at the aperture of a receiver with $a = 0.25$ m (see Fig. 3.4) is shown in Fig. 4.8 for different tracking errors and optical errors. A dish with diameter of 4.8 m is used and an average receiver surface temperature of 1 150 K is assumed. Figure 4.8 shows that the available solar power decreases as the optical error and tracking error increase. However, at a tracking error of 3°, the available solar power increases as the optical error increases. Figure 4.9 shows the net heat transfer rate at the cavity receiver inner wall. The net heat transfer rate is the available solar power minus the heat loss rate from the cavity receiver to the environment. Figure 4.9 shows that an optical

61

error of 10 mrad or less with a tracking error of 1° or less is required to have an acceptable net heat transfer rate. A tracking error of 2° would thus not be acceptable for the collector of a small-scale open solar thermal Brayton cycle with $A' = 0.0035$.

4.2.1.2 Receiver solar heat flux profile

In the previous section, results showed that an optimum area ratio of $A' = 0.0035$ could be used for a system with tracking error of 1° and 10 mrad optical error. For this optimum area ratio, tracking error and optical error, the solar heat flux rate at the different parts of the different walls of the receiver is shown in Fig. 4.10 and Fig. 4.11, as was found with SolTrace.
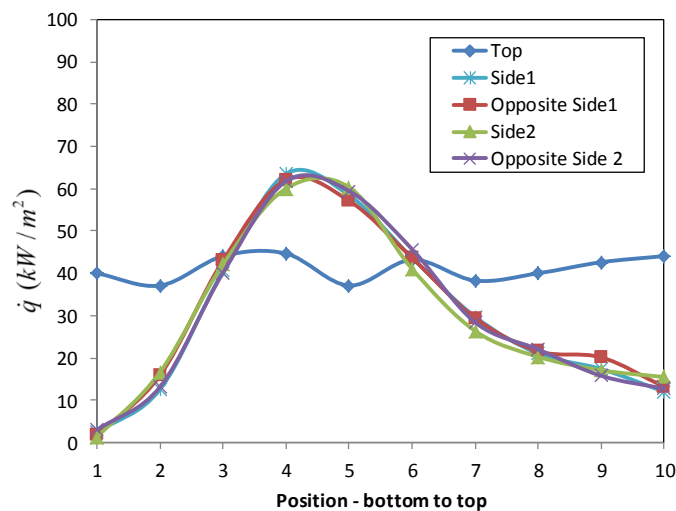
Figure 4.10 Heat flux rate at different positions on the different receiver inner walls for a tracking error of 0°.

These results were obtained by assuming that the inner walls of the cavity receiver were flat surfaces. Note that these solar heat flux rates are for a parabolic concentrator rim angle of 45°. Also note that the results should be multiplied with the reflectance of the concentrator dish to determine the available solar heat flux rate at the receiver inner walls. A solar beam irradiance of $I = 1\,000$ W/m^2 was used to generate the results. Note that $\dot{Q}_{solar} = I\pi D_{conc}^2 / 4$. The results are also valid for other solar beam irradiances if multiplied with the beam irradiance ratio. These solar heat flux rates are valid for all sizes of rectangular open-cavity receivers with the ratio of $A' \approx 0.0035$. The results show that the higher the tracking error, the larger the heat flux rate at the bottom parts of the one side of the receiver.

62
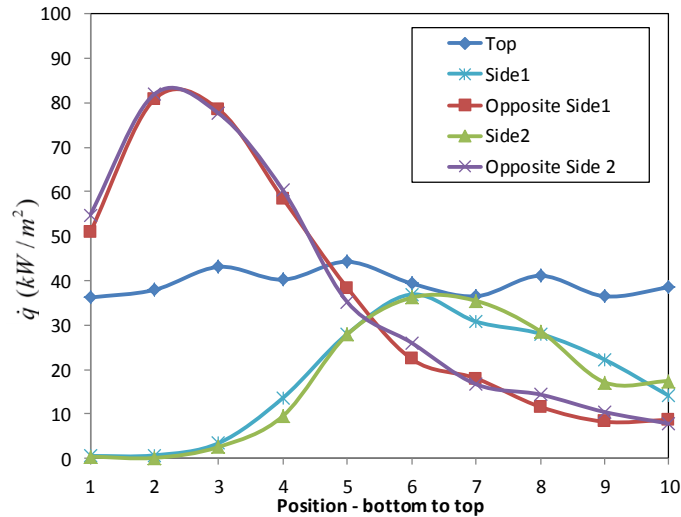
Figure 4.11 Heat flux rate at different positions on the different receiver inner walls for a tracking error of 1°.

4.2.1.3 Temperature profile and net heat transfer rate of receiver tube

The receiver surface temperature at the different positions of the tube and the net heat transfer rate available for air heating will depend on the receiver size, mass flow rate through the receiver, receiver tube diameter, receiver inlet temperature and dish reflectivity. Thus a receiver with aperture of 0.25 m x 0.25 m and a dish concentrator diameter of 4.8 m ($A' = 0.0035$) with 85% reflectivity and DNI of 1 000 W/m^2 was chosen for further analysis. The depth of the receiver was 0.5 m, as the receiver was rectangular. The results were found in Matlab by solving Eqs. (3.28) and (3.31) simultaneously using Gaussian elimination. Three tube diameters of 0.05 m, 0.0625 m and 0.0833 m were considered. These are the diameters on the inside of the tube. The view factors for the different tube sections are shown in Tables 4.1, 4.2 and 4.3, as determined with view factor relations available from Çengel (2006).

Note that, for the analysis, the receiver tube of the rectangular cavity is divided into a number of sections as determined with Eq. (4.1):

$$N = 4(2a/d) + a/d = 9a/d \tag{4.1}$$

The results shown in Fig. 4.12 and Fig. 4.13 give the tube surface temperature and net heat transfer rate at the different positions of a 0.05 m diameter tube used in an open-cavity rectangular receiver with square aperture side length of $a = 0.25$ m and an inlet temperature of 1 070 K.

63

Table 4.1 View factors for tube sections in the different parts of the receiver (for $d = 0.05$ m).

Tube position (View factor from)	View factor to	Number of transfers	View factor
Top wall	Aperture	1	0.07
	Other	40	0.0233
Side wall	Top	5	0.0233
	Across	1	0.05
	Left	1	0.085
	Right	1	0.085
	Aperture	1	0.116
	Other	27	0.0211

Table 4.2 View factors for tube sections in the different parts of the receiver (for $d = 0.0625$ m).

Tube position (View factor from)	View factor to	Number of transfers	View factor
Top wall	Aperture	1	0.07
	Other	32	0.0291
Side wall	Top	4	0.0291
	Across	1	0.0625
	Left	1	0.1
	Right	1	0.1
	Aperture	1	0.116
	Other	21	0.0241

Table 4.3 View factors for tube sections in the different parts of the receiver (for $d = 0.0833$ m).

Tube position (View factor from)	View factor to	Number of transfers	View factor
Top wall	Aperture	1	0.07
	Other	24	0.0388
Side wall	Top	3	0.0388
	Across	1	0.0833
	Left	1	0.115
	Right	1	0.115
	Aperture	1	0.116
	Other	15	0.0303

The increase in air temperature is shown in Fig. 4.12 and Fig. 4.13. A mass flow rate of 0.07 kg/s is used. With the use of the air temperature increase and the mass flow rate, the overall collector efficiency, η_{col} from Eq. (2.5), for 0° tracking error (Fig. 4.12) is calculated as 44% whereas, for a tracking error of 1° (Fig. 4.13), the overall collector efficiency is calculated as 39%. This efficiency can be improved by improving the reflectance of the concentrator, by changing the receiver design or surface coating or by altering the mass flow rate, inlet temperature and tube diameter.
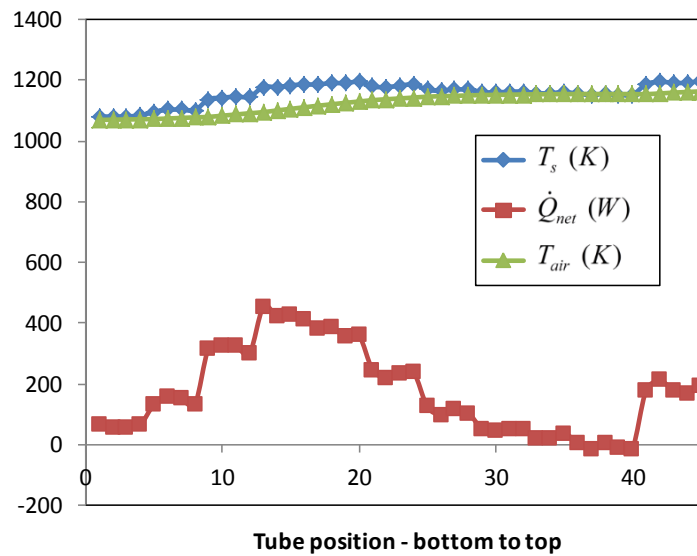
Figure 4.12 Temperatures and net heat transfer rates for a 0.05 m receiver tube diameter with a tracking error of 0° and optical error of 10 mrad.

Note that for $A' \approx 0.0035$, the accompanying optical efficiency at 0° tracking error is 99.6% and at 1° tracking error, the optical efficiency is 92.3% (see Fig. 4.1 and Fig. 4.2). The optimum system mass flow rate for an open solar thermal Brayton cycle as a function of concentrator diameter was found by Le Roux et al. (2012b) and can be approximated with Eq. (4.2):

$$\dot{m}_{opt} \approx -0.0002 D_{conc}^3 + 0.0097 D_{conc}^2 - 0.0626 D_{conc} + 0.1773$$

(4.2)

For a tube diameter of 0.0833 m, a mass flow rate of 0.08 kg/s and an inlet temperature of 1 000 K, the results are shown in Fig. 4.14 (0° tracking error) and Fig. 4.15 (1° tracking

error). These results are very similar to those presented in Fig. 4.12 and Fig. 4.13, except for the higher net heat transfer rates and lower temperatures.
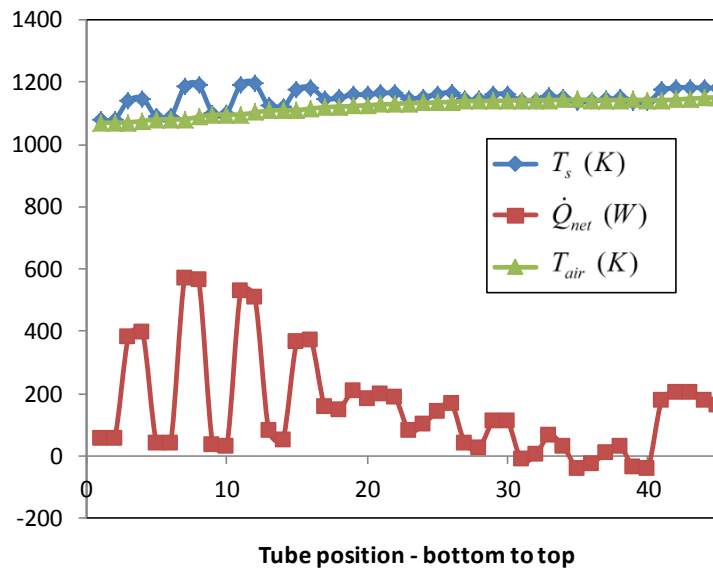
Figure 4.13 Temperatures and net heat transfer rates for a 0.05 m receiver tube diameter with a tracking error of 1° and optical error of 10 mrad.
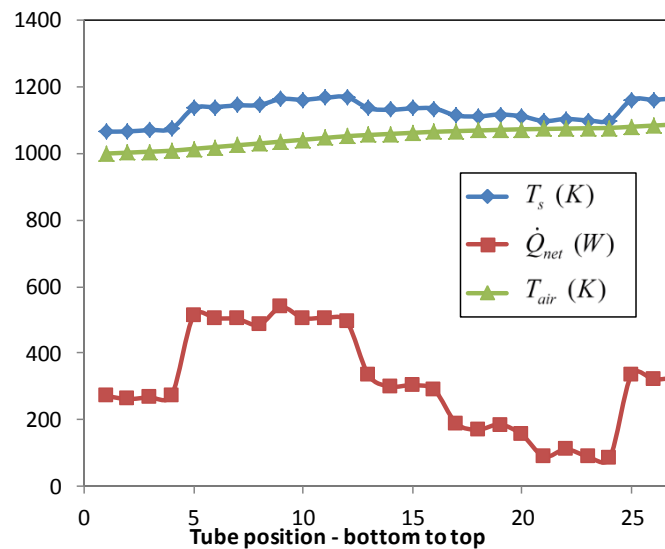
Figure 4.14 Temperatures and net heat transfer rates for a 0.0833 m receiver tube diameter with a tracking error of 0° and optical error of 10 mrad.

66
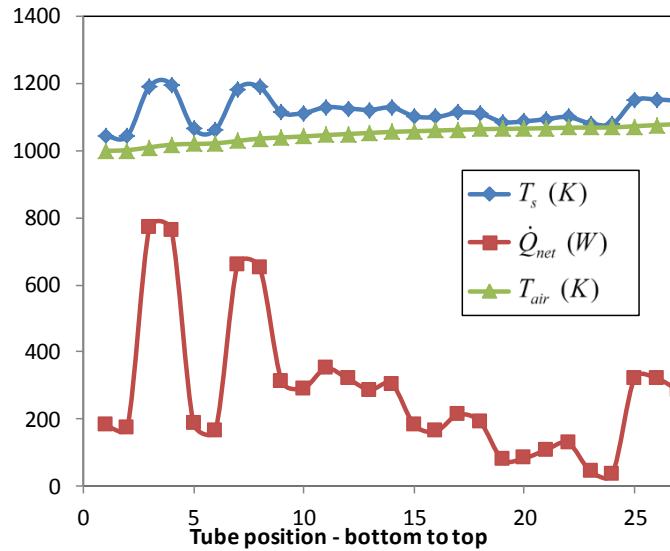
Figure 4.15 Temperatures and net heat transfer rates for a 0.0833 m receiver tube diameter with a tracking error of 1° and optical error of 10 mrad.

Tables 4.4-4.6 show the effects of mass flow rate, receiver tube air inlet temperature and tube diameter on the efficiency of the receiver (net heat transfer rate versus available solar power), pressure drop, and maximum receiver surface temperature. The receiver performance can be compared with the efficiencies of other solar receivers from the literature (Table 2.1).

Table 4.4 Efficiencies of the cavity receiver with $d = 0.05$ m.

		Tracking error = 0°				Tracking error = 1°				
$\dot{m}$ (kg/s)	$T_{in,0}$ (K)	η_{rec}	η_{2ndLaw}	$T_{s,max}$ (K)	$T_{s,ave}$ (K)	η_{rec}	η_{2ndLaw}	$T_{s,max}$ (K)	$T_{s,ave}$ (K)	ΔP (kPa)
0.06	900	0.66	0.67	1 083	1 032	0.65	0.66	1 069	1 024	56.0
0.06	1 000	0.57	0.70	1 159	1 113	0.54	0.69	1 153	1 104	56.0
0.06	1 070	0.50	0.72	1 214	1 169	0.47	0.71	1 211	1 160	56.0
0.07	900	0.69	0.62	1 064	1 016	0.66	0.61	1 050	1 009	75.1
0.07	1 000	0.58	0.65	1 143	1 099	0.56	0.64	1 136	1 092	75.1
0.07	1 070	0.51	0.67	1 199	1 157	0.48	0.66	1 196	1 150	75.1
0.08	900	0.70	0.55	1 049	1 004	0.69	0.54	1 037	998	97.0
0.08	1 000	0.60	0.58	1 130	1 089	0.57	0.57	1 124	1 082	97.0
0.08	1 070	0.52	0.60	1 187	1 148	0.48	0.58	1 185	1 141	97.0

67

Table 4.5 Efficiencies of the cavity receiver with d = 0.0625 m.

		Tracking error = 0°				Tracking error = 1°				
$\dot{m}$ (kg/s)	$T_{in,0}$ (K)	η_{rec}	η_{2ndLaw}	$T_{s,max}$ (K)	$T_{s,ave}$ (K)	η_{rec}	η_{2ndLaw}	$T_{s,max}$ (K)	$T_{s,ave}$ (K)	ΔP (kPa)
0.06	900	0.64	0.73	1 100	1 049	0.61	0.72	1 098	1 035	17.2
0.06	1 000	0.55	0.75	1 178	1 128	0.51	0.75	1 179	1 113	17.2
0.06	1 070	0.48	0.77	1 233	1 182	0.45	0.77	1 236	1 168	17.2
0.07	900	0.66	0.71	1 079	1 033	0.62	0.70	1 079	1 020	23.0
0.07	1 000	0.57	0.74	1 160	1 113	0.52	0.73	1 163	1 101	23.0
0.07	1 070	0.50	0.76	1 217	1 170	0.46	0.75	1 221	1 157	23.0
0.08	900	0.68	0.69	1 063	1 020	0.65	0.68	1 064	1 008	29.6
0.08	1 000	0.58	0.72	1 146	1 102	0.55	0.71	1 149	1 091	29.6
0.08	1 070	0.51	0.74	1 204	1 160	0.47	0.73	1 209	1 149	29.6

Table 4.6 Efficiencies of the cavity receiver with d = 0.0833 m.

		Tracking error = 0°				Tracking error = 1°				
$\dot{m}$ (kg/s)	$T_{in,0}$ (K)	η_{rec}	η_{2ndLaw}	$T_{s,max}$ (K)	$T_{s,ave}$ (K)	η_{rec}	η_{2ndLaw}	$T_{s,max}$ (K)	$T_{s,ave}$ (K)	ΔP (kPa)
0.06	900	0.61	0.75	1 129	1 080	0.60	0.75	1 154	1 067	3.73
0.06	1 000	0.52	0.78	1 203	1 153	0.50	0.78	1 231	1 141	3.73
0.06	1 070	0.45	0.80	1 254	1 205	0.43	0.80	1 285	1 193	3.73
0.07	900	0.63	0.75	1 108	1 062	0.62	0.75	1 133	1 051	4.99
0.07	1 000	0.53	0.78	1 185	1 138	0.52	0.78	1 213	1 127	4.99
0.07	1 070	0.48	0.79	1 238	1 191	0.45	0.79	1 268	1 181	4.99
0.08	900	0.64	0.75	1 091	1 047	0.64	0.75	1 037	1 116	6.41
0.08	1 000	0.55	0.78	1 170	1 126	0.54	0.77	1 197	1 116	6.41
0.08	1 070	0.48	0.79	1 225	1 181	0.46	0.79	1 254	1 171	6.41

It is concluded that the higher the inlet temperature, the less efficient the receiver becomes and the higher the maximum receiver surface temperature. For the tracking error of 1°, the receiver efficiency and average surface temperature are lower. For higher efficiency, lower inlet temperatures are beneficial so that lower surface temperatures are present. However, for

the Brayton cycle, a larger outlet temperature would be beneficial. Thus, a high receiver efficiency is not necessarily beneficial for the system as a whole. It is also concluded that the higher the mass flow rate, the lower the surface temperatures and the more efficient the receiver. This was also found in the literature by Kribus et al. (1999) and Hischier et al. (2009). Again, note that a higher mass flow rate is not necessarily beneficial for the system as a whole, since the pressure drop increases and the outlet temperature decreases.

4.2.1.4 Effect of wind

The effect of wind on the net heat transfer rate and tube surface temperature profile is shown by comparing Fig. 4.16 with Fig. 4.14. It is assumed that the convection heat transfer coefficient is roughly 10 times the natural convection heat transfer coefficient. The collector efficiency comes down to 10%, which shows that the effect of wind should be considered when modelling the cavity receiver.
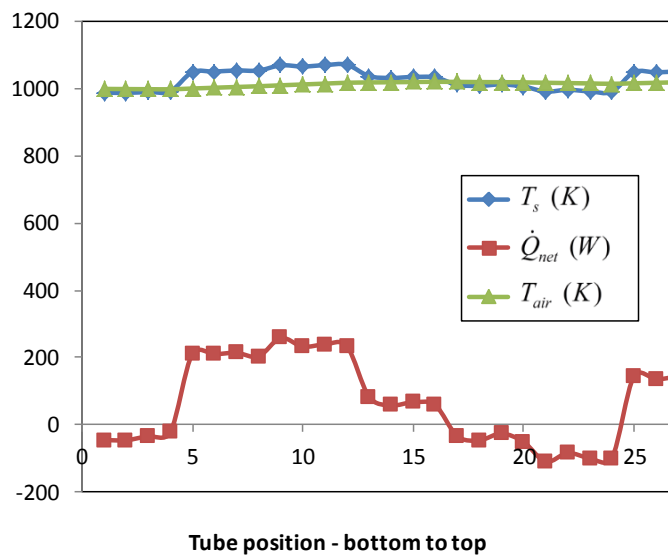
Figure 4.16 Temperatures and net heat transfer rates for a 0.0833 m receiver tube diameter with a tracking error of 0°, optical error of 10 mrad and excessively heavy wind.

4.2.1.5 Entropy generation rate due to the solar receiver

The second law efficiency is presented in Tables 4.4-4.6 as a function of mass flow rate and receiver tube size. The second law efficiency shown in Eq. (3.8) can be used as an indicator to choose the optimum receiver tube diameter where P_{in} can be assumed to be 180 kPa (Le Roux et al., 2012b). In Tables 4.4-4.6, η_{2ndLaw} increases as d and $T_{in,0}$ increase while η_{rec}

69

decreases, indicating that a large tube diameter is beneficial in a small-scale open solar thermal Brayton cycle. The smaller tube diameter allows for higher efficiency but due to the high pressure drop, a much lower second law efficiency is obtained, which indicates that a larger tube would be more beneficial. As the mass flow rate increases, η_{rec} increases, while η_{2ndLaw} decreases or stays constant when the tube diameter is large. The highest η_{2ndLaw} was found when the tube diameter and inlet temperature are large and the mass flow rate is small. However, these variables would also create a very high surface temperature. If the surface temperature is restricted to 1 200 K, a larger mass flow rate and lower inlet temperature can still provide high second law efficiencies, when a large tube diameter is used.

4.2.2 Optimum performance of the open solar thermal Brayton cycle

In the previous section, the performance of the open-cavity tubular solar receiver was investigated. In this section, the performance of the open solar thermal Brayton cycle with open-cavity tubular receiver and counterflow plate-type recuperator is investigated. The goal of this work was to determine, with Eq. (3.2) as objective function, the optimum receiver tube diameter and counterflow recuperator geometries of a small-scale open and direct solar thermal Brayton cycle with 4.8 m diameter parabolic dish with 1° tracking error, 10 mrad optical error and $A' = 0.0035$, so that the net power output of the system is a maximum. The method of total entropy generation minimisation was used to maximise the power output by simultaneously optimising the geometry variables of the receiver and recuperator. The temperatures and net absorbed heat rates at different parts of the receiver tube were found by solving multiple equations using numerical methods as discussed in the previous section.

Limiting factors to the performance of the solar thermal Brayton cycle include maximum receiver surface temperature and recuperator weight. It is often beneficial for the cycle to have a large recuperator, however, the recuperator should be practical. The turbine operating point was used as parameter in the objective function so that the maximum of the objective function can be found at different parameter values. The compressor isentropic efficiency and shaft speed were obtained with interpolation from the compressor maps. With the use of the compressor and turbine maps, the temperatures and pressures at every point of the system were found with the use of iteration and by modelling every component as discussed in Chapter 3. Five different micro-turbines were also considered. Different combinations of the five micro-turbines by Garrett (2014), three different receiver tube diameters and 625

70

differently sized recuperators were used as parameters and variables to determine the net power output of the system.

Matlab was used to determine the combinations of the parameters and variables which would give the best results. The recuperator variables were the width of the recuperator channel, *a*, the height of a recuperator channel, *b*, the length of the recuperator, *L*, and the number of flow channels in one direction, *n*. The basic structure of the Matlab program was as follows, where *d* is the receiver tube diameter:

For *d* = 0.05, 0.0625 or 0.0833,

  For *MT* = 1:5,

    For the different operating points of each turbine,

     For 625 different recuperators,

      Find temperatures and pressures in the cycle with iteration

      Find net power output of the system

It was assumed that the tube going to and from the receiver was 6 m long with 10 mm insulation thickness and insulation conductivity of 0.18 W/mK. A solar DNI of 1 000 W/m^2 was assumed and a dish reflectivity of 85%. A constraint on the system optimisation was the maximum receiver surface temperature, which was constrained to 1 200 K. A second constraint was the recuperator total plate mass, which was restricted to either 300 kg, 400 kg or 500 kg. The recuperator material was stainless steel.

Note that the compressor isentropic efficiency, compressor corrected mass flow rate, compressor pressure ratio and rotational speed are intrinsically coupled and are available from the compressor map.

4.2.2.1 Results

In Figs. 4.17-4.21, the maximum net power output of the systems at steady state was found with Eqs. (3.2), (3.28) and (3.31) in Matlab. It is shown that for the 4.8 m diameter solar dish with 0.25 m x 0.25 m receiver aperture area, a receiver tube diameter of 0.0833 m will give the best results as was also found in Section 4.2.1.5. In the results, note that each data point represents a maximum, which is achieved using a unique recuperator. Each data point is at a different turbine pressure ratio. Note that in these results, the recuperator mass was restricted to 500 kg and the maximum receiver surface temperature was constrained to 1 200 K.

In Figs. 4.17-4.21, it is shown that as the turbine pressure ratio increases, the maximum net power output increases up to a maximum. This effect is mostly due to a combination of compressor and turbine efficiencies which are a maximum when within a certain flow range and pressure ratio. It is also shown that for larger receiver tube diameters, a higher maximum net power output can be achieved at high turbine pressure ratios. Note that in Section 4.2.1.5, it was found that the highest second law efficiencies for the receiver were achieved when the tube diameter and inlet temperature were large and the mass flow rate small. This combination of variables would also create a very high surface temperature. When the surface temperature is then restricted to 1 200 K, a larger mass flow rate and lower inlet temperature can still provide high second law efficiencies, when a large tube diameter is chosen. Also note that in the solar thermal Brayton cycle, the larger the receiver tube diameter, the smaller the pressure drop through it and thus the more power is available at the turbine. In Figs. 4.17-4.21 it is also shown that the curves are not smooth. This is due to the efficiencies of the compressor and turbine which are sensitive to flow and pressure changes. Also note that, for the model, the compressor efficiencies were interpolated from a compressor map. Note that different recuperators are depicted in each data point. The recuperator efficiency influences the inlet temperature to the receiver which influences receiver efficiency, maximum receiver surface temperature and turbine power. The compressor power and compressor efficiency is in turn dependent on turbine power. The curves are thus also not smooth because of the different recuperators used and due to the maximum receiver surface temperature restriction.
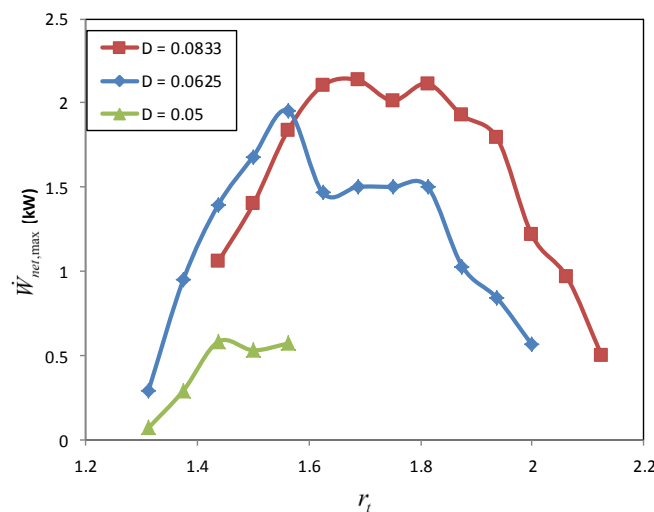
Figure 4.17 Maximum net power output of the system for $MT = 1$.
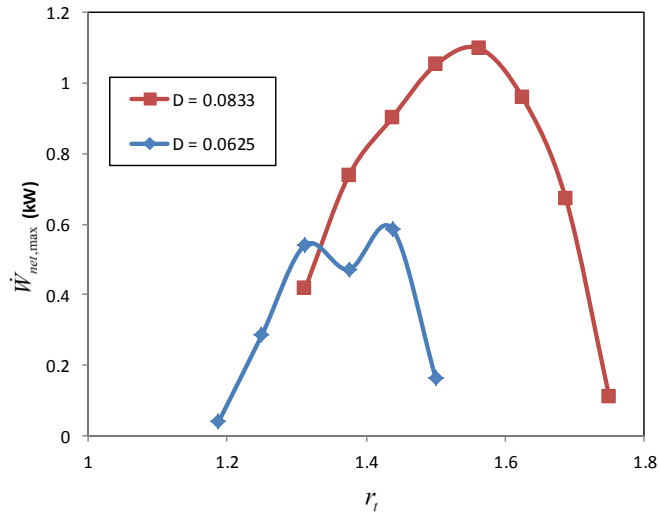
Figure 4.18 Maximum net power output of the system for *MT* = 2.
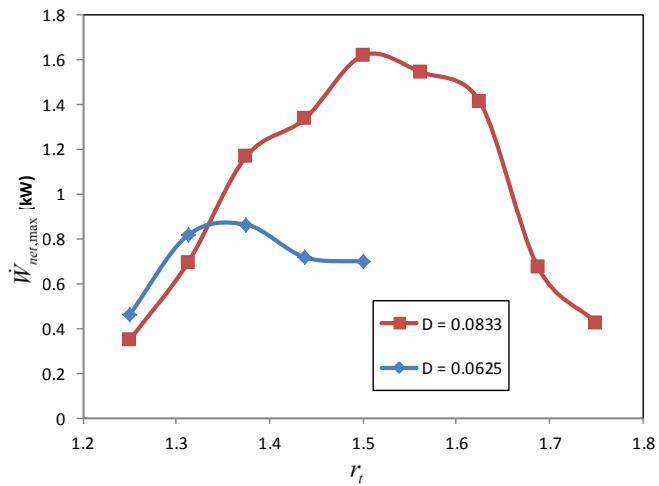
Figure 4.19 Maximum net power output of the system for *MT* = 3.
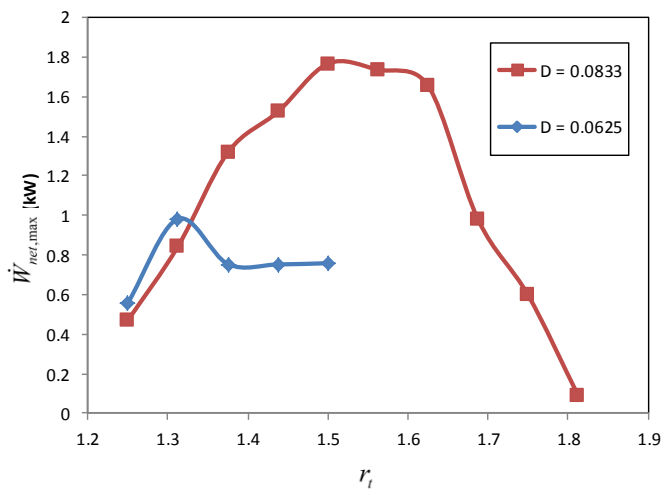
Figure 4.20 Maximum net power output of the system for *MT* = 4.

73

Table 4.7 Optimum recuperator geometries, maximum net power output, maximum receiver surface temperature and recuperator mass for *MT* = 5 and receiver tube diameter, *d* = 0.0833 m.

r_t	a (m)	b (m)	L (m)	n	$\dot{W}_{net,\max}$ (W)	$T_{s,max}$ (K)	Mass (kg)
1.688	0.15	0.005	1.5	15	946	1 178	111.2
1.75	0.225	0.005	1.5	15	1 168	1 198	165.2
1.813	0.3	0.005	1.5	15	1 353	1 198	219.2
1.875	0.45	0.005	1.5	15	1 575	1 198	327.2
1.938	0.45	0.004	2.25	15	1 808	1 196	490
2	0.15	0.003	2.25	45	1 848	1 199	495.7
2.063	0.225	0.002	1.5	45	1 991	1 196	489.2
2.125	0.225	0.002	1.5	45	2 058	1 170	489.2
2.188	0.225	0.002	1.5	45	2 110	1 134	490.9
2.25	0.225	0.002	1.5	45	1 714	1 111	490.9
2.313	0.225	0.002	1.5	45	1 662	1 087	490.9
2.375	0.225	0.002	1.5	45	1 577	1 075	489.2
2.438	0.225	0.002	1.5	45	1 571	1 046	490.9
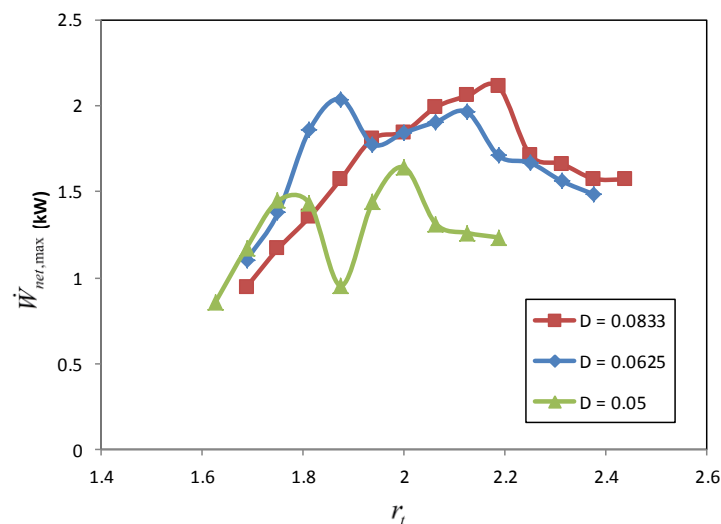
Figure 4.21 Maximum net power output of the system for *MT* = 5.

Table 4.7 shows the optimum geometries for a system with *MT* = 5 and a receiver tube diameter of 0.0833 m (compare with Fig. 4.21). For each turbine pressure ratio shown in Table 4.7, a maximum net power output is given with responsible recuperator geometry. The

74

maximum receiver surface temperature and recuperator mass are also given. Table 4.7 shows that a recuperator with $a = 225$ mm, $b = 2.25$ mm, $L = 1.5$ m and $n = 45$ was the best-performing recuperator since it gave the highest maximum net power output of 2.11 kW. These optimum recuperator geometries were also found at most of the turbomachines considered when a receiver tube diameter of 0.0833 m was used and the recuperator mass was restricted to 500 kg. Also note that the maximum receiver surface temperature was restricted to 1 200 K.
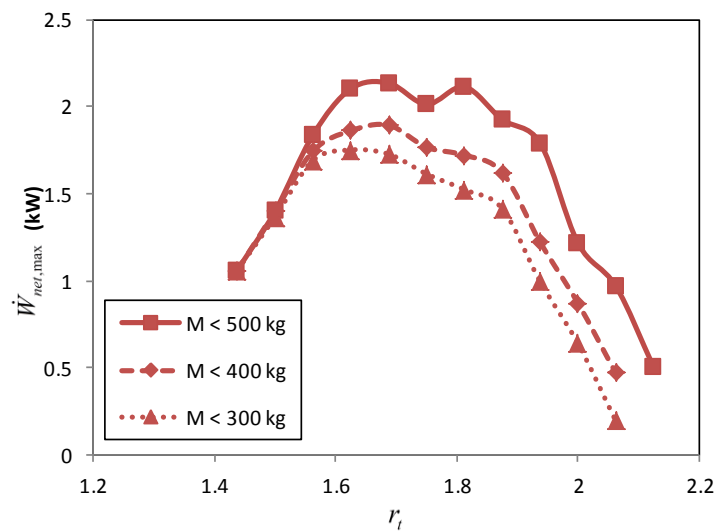
Figure 4.22 Maximum net power output of the system for *MT* = 1 with different recuperator mass constraints.
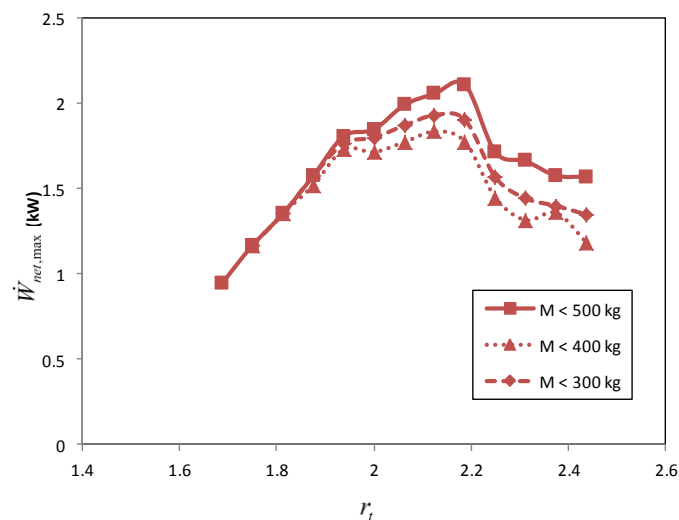
Figure 4.23 Maximum net power output of the system for *MT* = 5 with different recuperator mass constraints.

75
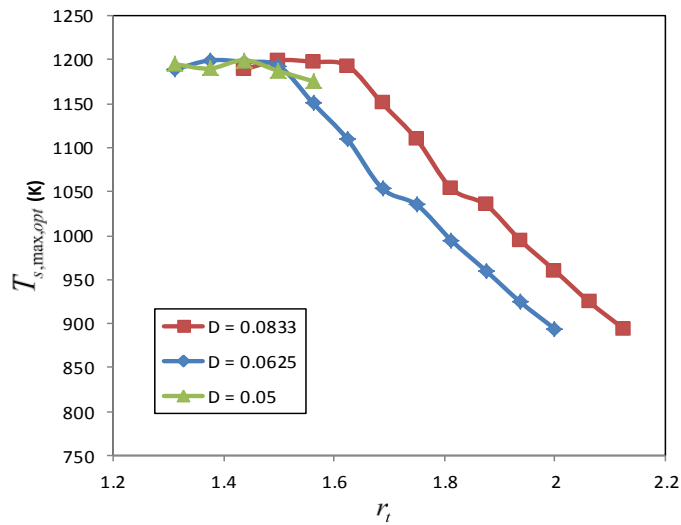
Figure 4.24 Optimum maximum receiver tube surface temperature at different operating temperatures for *MT* = 1.
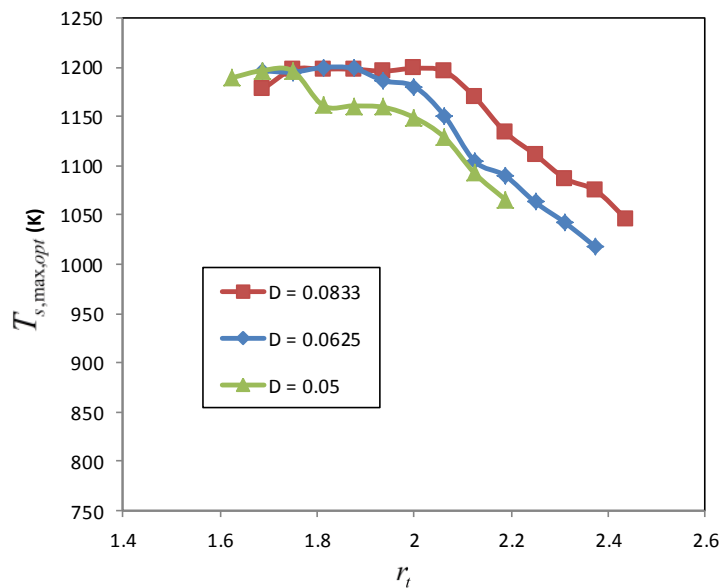
Figure 4.25 Optimum maximum receiver tube surface temperature at different operating temperatures for *MT* = 5.

The larger the mass of the recuperator, the higher the net power output of the system as shown in Fig. 4.22 and Fig. 4.23. When the recuperator mass was constrained to 400 kg, a recuperator with $a = 150$ mm, $b = 2.25$ mm, $L = 1.5$ m and $n = 45$ was found to be the most common optimum. When the recuperator mass was constrained to 300 kg, a recuperator with $a = 150$ mm, $b = 2.25$ mm, $L = 1.5$ m and $n = 37.5$ was best.

From Fig. 4.24 and Fig. 4.25, it is shown that it is optimum for the maximum receiver tube surface temperature to decrease with increasing turbine pressure ratio and with decreasing receiver tube diameter.

4.2.2.2 Summary

It was found that a 0.0833 m tube diameter should be sufficient for the small-scale open solar thermal Brayton cycle with a 4.8 m dish diameter. This tube gave acceptable results when used with the different turbomachines. Larger tube diameters can also be studied for future work. It was found that a recuperator with $a = 225$ mm, $b = 2.25$ mm, $L = 1.5$ m and $n = 45$ gave the best results for this set-up with mass constraint and receiver maximum surface temperature constraint. The large receiver tube diameter allows for higher receiver surface temperatures at higher turbine pressure ratios.

4.3 Flownex results

Flownex was used as a tool for comparison of the results of the performance of the small-scale open solar thermal Brayton cycle as found analytically using Matlab. Case studies were carried out and compared with the results found analytically.

A receiver tube diameter of 0.0833 m was used and the micro-turbine GT2560R was selected. Different steady-state operating speeds of the micro-turbine were considered. The recuperator channel cross-section was chosen as 0.5 m x 0.002 m with 40 channels in one flow direction. The recuperator length was chosen as 0.6 m. The results as found with the Matlab model and with Flownex are shown in Table 4.8 and Table 4.9 with node reference to Fig. 2.1.

The temperature results in Table 4.8 are also shown in Fig. 4.26 where the results generated with Matlab and Flownex are compared. The results show that for the calculation of the steady-state temperatures and pressures, there is good comparison between the Matlab results and Flownex results of within 8%, except for the recuperator outlet temperature. Note that in Matlab, the ε-*NTU* efficiency was calculated with heat loss to the environment added, while Flownex uses the simple ε-*NTU* method. The difference in recuperator outlet temperature can thus be expected.

Table 4.10 shows that there is a slight difference in the calculation between the shaft speed and mass flow rate. Compressor and turbine maps were inserted into Matlab and Flownex in different ways by reading from the maps visually. These errors will contribute to differences in the calculation of the shaft speed and mass flow rates.

Table 4.8 Flownex and Matlab results for the system at 87 000 rpm (GT2560R).

Node	Temperature				Pressure		
	Flownex		Matlab	Difference in	Flownex	Matlab	Difference in
	Degrees Celsius (˚C)	Kelvin (K)	Kelvin (K)	value (%)	Pressure (kPa)	Pressure (kPa)	value (%)
1	27	300.2	300.2	0	86	86	0
2	90.2	363.4	363.2	0.178	130.1	132.8	2.06
3	90.2	363.4	363.2	0.178	130.1	132.8	2.06
4	657	930.2	941.8	1.769	129.7	132.4	2.097
5	657	930.2	941.7	1.754	129.3	132.2	2.220
6	778.4	1 051.6	1047	0.531	127.3	130.2	2.286
7	778.4	1 051.6	1047	0.545	127.1	129.9	2.211
8	717.5	990.7	976.4	1.990	86.6	86.61	0.012
9	717.5	990.7	976.4	1.990	86.6	86.61	0.012
10	158.2	431.4	393.9	23.69	86	86	0

Table 4.9 Flownex and Matlab results for the system at 85 000 rpm (GT2560R).

Node	Temperature				Pressure		
	Flownex		Matlab	Difference in	Flownex	Matlab	Difference in
	Degrees Celsius (˚C)	Kelvin (K)	Kelvin (K)	value (%)	Pressure (kPa)	Pressure (kPa)	value (%)
1	27	300.2	300.2	0	86	86	0
2	83.64	356.8	359.0	2.614	128	128.0	0.039
3	83.64	356.8	359.0	2.614	128	128.0	0.039
4	666.9	940.0	991.9	7.777	127.8	127.8	0.0156
5	666.9	940.0	991.8	7.763	127.5	127.6	0.0549
6	784.5	1 058	1 094	4.704	125.7	125.8	0.0636
7	784.5	1 058	1 094	4.684	125.5	125.5	0.00797
8	725.5	998.6	1 026	3.805	86.2	86.21	0.0116
9	725.5	998.6	1 026	3.805	86.2	86.21	0.0116
10	149.2	422.3	389.1	22.31	86	86	0
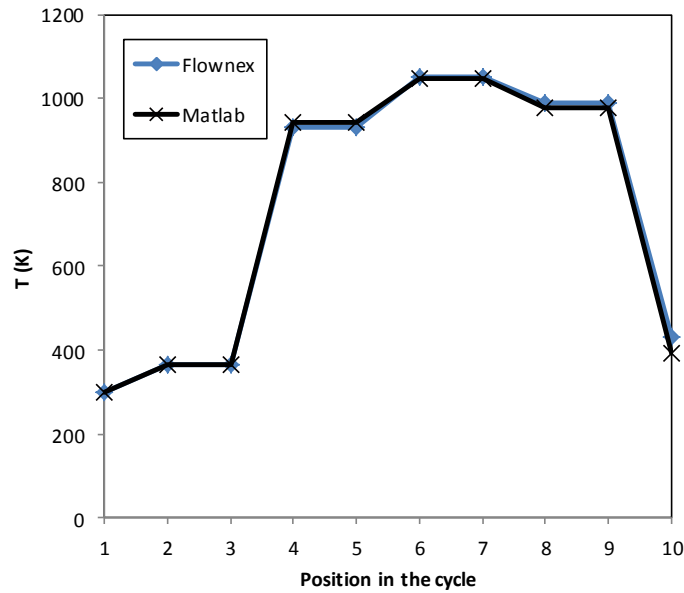
Figure 4.26 Predicted temperatures with the Matlab model and Flownex model at the different positions in the open solar thermal Brayton cycle using micro-turbine GT2560R at 87 000 rpm with reference to Fig. 2.1.

Table 4.10 Flownex and Matlab parameter results at steady state (GT2560R).

Chosen shaft speed (rpm)	87 000		85 000	
	Matlab	Flownex	Matlab	Flownex
Calculated shaft speed (rpm)	89 800	87 000	85 926	85 000
Calculated mass flow rate (kg/s)	0.0645	0.065	0.0593	0.060

4.4 Summary

The performance and optimised components of a dish-operated small-scale open solar thermal Brayton cycle were determined in this chapter. As discussed in Chapter 3, the results were generated in Matlab with the use of the method of total entropy generation minimisation and SolTrace while numerical results were generated with Flownex. The results showed that for the recuperated open solar thermal Brayton cycle with dish optical error of 10 mrad and a solar tracking error of 1° to be successful, the area ratio should be $A' \approx 0.0035$. It was shown that a tracking error of 2° would not be acceptable for the open solar thermal Brayton cycle. It was recommended that a cost-effective high-temperature receiver coating for low emissivity should be developed as such a coating would be very beneficial for the performance of the cycle.

79

It was shown that the open-cavity tubular solar receiver surface temperature and net heat transfer rate for heating air would depend on the receiver size, mass flow rate through the receiver, receiver tube diameter, receiver inlet temperature and dish errors. Receiver efficiencies of between 43% and 70% were found for the open-cavity tubular receiver with $0.06 \text{ kg/s} \leq \dot{m} \leq 0.08 \text{ kg/s}$, $0.05 \text{ m} \leq d \leq 0.0833 \text{ m}$, $900 \text{ K} \leq T_{in,0} \leq 1\,070 \text{ K}$ operating on a dish with 10 mrad optical error and maximum solar tracking error of 1°. Results showed that a smaller receiver tube diameter allowed for higher efficiency but due to the high pressure drop, a much lower second law efficiency was obtained, which indicated that a larger receiver tube diameter would be more beneficial for the small-scale open solar thermal Brayton cycle.

A 0.0889 m tube diameter was found to be sufficient for the small-scale open solar thermal Brayton cycle with a 4.8 m dish diameter for all five micro-turbines considered in the study. It was found that a recuperator with $a = 225$ mm, $b = 2.25$ mm, $L = 1.5$ m and $n = 45$ gave the best results for the set-up with mass constraint of 500 kg and receiver maximum surface temperature constraint of 1 200 K.

The results showed that for the calculation of the steady-state temperatures and pressures, there was good comparison between the Matlab results and Flownex results (within 8%) except for the recuperator outlet temperature, since different $\varepsilon\text{-}NTU$ methods were used to calculate the recuperator efficiency.

CHAPTER 5
EXPERIMENTAL STUDY

_____

5.1 Introduction

A solar dish and receiver were constructed to test the optimised solar receiver as found in Chapter 4 and to determine whether its performance can be modelled with the provided modelling tools. The optimum tube diameter found in Chapter 4 was quite large relative to tube diameters used in receiver heat loss models as discussed in the literature. The receiver was therefore tested to determine any discrepancies from the heat loss model used. The geometry-dependent effects and temperature-dependent effects on the receiver performance were investigated with a blower test and with a high-temperature test. The solar collector, consisting of the solar dish and receiver, plays a very important role in determining the success of the open solar thermal Brayton cycle, as it acts as the heat source in the cycle. In this chapter, the challenges and errors associated with the construction of a solar collector for an open solar thermal Brayton cycle are discussed. The use of SolTrace and the heat loss models presented in Chapter 3 is validated to a certain extent.

5.2 Experimental set-up

A two-axis solar tracking system, solar dish and receiver were constructed to test the optimised solar receiver as found in Chapter 4 and to determine whether its performance could be modelled with the provided tools. A parabolic dish with tube diameter of 4.8 m and a tubular cavity receiver with diameter of 0.0889 m were constructed.

5.2.1 Two-axis solar tracker

A two-axis solar tracking system was designed and built on the roof of the Engineering 2 Building at the University of Pretoria (Fig. 5.1). The two-axis solar tracking system allowed a parabolic dish and receiver to rotate in the azimuth axis and to slide along two six-metre beams to position itself towards the elevation of the sun, using winch motors. Since most commercially available solar tracking sensors, as well as the self-developed sensor discussed in Section 2.3.1, have a tracking error of $1° – 2°$, electronic tracking sensors were not used in the experimental tests as they were not accurate enough, according to results found in Chapter 4. As a result, the solar tracking was done manually every minute or two during the experiments by positioning the collector in such a way that the shadow of the receiver was

81

exactly in the middle of the dish. By doing this, the tracking error was expected to be less than 1° since the tracking error would be

$$\gamma = \tan^{-1}(\tau/f_c) = \tan^{-1}(0.05/2.897) = \tan^{-1}(0.0173) \approx 1° \tag{5.1}$$

if the receiver shadow was allowed a maximum play of 50 mm off its position at the centre of the dish.

Figure 5.1 Construction of the two-axis solar tracking system.

Other errors due to receiver positioning and tilting of the dish support beam could not be determined. However, by positioning the collector manually, these errors were also accounted for.

5.2.2 Solar dish

A 4.8 m aluminium parabolic dish with rim angle of 45° was designed and built for the experimental set-up (Fig. 5.2 and Fig. 5.3). The dish focuses concentrated sunrays onto a central point. The dish and the solar tracking structure were designed to handle a wind loading of 140 km/h. The design, manufacturing and installation of the dish created the opportunity to better understand the errors associated with the solar collector.

Polished aluminium alloy arms (Alloy 5754) and mill-finished pure aluminium sheets (Alloy 1050 H12/H24 - more than 99.5% Al) were used to construct the dish. The polished aluminium alloy arm sections were laser cut to the correct profile and were then welded to create the 12 tubular arms. The 12 arms were joined together in the middle of the dish with two base plates clamping them from the top and the bottom (Fig. 5.2). Note that the top

82

reflecting surfaces of the arms had a different parabolic function than the bottom surfaces where the sheets were attached so that all the reflective surfaces had the same focal point.

Figure 5.2 Assembly of the 4.8 m diameter parabolic solar dish in the laboratory (upside down).

Figure 5.3 Test set-up as modelled in SolidWorks and as constructed showing the solar dish on the two-axis solar tracking system.

For the mill-finished pure aluminium sheets, 1.2 mm sheet thickness was used to prevent hail damage. The 12 sheet segments were also laser cut from 2.5 m x 1.25 m aluminium sheets and were shaped during installation by riveting them onto the bottom of the positioning arms with aluminium large-flange blind rivets. The parabolic shape of the dish is shown in Fig. 2.6 where $R = 2.4$ m and the rim angle is 45°. The focal length is calculated with Eq. (2.2) as

$$f_c = \sqrt{\frac{(1+\cos 45)^2 \pi(2.4)^2}{4\pi \sin^2 45}} = 2.897 \text{ m} \tag{5.1}$$

For a 45° rim angle, $f_c = H + R$, and thus $H = 0.497$ m. According to Eq. (2.3), $a = H / R^2 = 0.0863$. The derivative of the function or the slope of the dish is $y' = 2ax$. Thus, the slope angle is calculated with Eq. (5.2) as 22.5° for $x = 2.4$ m. The slope error was also calculated similarly as shown below.

$$\zeta = \tan^{-1}(2ax) \tag{5.2}$$
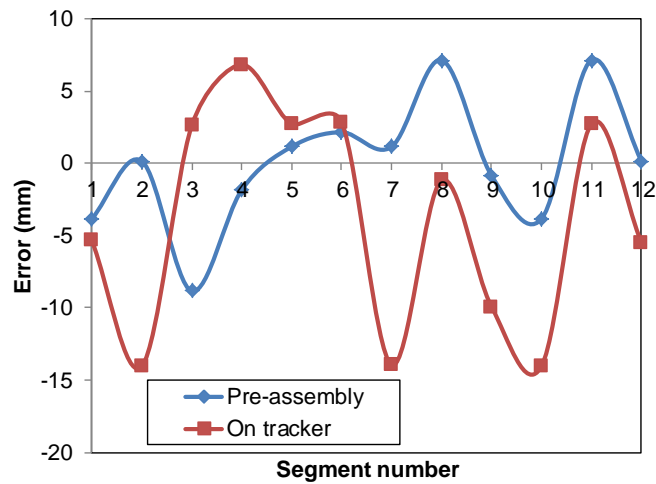
Figure 5.4 Measured error of the end-height of the 12 dish arms during pre-assembly and on the tracker.

The dish arms were assembled in storage (Fig. 5.2) and were again assembled on the solar tracker (Fig. 5.3). Theoretically, the end points of all 12 dish arms should be located at the same height, H, from the bottom base plate. Figure 5.4 shows the measured error in the height of each dish arm as assembled in the laboratory and on the roof. These errors translate into the slope error of the dish, which can be calculated with Eqs. (2.3) and (5.2). For example, a 15 mm error in the height of a dish arm creates a slope error of 10.6 mrad. The absolute slope error measured per arm is shown in Fig. 5.5 for the dish as installed on the solar tracking system. The average absolute slope error for the dish due to the arms was found to be 4.86 mrad. The surface finish and roughness on macro scale can also increase the slope error of the dish further, hence the slope error was estimated to be 5 mrad.

84
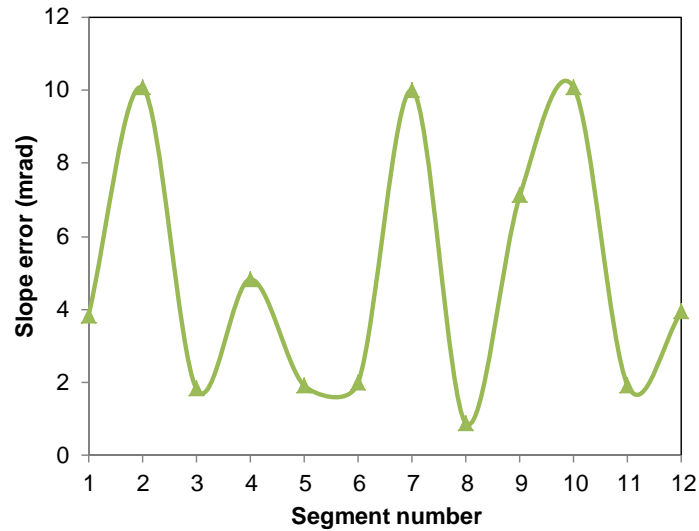
Figure 5.5 Absolute slope error per dish arm as installed on the solar tracking system.

5.2.3 Measurement of the solar resource
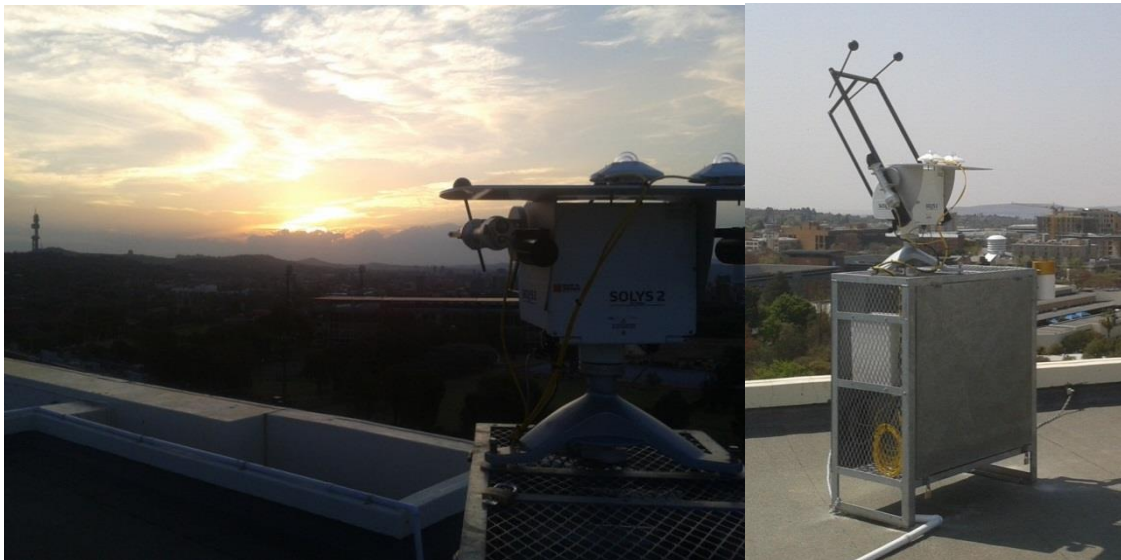
Figure 5.6 Solar measuring station to measure the DNI of the sun (SOLYS 2).

For the experiments, it was important to know exactly how much power was available from the sun at any moment to determine $\dot{Q}_{solar}$. The direct normal irradiance (DNI) was measured at a solar measuring station (SOLYS 2) available at the University of Pretoria (Fig. 5.6). The experiments were conducted during South Africa's winter season, which meant the sun's DNI and elevation were at their lowest. This station also took other important measurements such as wind speed, temperature and relative humidity. The data from the SOLYS 2 as

85

obtained during the experiments is shown in Appendix A. The accuracy of the solar measurements is assumed to be within 2% (Geuder et al., 2009). The sun's elevation and azimuth angles at the time of the experiments were available from SunEarthTools (2014) and are also shown in Appendix A.

5.2.4 Solar receiver

The solar receiver as discussed in Section 3.4.2 was constructed for the experimental set-up so that it could be placed at the focal point of the solar dish. The solar receiver was constructed by welding a number of 90-degree stainless steel (316) elbows and tubes with outer diameter of 0.0889 m, as shown in Fig. 5.7, to create the optimum aperture area of 0.25 m x 0.25 m, according to Section 4.2.1.1.

The receiver tube diameter of 0.0889 m was used because it was found to be the best tube diameter to perform in the open solar thermal Brayton cycle with a dish diameter of 4.8 m, according to Chapter 4. The tube diameter was quite large relative to the tubes in other receiver models discussed in the literature and it was therefore tested to determine any discrepancies from the heat loss models. The receiver was manufactured in-house at the University of Pretoria. The receiver top could not be manufactured as shown in Fig. 3.3 due to the difficult welding seams. As a result, a ceramic fibre insulation board was used at the top to reflect the sun's rays back onto the receiver tubes. Also, a gap of 10 mm between each receiver tube coil was required for welding purposes (Fig. 5.7 and Fig. 5.8).

Figure 5.7 Manufacturing of the solar receiver.

86
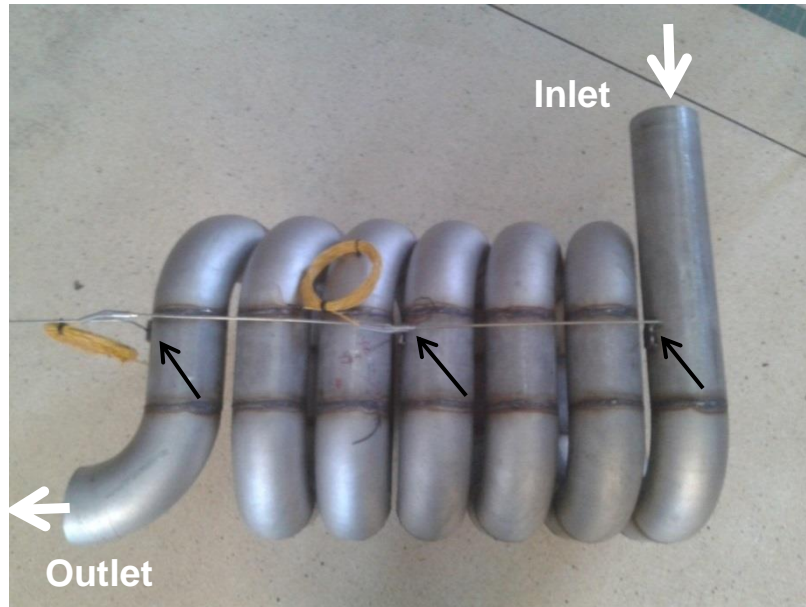
Figure 5.8 A side view of the solar receiver showing the position of the three weldpad thermocouples (black arrows) and the flow direction of the air (white arrows) from the bottom of the receiver (inlet) to the top (outlet).

Figure 5.9 The solar receiver positioned on the bottom insulation before being installed on the receiver structure.

The solar receiver was pressure tested to detect welding leakages until it was able to hold 1.5 bar gauge pressure for 1 minute. Three K-type weldpad thermocouples were welded onto the receiver surface at the inlet, outlet and in the middle of the receiver (Fig. 5.8) so that temperature measurements could be taken during the experiments. In Fig. 5.8, the receiver inlet is shown on the right and the outlet is shown on the left. The receiver height from the

bottom to the outlet was 765 mm and the receiver width was 427.8 mm. In the experiment, no coating was placed on the receiver. The receiver weight was calculated to be 50 kg.

The receiver was installed on the receiver structure of the solar tracker at the focal point of the solar dish. A 100 mm thick ceramic fibre insulation board (280 kg/m^3) and insulation blanket, able to withstand temperatures of 1 260 °C, were used to insulate the receiver from the side, top and bottom. The receiver rested on 614 x 614 mm ceramic fibre insulation board at the bottom with a 0.25 m x 0.25 m aperture (Fig. 5.9 and Fig. 5.10). In Fig. 5.9, the insulation boards at the back, left and bottom of the receiver are shown. The insulation thermal conductivity was 0.085 W/mK at 200 °C, 0.112 W/mK at 400 °C and 0.145 W/mK at 600 °C, according to the manufacturer's specifications.

Figure 5.10 Top view of the solar receiver with the aperture shown at the bottom.

Modelling of the receiver at high temperature (1 200 K) in SolidWorks showed that the receiver could coil upwards and radially during thermal expansion, but not more than 10 mm (Fig. 5.11). This thermal expansion of the receiver should be considered when it is connected to an inlet or outlet tube. A high-temperature flexible metal hose should be considered when connecting the receiver to perform in a small-scale open solar thermal Brayton cycle. The thermal expansion is also important when considering the insulation cover. The insulation boards were thus placed around the receiver to allow for thermal expansion. For the integration of the receiver into the open solar thermal Brayton cycle, the solar receiver should be specifically investigated for thermal expansion and fatigue loading due to creep.
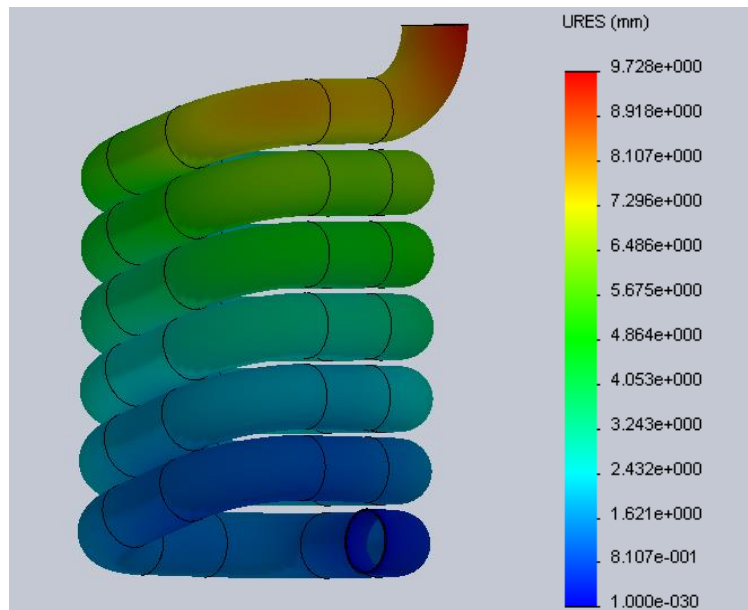
Figure 5.11 Thermal expansion of the solar receiver during operation as found with SolidWorks. The air inlet is at the bottom and the outlet at the top of the figure.

5.2.5 Blower

A 2 500 W leaf blower was used in the experiments. The blower was chosen for its mass flow rate which was close to typical mass flow rates found for the small-scale solar thermal Brayton cycle in the analytical study (see for example Table 4.6 and Table 4.10). The blower was attached to the inlet of the solar receiver. The blower was used to blow air through the inside of the receiver tube while the receiver was exposed to the solar heat flux. Six different blower speed settings were used. An anemometer (Kestrel 4 200 Pocket Air Flow Tracker) was used to determine the speed of the air flow. For each blower setting, five measurements were taken at five different positions of the outlet air flow to determine the average air speed. The average mass flow rates created by the blower at the different speed settings were determined as $\dot{m} = \rho AV$. These measurements at steady state are shown in Table 5.1. The accuracy of the flow meter was determined to be ±5% at worst, according to the manufacturer's specifications.

The elevation of Pretoria is 1 410 m and the average pressure fluctuates around 87 kPa. From this, the air density was calculated to be approximately 1 kg/m^3. Measurements were taken at the outlet of the solar receiver, with the blower attached to the solar receiver inlet (Table 5.1). The mass flow rates per speed setting as determined in Table 5.1 were used in calculations to determine the net absorbed heat rate of the solar receiver as discussed in the next section. The blower measurements were also taken indoors without the receiver attached to determine the

89

increase in air temperature due to the blower (Table 5.2). The increase in air temperature due to the blower was assumed negligible.

Table 5.1 Blower measurements outdoors with receiver attached.

Speed setting	Average velocity (m/s)	Ambient temperature (°C)	Density (kg/m^3)	Mass flow rate (kg/s)
1	16.4	23	1	0.0883
2	17.5	23	1	0.0944
3	18.3	23	1	0.0983
4	20.0	23	1	0.108
5	21.5	23	1	0.116
6	22.4	23	1	0.121

Table 5.2 Blower measurements indoors without the receiver attached.

Speed setting	Average velocity (m/s)	Room temperature (°C)	Outlet temperature (°C)	Temperature difference (°C)	Density (kg/m^3)	Mass flow rate (kg/s)
1	21.7	21	23	2	1	0.117
2	23.0	21	23	2	1	0.124
3	25.5	21	24	3	1	0.138
4	24.9	21	25	4	1	0.134
5	28.9	21	25	4	1	0.157
6	29.3	21	25	4	1	0.158

5.3 Experimental procedure

For the purpose of the experiment, low-cost mill-finished aluminium sheets with reflectivity of 55% (see Section 2.3.2) were used for the solar dish. These sheets are much safer for operation on an experimental set-up and were thus chosen to prevent damage to the receiver structure as a result of possible tracking error. This is similar to a very dirty polished aluminium dish, according to Fig. 2.5. These, low reflectivity and low specularity reflectors were only used for the purpose of this research and for comparison of results with SolTrace. However, for commercial purposes, a high-reflectivity and high-specularity reflector should be used. The experimental test set-up is shown in Fig. 5.12. Two different types of tests were performed, Test A and Test B.

90

5.3.1 Test A

Firstly, in Test A, the blower was used to blow air through the receiver at six different speed settings while the receiver was exposed to the solar heat flux from the solar dish. The receiver surface temperatures at the inlet, outlet and in the middle of the receiver tube were measured with the K-type thermocouples and the air temperature at the outlet of the receiver was measured with a T-type thermocouple in the outlet air stream. The purpose of Test A was to determine the optical efficiency of the collector to be used in Test B. Test A was performed to study the geometry-dependent factors contributing to the performance of the collector.

Figure 5.12 Layout of the experimental set-up.

1– Solar receiver with insulation; 2 – Leaf blower at receiver inlet; 3 – Receiver support structure; 4 – Parabolic dish; 5 – Thermocouple wires to data logger.

5.3.2 Test B

For Test B, a high-temperature test was performed. In this test, the blower and receiver-outlet thermocouple were removed and the inlet and outlet of the receiver were closed off with a

91

ceramic fibre insulation blanket to prevent heat loss due to natural convection. With the receiver at the focal point of the dish, the receiver temperatures were measured until steady-state temperatures were reached. The temperature on the surface of the insulation was also measured on one side in the middle of the receiver. Thus, in this test, there was no air flow through the receiver and the receiver could only lose heat through its aperture with convection and radiation and through the insulation with conduction. This test was performed to determine the convection heat loss coefficient on the inside of the cavity and to validate the use of SolTrace and the heat loss models used.

5.4 Experimental results

The results found from running Test A and Test B are presented in this section. The available solar power was measured with the solar measuring station (SOLYS 2) during the experiments. The data measured with the station during the experiments is shown in Appendix A. A datalogger with accuracy of within 0.5 °C was used to measure the temperatures and to store the data. Calibration showed that a further error of 1 °C could be expected from the thermocouples.

5.4.1 Test A, Blower Test
5.4.1.1 Results
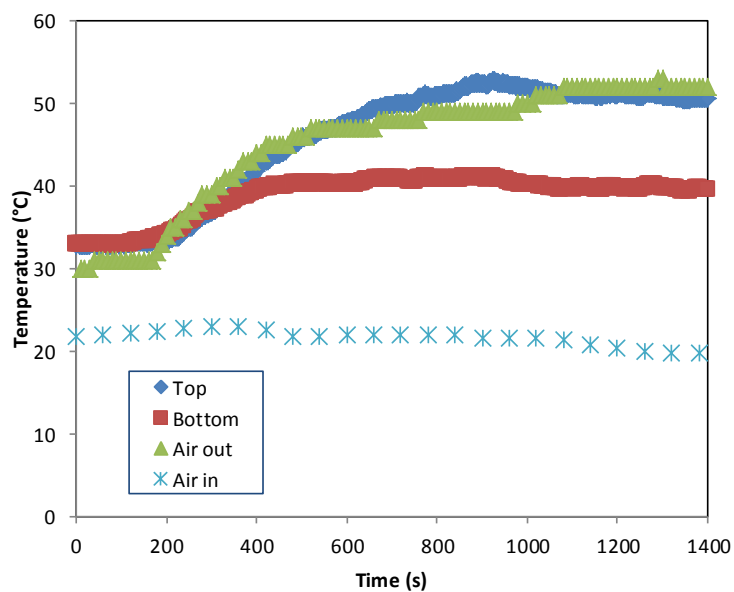
Figure 5.13 Receiver surface temperature and air temperature measurements at the inlet (bottom) and outlet (top) of the solar receiver with the blower on Speed Setting 6.

92
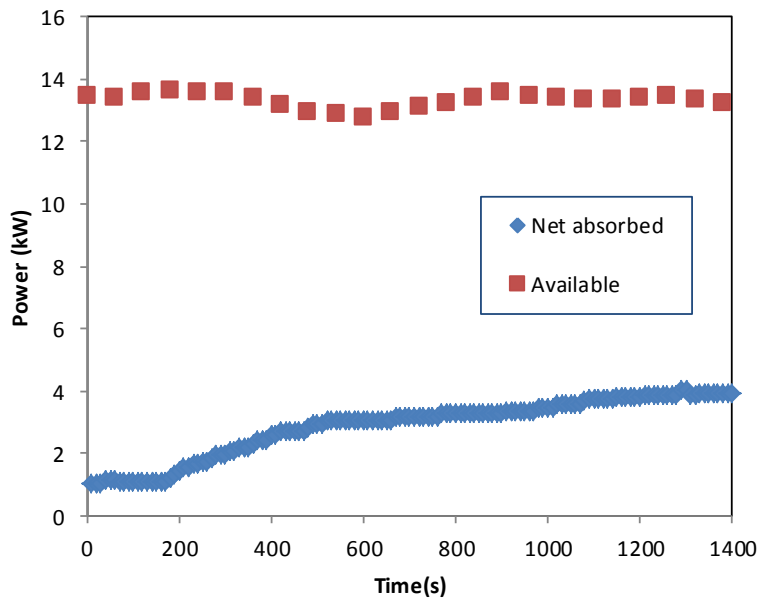
Figure 5.14 Net absorbed heat rate of the air in the solar receiver with the blower on Speed Setting 6.

Figure 5.13 shows the measured temperatures of the receiver inlet (bottom) and outlet (top) surfaces as well as the air temperature at the inlet (air in) and at the outlet (air out) of the receiver. These results were generated with the blower on Speed Setting 6 (see Table 5.1) and the experiment was performed on Day 1 (see Appendix A). The air outlet temperature was just above 50 °C. Figure 5.14 shows the net absorbed heat rate versus the available power from the sun. The net absorbed heat rate was determined with Eq. (5.3) since the heat loss rate from the receiver at these temperatures was assumed negligible. The mass flow rate from Table 5.1 was used for the calculation.

$$\dot{Q}_{net} = \dot{m}c_p \left(T_{out} - T_{in} \right) \tag{5.3}$$

The results show that the collector efficiency, η_{col}, equal to $\dot{Q}_{net} / \dot{Q}_{solar}$, was about 30% at steady state (Fig. 5.14). In this experiment, the receiver was only moved into the focal point of the dish after $t \approx 200$ s. Figure 5.15 shows the focal point of the dish on the receiver from the bottom of the receiver. The receiver tubes are illuminated and the blower is shown behind the heat shield. The measured temperatures at steady state are shown in Table 5.3 together with the steady-state temperatures of eight other tests performed on different days and with different speed settings. Some of these tests are discussed below. Figures 5.16 shows the

93

results when the blower was set to Speed Setting 1 (see Table 5.1). This test was also performed on Day 1 (see Appendix A). The air outlet temperature was again close to 50 °C. Note that the collector efficiency at steady state was found to be 23.2%.

Figure 5.15 A view from the bottom: the illuminated receiver at the focal point of the dish during an experiment with the blue sky in the background.

Table 5.3 Steady-state receiver surface temperature and air temperature measurements at the inlet, outlet and in the middle of the receiver (see Appendix A and Table 5.1).

Day	1	1	2	2	2	3	3	3	3
Blower setting	6	1	5	4	3	2	4	4	3
Start time	12:37	14:36	11:18	12:27	14:26	10:13	11:24	12:25	14:28
Steady-state time	13:00	14:56	11:34	12:52	14:40	10:41	12:01	12:45	14:41
Receiver inlet (°C)	39.2	38.8	35.5	38.4	35.9	35.5	-	38.0	36.2
Receiver middle (°C)	45.5	44.9	41.7	45.7	44.4	44.6	-	46.6	45.0
Receiver outlet (°C)	50.4	50.6	46	54.1	50.0	50.1	-	52.2	48.0
Air ambient (°C)	19.8	20.4	17	16.4	18.6	15.9	18.4	19.1	19.9
Air outlet (°C)	52	51	42	49	49	46	50	52	45.0
Collector efficiency (%)	29.5	23.2	19.9	24.9	22.4	21.0	25.3	26.3	21.2
Optical efficiency (%)	53.6	42.2	36.2	45.3	40.7	38.2	46.0	47.8	38.5

In Fig. 5.17, the temperature rise of the receiver is shown with the blower on Speed Setting 5 (Day 2). The steady-state temperatures are noted in Table 5.3. Figure 5.18 shows that it took long for the receiver to reach its initial temperature after a test. In this test, the speed setting

was changed from Speed Setting 2 to Speed Setting 4 at 3 630 s (11:10, Day 3). At 4 500 s (11:24), the receiver was moved into the focal point after resting in the horizontal position. Figure 5.19 shows the net absorbed heat rate. Table 5.3 shows the steady-state temperatures.
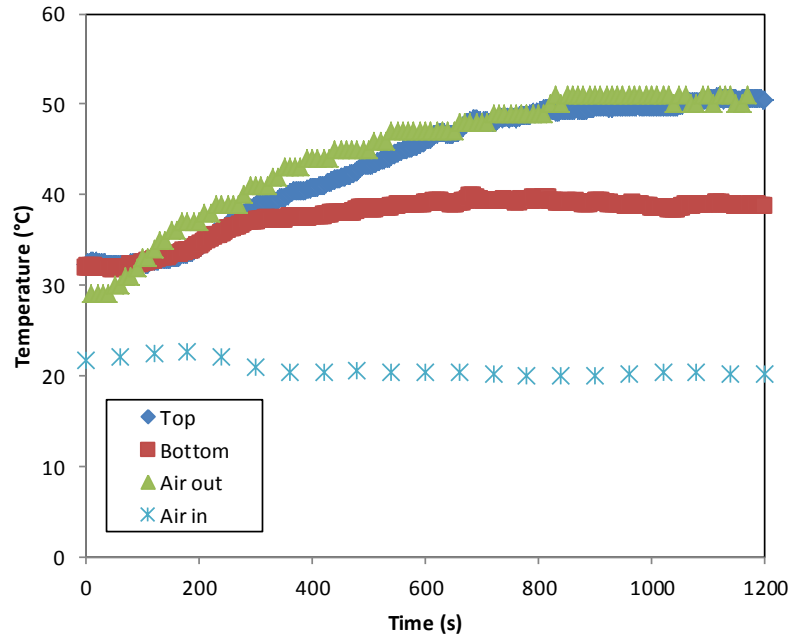
Figure 5.16 Receiver surface temperature and air temperature measurements at the inlet (bottom) and outlet (top) of the solar receiver with the blower on Speed Setting 1.
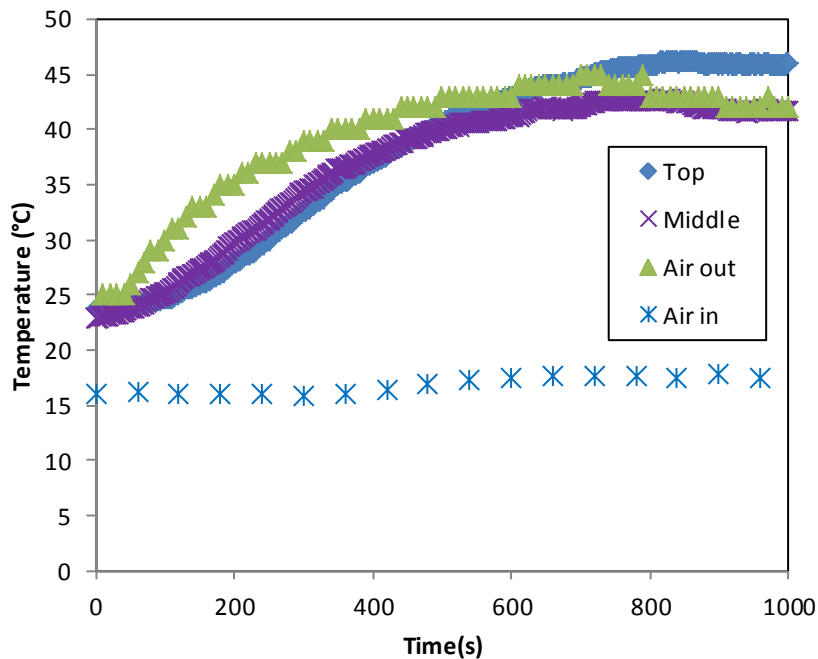
Figure 5.17 Receiver surface temperature and air temperature measurements at the inlet (bottom) and outlet (top) of the solar receiver with the blower on Speed Setting 5.

95
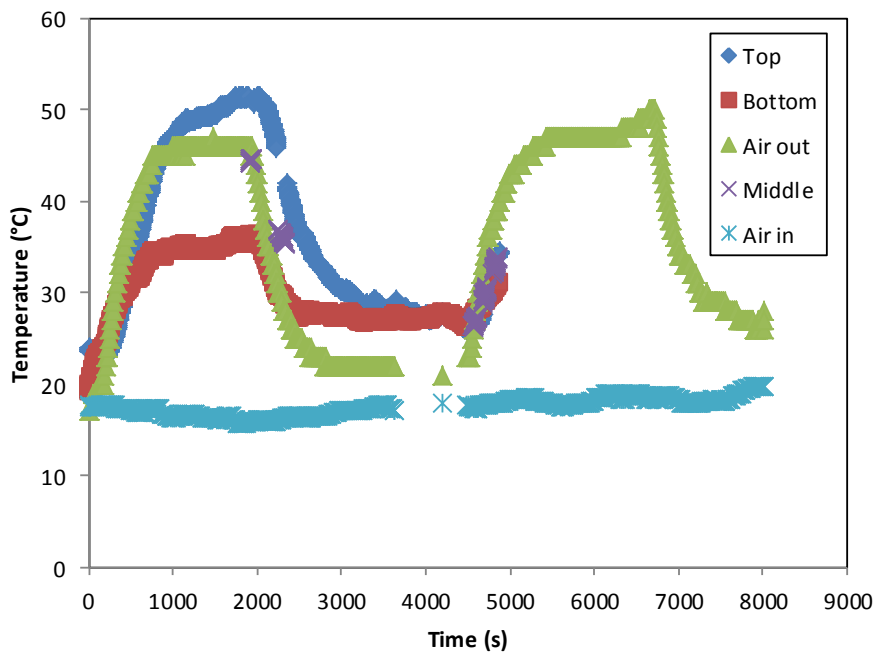
Figure 5.18 Receiver surface temperature and air temperature measurements at the inlet (bottom) and outlet (top) of the solar receiver with the blower on Speed Setting 2 and Speed Setting 4.
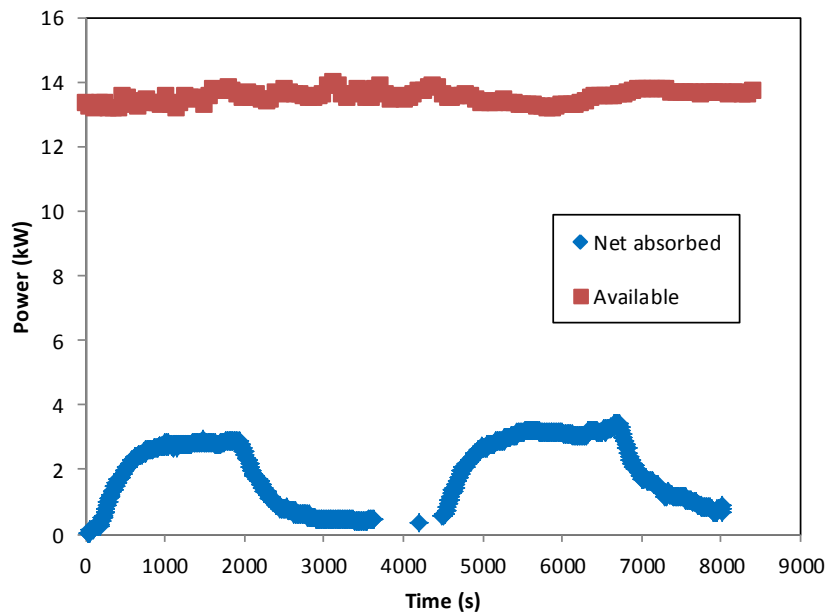
Figure 5.19 Net absorbed heat rate of the air in the solar receiver with the blower on Speed Setting 2 and Speed Setting 4.

96
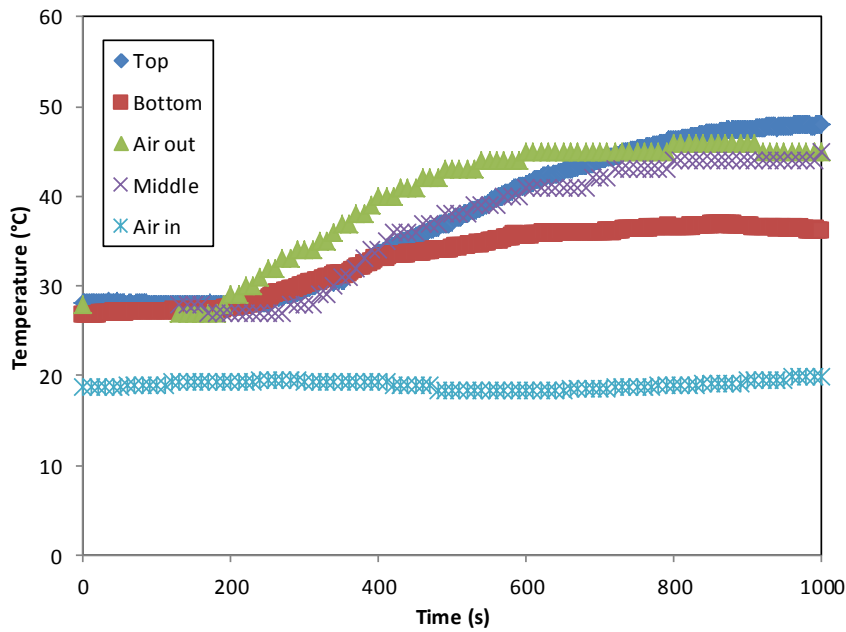
Figure 5.20 Receiver surface temperature and air temperature measurements at the inlet (bottom) and outlet (top) of the solar receiver with the blower on Speed Setting 3.

For the test with Speed Setting 3 (Day 3), the blower was switched on at 0 s, and at 200 s, the receiver was moved into the focal point. The temperature results are shown in Fig. 5.20.

5.4.1.2 Discussion

Table 5.3 shows the steady-state results for all the experiments conducted in Test A. From the results, it was found that the air temperature at the outlet was mostly higher than the receiver outlet surface temperature. The exceptions in Table 5.3 (Day 1) can be attributed to different heat flux levels on the inside walls of the cavity at different tracking positions. The thermocouple at the outlet of the receiver was placed on top of the receiver tube and was covered with insulation. This specific position on the receiver can be colder or hotter than the air at the outlet depending on the heat flux at this position. If the heat flux at the outlet of the receiver is much lower than at the inlet, the surface temperature of the receiver tube at the outlet can be lower than the air temperature, as shown in Fig. 4.16 for example. Measurement error can also play a role as discussed in Section 5.5.

The average receiver surface temperature in Test A was relatively low. The heat loss from the receiver was thus assumed negligible when compared to the heat transfer to the air blowing through the receiver at steady state. The efficiency of the collector, η_{col}, was determined

97

from these experiments as shown in Table 5.3. Since $\eta_{rec} \approx 1$, and $\eta_{refl} \approx 0.55$, the optical efficiency could be determined according to Eq. (5.4) derived from Eq. (2.7) and is shown in Table 5.3.

$$\eta_{col} = \eta_{refl}\eta_{rec}\eta_{optical} \tag{5.4}$$
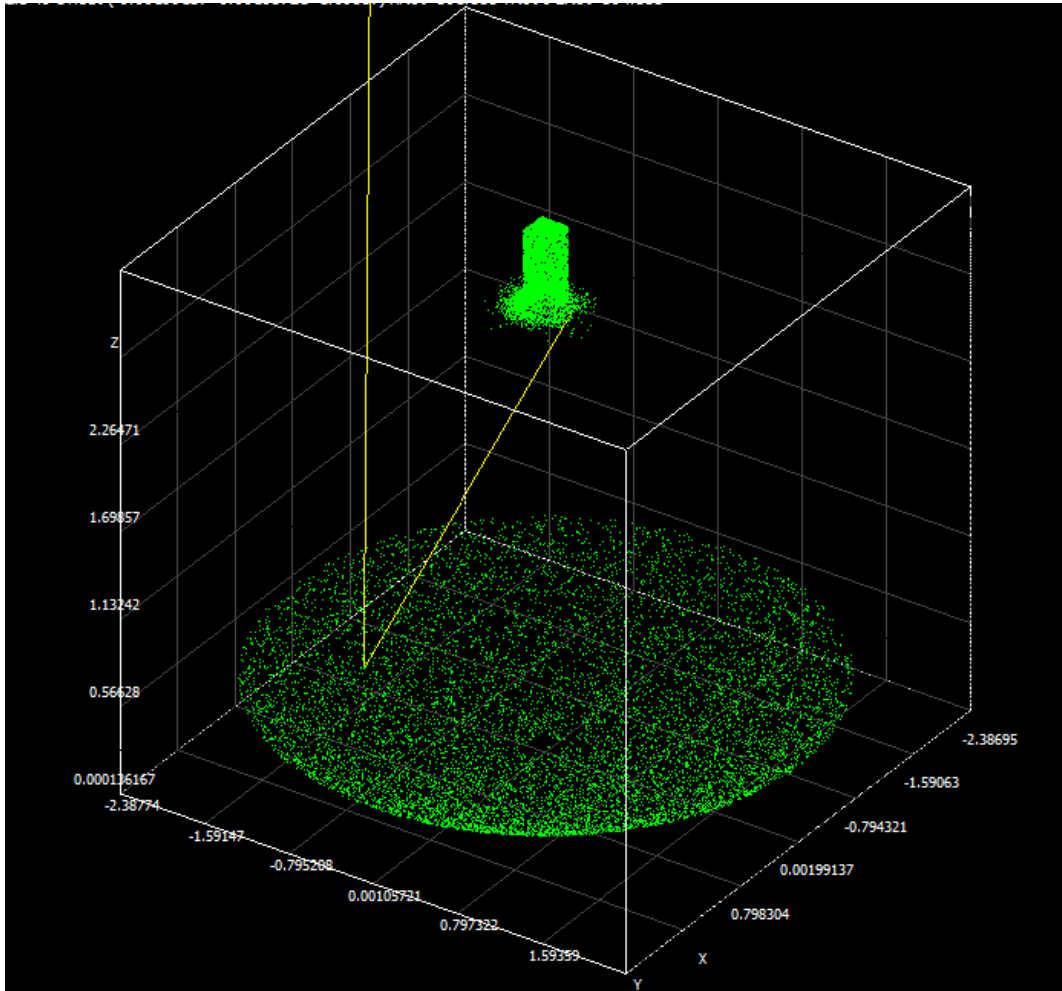
Figure 5.21 Expected ray performance of the experimental collector during the second test of Day 2, according to SolTrace.

Note that the optical efficiency fluctuated between a minimum of 36% and a maximum of 54%. These deviations in values could only be attributed to tracking error, which seemed to be a function of the solar elevation and thus a function of the time of day (See Appendix A). Note that higher efficiencies were attained when the solar elevation was higher. This can be due to the possible twisting of the structure when lifted upwards (more vertical) and thus the tracking error was higher when the sun's elevation was low, as was the case in the mornings

and afternoons. The average collector efficiency between 10:00 and 12:00 was found to be 22.1%, 26.9% between 12:00 and 13:00 and 22.3% between 14:00 and 15:00.
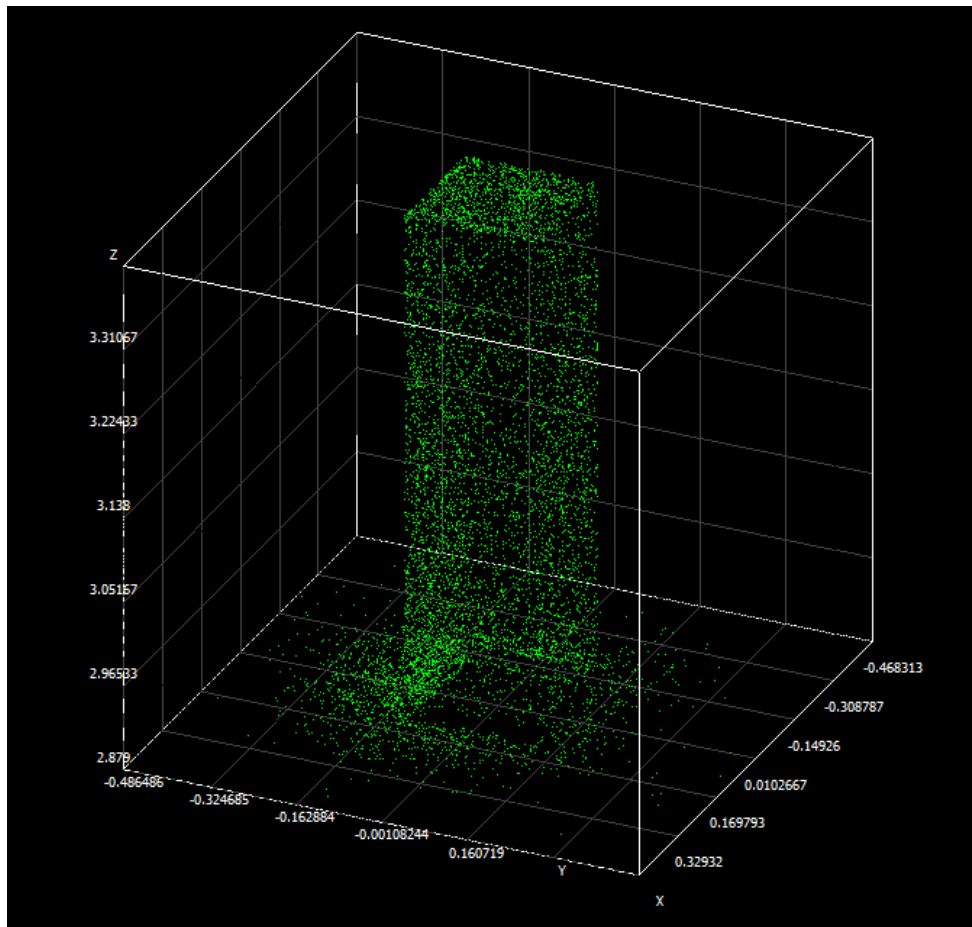
Figure 5.22 Expected solar flux available at the experimental receiver, according to SolTrace.

According to Fig. 5.5, the average slope error of the dish was expected to be 5 mrad. The maximum solar tracking error of the set-up was expected to be 1° in both axes of movement. According to the literature study, initially, the absorptivity of the stainless steel tube is 80% and the emissivity is 0.2. After exposure to high temperature, the absorptivity of the stainless steel tube is 85% and the emissivity is 0.7, according to the literature study. Thus it is assumed that the figures presented in the analytical study (Fig. 4.2) are also relevant to the experiments performed with minimal error for the receiver initially. These figures were generated with the assumption of 85% tube absorptivity. The optical error of the dish found from Fig. 4.2 for an optical efficiency of between 36% and 54% and for $A' = 0.0035$, was found to be between 20 mrad and 35 mrad. Thus, if the slope error of the dish is 5 mrad (see

99

Section 5.2.2), the specularity error of the dish, according to Eq. (3.4), is between 17.3 mrad and 33.5 mrad, which can be expected from the mill-finished aluminium sheets.

Figure 5.21 shows the expected focal spot of the experimental dish on the receiver aperture during the second test on Day 1, as found with SolTrace for a dish with 5 mrad slope error, 25 mrad specularity error, 1° tracking error, 55% dish reflectivity, DNI of 700 W/m^2 and 85% receiver tube absorptivity. According to SolTrace, such a collector would have an efficiency of 21%. This efficiency compares well with the efficiency of 23.2% (Table 5.3) obtained experimentally during the second test on Day 1 when the DNI was 700 W/m^2 (see Appendix A). Figure 5.22 shows that a fair amount of the rays would end up around the aperture instead of going into the receiver. The focal spot in the photo (Fig. 5.15) also compares well with Fig. 5.22.

5.4.1.3 Conclusion

The results showed how the receiver captured the solar power from the dish. From the results, it was found that the air temperature at the outlet was sometimes lower than the receiver outlet surface temperature and sometimes it was higher. This can be attributed to different flux levels on the inside walls of the cavity at different tracking positions. The results showed that for a small-scale open solar thermal Brayton cycle, the dish could contribute tremendously towards the total efficiency of the system. It was found that the optical efficiency of the solar dish varied between 36% and 54%. The results showed that SolTrace could be used to model the collector of the solar thermal Brayton cycle. The positioning of the receiver at the correct height and its positioning precisely in the middle of the focal point were also found to be more challenging than anticipated and it should be done with accuracy. From these experimental results, it is concluded that to make the small-scale open solar thermal Brayton cycle a success, a very accurate solar tracking system with a high-specularity, high reflectivity dish is required as was also found in the analytical work. A 1° tracking error and 10 mrad optical error with reflectivity above 90% should be sufficient. The tracking error should not be affected by factors such as wind and structure deflection and thus a smaller dish with less deflection would be more beneficial. However, it is important to note that the collector efficiency is also a function of the collector cost.

5.4.2 Test B, High-temperature test results

In this test, the dish concentrator was used to heat the receiver up to study the heat loss model of the receiver. For the high-temperature test, the temperature-dependent effects on the

100

receiver performance were investigated. For this test, the blower was removed and the inlet and outlet of the receiver were closed off with ceramic fibre insulation to prevent heat loss due to natural convection. The receiver was heated in the collector up to steady state whereafter the receiver was placed back in its resting horizontal position. This test was done to determine how the receiver loses heat to the environment. The insulation surface temperature was also measured.

5.4.2.1 Results – Part 1
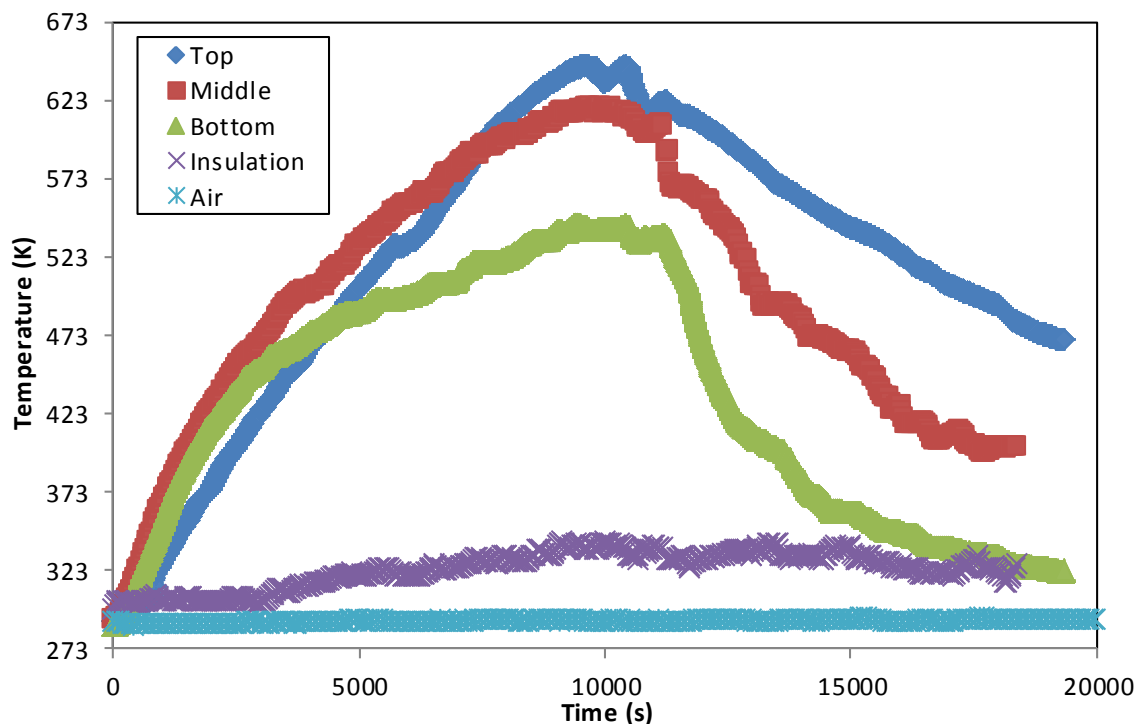
Figure 5.23 Receiver temperature increase.

Figure 5.23 shows the rise in receiver surface temperature at the top (outlet position), bottom (inlet position) and middle of the receiver when it was in the focal point of the dish. The temperature rise of the insulation is also shown. The test started at 10:22 (Day 4) and reached steady state after about 10 000 s whereafter the collector was taken back to the horizontal position. The results show that the top part of the receiver retained its temperature much longer after steady state than the middle and bottom because of hot air being trapped in the cavity. The maximum temperature reached at steady state was around 650 K. The temperature at the middle and bottom of the receiver dropped dramatically as the receiver was tilted horizontally. Figure 5.23 shows that there was a difference of about 100 °C

101

between the top and bottom of the receiver at steady state while this temperature difference was about 150 °C at the end of the test.
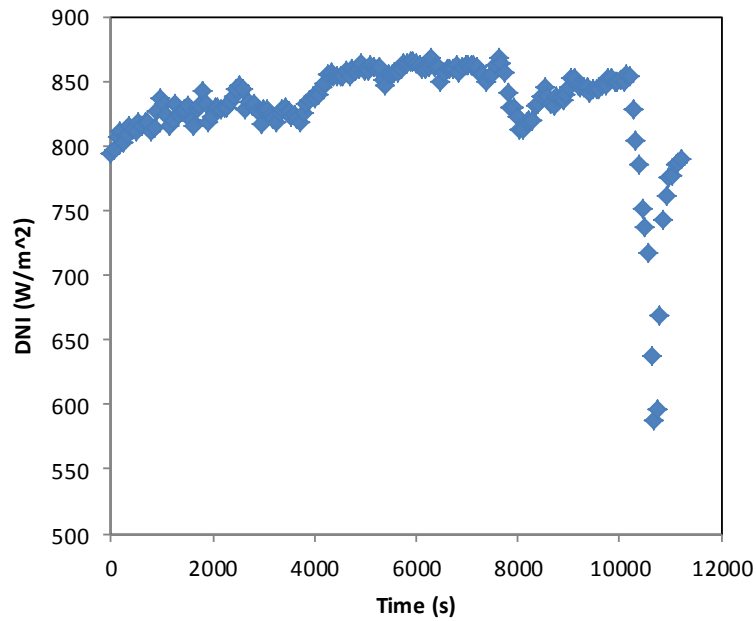
Figure 5.24 Measured DNI during the experiment (Day 4), according to the SOLYS 2.

Figure 5.25 A bottom view of the solar receiver and its support structure during receiver testing with the blue sky in the background.

In Fig. 5.24, the solar DNI as measured with the SOLYS 2 on Day 4 is shown (also see Appendix A). At around 10 000 s, the DNI went down due to a fair amount of smoke which

102

filled the air coming from a nearby wildfire. However, the receiver reached its steady-state temperature before the smoke arrived and the smoke did not affect the results. Figure 5.25 shows the receiver during the test.

5.4.2.2 Discussion – Part 1

To validate the heat loss models as described in Chapter 3, the average surface temperature of the receiver per second can be calculated analytically with Eq. (5.5) and Eq. (5.6), according to Eq. (3.9) (see Fig. 3.4).

$$T_{s,t+1} = \dot{Q}_{net,t} / mc_p + T_{s,t} \tag{5.5}$$

Where

$$\dot{Q}_{net,t} = \dot{Q}* - \dot{Q}_{loss,rad,t} - \dot{Q}_{loss,conv,t} - \dot{Q}_{loss,cond,t}$$
$$= \eta_{optical}\eta_{refl}\dot{Q}_{solar} - \varepsilon\sigma A_{ap}\left(T_{s,t}^{4} - T_0^{4}\right) - hA_{conv}\left(T_{s,t} - T_0\right) - k_{ins}A_{cond}\left(T_{s,t} - T_{ins}\right)/t \tag{5.6}$$
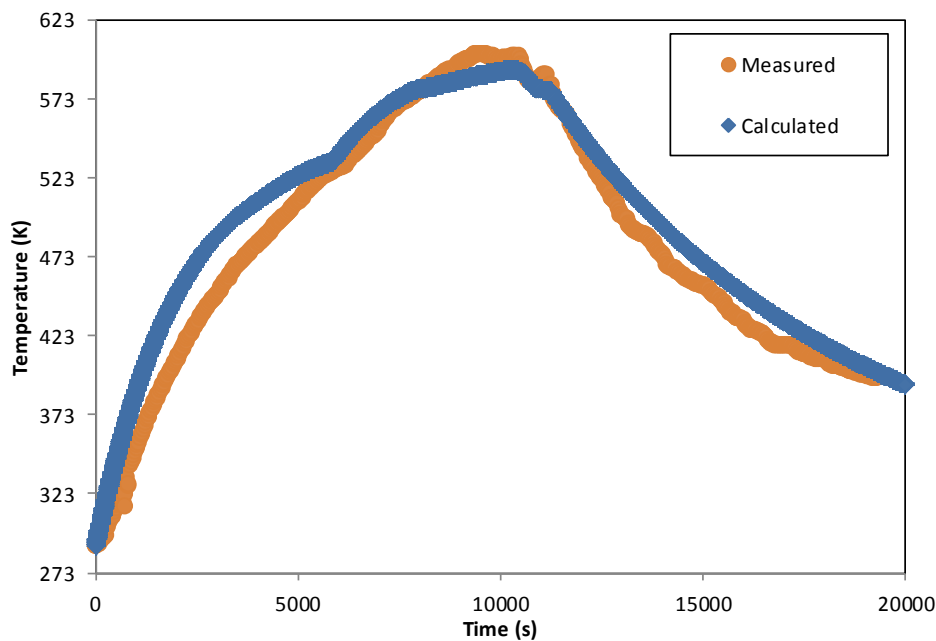
Figure 5.26 Receiver average surface temperature as a function of time as measured experimentally and as calculated with *h* = 6.5 W/ m²K before steady state and *h* = 1 W/m²K after steady state.

103

Note that to calculate the average receiver surface temperature, it was assumed that the optical efficiency of the dish was between 36% and 54% and the reflectivity of the dish was 55% as found in the experimental results in the previous section. This assumption could be made because Test B was run one day after the conclusion of Test A. Thus the efficiency of $\dot{Q}*/\dot{Q}_{solar} = \eta_{optical}\eta_{refl}$ was 22.1% between 10:00 and 12:00, and 26.9% after 12:00, according to Test A. The convection heat transfer coefficient of the cavity receiver could be determined by fitting curves to the experimental results in Fig. 5.26 and Fig. 5.27 as calculated with Eq. (5.5) and Eq. (5.6) by changing the parameter h (the convection heat transfer coefficient) until both curves fitted. The only solution where both curves fitted was for $h \approx 6.5$ W/m^{2}K and $h \approx 1$ W/m^{2}K before and after steady state respectively. Note that the receiver was placed in the horizontal position after steady state was reached. Figure 5.27 shows the conduction heat loss as calculated with the measured average receiver surface temperatures and the calculated average receiver surface temperature.
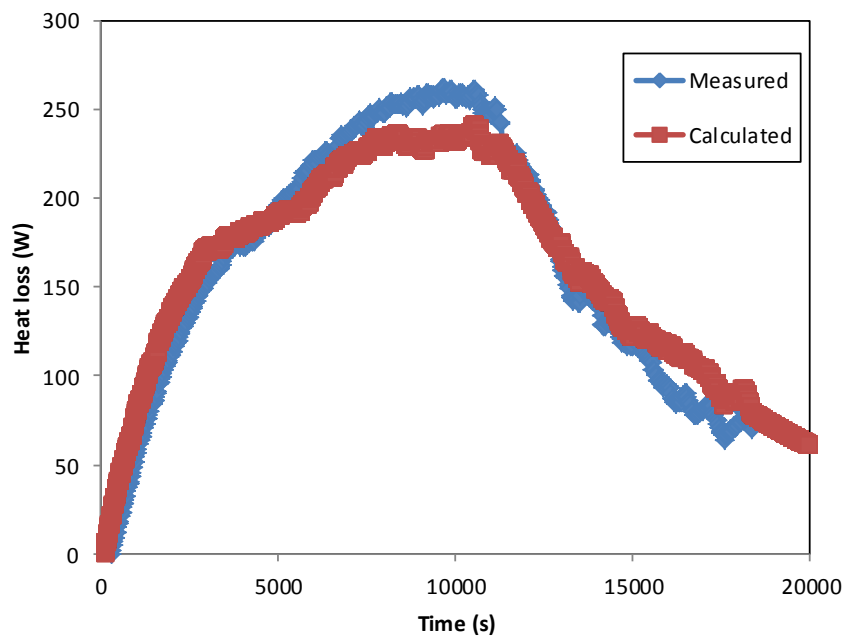
Figure 5.27 Conduction heat loss from the receiver as calculated with measured experimental data and as calculated with h = 6.5 W/ m^{2}K before steady state and h = 1 W/m^{2}K after steady state.

Also note that the following constants were used: ε was chosen as 0.7, k = 0.046 W/mK (Tiasa, 2001), $A_{cond} \approx 2$ m^2 and $A_{conv} \approx 1.675$ m^2 as these were the areas exposed to

104

conduction and convection heat loss respectively. The curve-fit result was not very sensitive to the changing of ε or k because convection heat loss dominated in this temperature range.

The heat transfer coefficient on the inside of the cavity receiver as calculated with Harris and Lenz (1985) was 3.7 W/m^{2}K (Section 3.4.2.3) for the average elevation of 36° during the test (see Appendix A). This heat transfer coefficient should still be multiplied with a wind factor. The average wind speed during the test was about 2 m/s as measured with the SOLYS 2 (see Appendix A). If the wind factor is assumed to be approximately 1.5, according to Prakash et al. (2009), the heat transfer coefficient is calculated as 5.55 W/m^{2}K.

According to Ma (1993), the forced heat transfer coefficient for the receiver due to a headwind of 2 m/s at 36°, which can be added to the natural convection heat transfer coefficient calculated as 3.7 W/m^{2}K, is calculated in Eq. (5.7).

$$h_{forced} = \left(0.1634 + 0.7498\sin(\theta) - 0.5026\sin(2\theta) + 0.3278\sin(3\theta)\right) \times V^{1.401}$$
$$= 1.15 \text{ W/m}^2\text{K} \tag{5.7}$$

According to Ma (1993), the forced heat transfer coefficient due to a side wind of 2 m/s, which can be added to the natural convection heat transfer coefficient calculated as 3.7 W/m^{2}K , is calculated in Eq. (5.8).

$$h_{forced} = 0.1967 \times V^{1.849}$$
$$= 0.7 \text{ W/m}^2\text{K} \tag{5.8}$$

The method given by Ma (1993) gives a maximum calculated convection heat transfer coefficient of 4.85 W/m^{2}K.

These calculated values of 5.55 W/m^{2}K and 4.85 W/m^{2}K show that the average convection heat transfer coefficient before steady state as determined experimentally (6.5 W/m^{2}K) is about 20% higher than determined with the heat loss model.

5.4.2.3 Results and discussion – Part 2

The convection heat transfer coefficient of the inner solar receiver cavity as determined experimentally was thus higher than that calculated with the heat loss models. After inspection of the experimental set-up, it was noted that the insulation did not cover the receiver fully and small gaps between the insulation boards were noted. These gaps appeared

due to the thermal expansion of the receiver. Also note that convection heat loss was taking place over most of the receiver tube area, since only parts of it made contact with the insulation as shown in Fig. 3.4. This was as a result of the large diameter receiver tube used and due to the 10 mm gap between the tube coil, which had to be present for welding purposes.
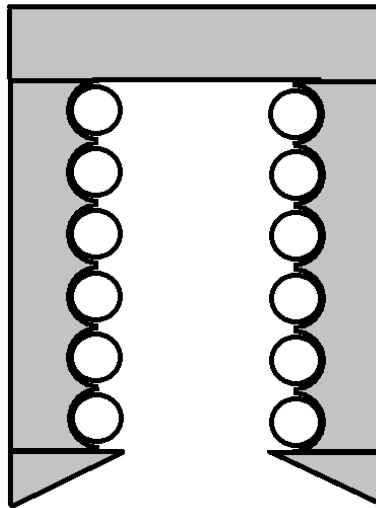
Figure 5.28 Receiver insulation covering the receiver tube so that less tube area is exposed to convection heat loss.
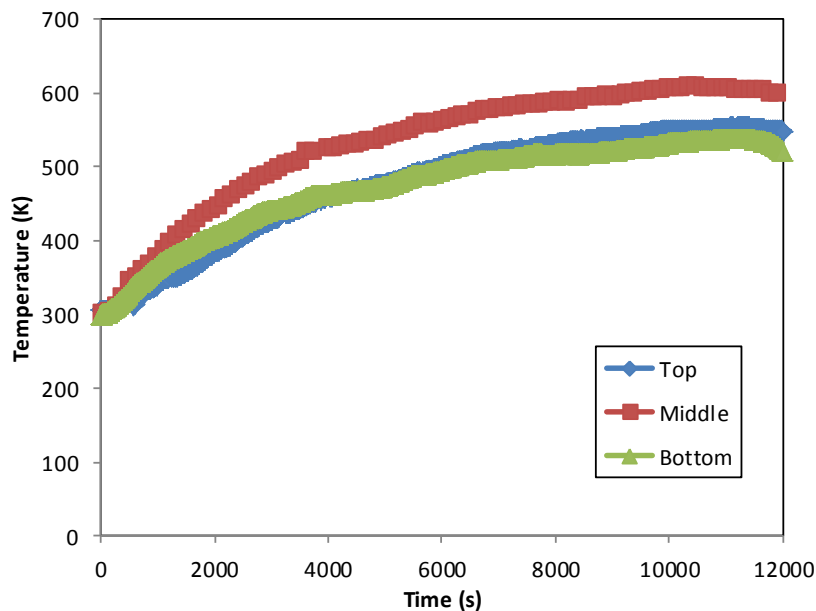
Figure 5.29 Receiver temperature rise during the second test.

The test was repeated a second time, but this time with insulation blanket stuffed in between all the gaps. The small gaps between the insulation board and the receiver tube were stuffed as shown in Fig. 5.28 (compare with Fig. 3.4) so that air could not flow around the tubes but only on the inside of the cavity.

The second test reached more or less the same average receiver surface temperature as in the first test, but with a much lower solar input. The results are shown in Fig. 5.29 and the second test is compared with the first test in Table 5.4 and Fig. 5.30. The results show that the insulation arrangement in the second test is much more efficient. Also note that in the second test, the temperature in the middle of the receiver was the higher temperature. This can be attributed to the solar heat flux distribution as shown in Fig. 4.10 and Fig. 4.11 as well as a smaller convection heat loss area in the first test.

For the insulation arrangement in the second test, the conduction heat loss was found to be more than 1.5 times more while the convection heat loss was found to be more than three times less at the same average steady-state temperature. Note that the convection heat loss rate percentage can thus be significantly reduced (Fig. 5.30) by placing the insulation around the tubes correctly and making sure that there are no gaps between the insulation and the receiver.

Table 5.4 Heat loss from the cavity receiver at steady state.

	$T_{s,ave}$ (K)	$\dot{Q}_{loss,cond}$ (W)	$\dot{Q}_{loss,conv}$ (W)	$\dot{Q}_{loss,rad}$ (W)	$\dot{Q}_{loss,total}$ (W)
Test 1	591.7	236.0	3 286	286.6	3 812
Test 2	589.1	381.5	1 003	281	1 667

The convection heat transfer coefficient of the cavity receiver in the second test was determined in a similar way as was done for the first test. It was found that $h \approx 4.5$ W/m²K before steady state and $h \approx 0.8$ W/m²K after steady state when the receiver was placed in the horizontal position. These results compare much better with the theory and thus it is concluded that the insulation arrangement should be done as was done in the second test. Note that the following constants were used for fitting the curves in the second test: ε was chosen as 0.7, $k = 0.046$ W/mK (Tiasa, 2001), $A_{cond} \approx 2.4$ m² and $A_{conv} \approx 0.838$ m² as these were the areas exposed to conduction and convection heat loss respectively. Note that the convection heat loss area is assumed to be half of what it was in the first test due to the different insulation arrangement.
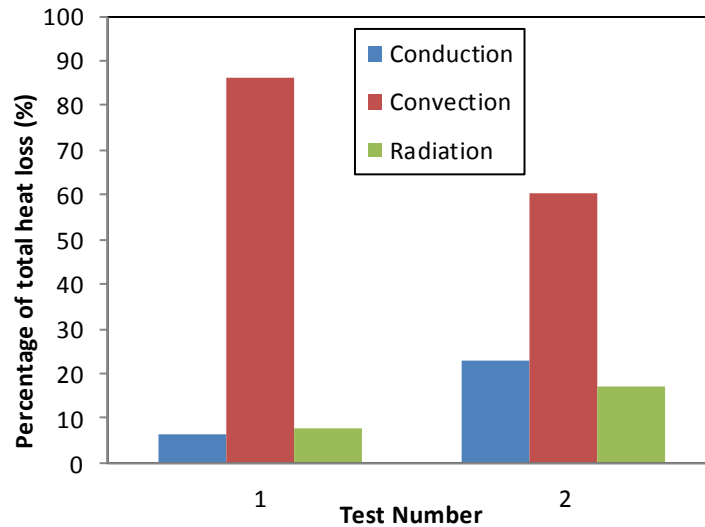
Figure 5.30 Comparison of the heat loss mechanisms from the receiver at an average temperature of 590 K as determined in two receiver tests.

5.4.2.4 Conclusion

The solar receiver was heated up to steady state in two tests with different insulation arrangements. It was found that the arrangement of the insulation around the large diameter receiver tube could significantly influence the convection and conduction heat loss rates from the cavity receiver. The receiver tube had to be covered all around on the sides to reduce heat loss. It was shown that the surface contact between the receiver insulation and the receiver tube was important. It is recommended that a single moulded insulation cover should be made for the receiver with good thermal contact between the receiver surface and the insulation. Such a cover should yield better results than with the placement of insulation boards around the receiver from different sides. However, thermal expansion might pose a problem for such a cover. The results showed that inclination played an important role in the convection heat loss of the receiver, which dominated the heat loss at the tested temperatures. The convection and conduction heat loss models were verified experimentally to a certain extent for the solar thermal Brayton cycle. However, it is recommended that the receiver should also be tested at 1 150 K.

5.5 Error analysis

The following comments are made regarding the accuracy and precision of the experimental results obtained. Note that from Eq. (5.3), the collector efficiency was determined in Test A as shown in Eq. (5.9).

$$\eta_{col} = \frac{\dot{m}c_p\left(T_{out} - T_{in}\right)}{\dot{Q}_{solar}} = \frac{\dot{m}c_p\Delta T}{\dot{Q}_{solar}} \qquad (5.9)$$

For the temperature measurements, the accuracy of the datalogger was within 0.5 °C and the accuracy of the thermocouples within 1 °C (see Section 5.4) so that the accuracy of the temperature measurement was within 1.12 °C, or $\sqrt{\left(1\right)^2 + \left(0.5\right)^2}$. According to Eq. (5.10), the accuracy of the measurement of the temperature difference was within 1.6 °C.

$$\delta\Delta T = \sqrt{\left(\delta T_{in}\right)^2 + \left(\delta T_{out}\right)^2} = \sqrt{\left(1.12\right)^2 + \left(1.12\right)^2} = 1.6 \, ^\circ\text{C} \qquad (5.10)$$

The accuracy of the air flow measurements was within 5% (Section 5.2.5) and the accuracy of the solar measurements was within 2% (Section 5.2.3). According to Eq. (5.10), the temperature difference measurements were within 5% when assuming an average temperature difference of 30 °C in Test A. The accuracy of the collector efficiency is calculated with Eq. (5.11).

$$\frac{\delta\eta_{col}}{\eta_{col}} = \sqrt{\left(\frac{\delta\dot{m}}{\dot{m}}\right)^2 + \left(\frac{\delta\Delta T}{\Delta T}\right)^2 + \left(\frac{\delta\dot{Q}_{solar}}{\dot{Q}_{solar}}\right)^2} = \sqrt{\left(0.05\right)^2 + \left(0.05\right)^2 + \left(0.02\right)^2} = 7.3\% \qquad (5.11)$$

From Table 5.3 it was found that the precision or repeatability in determining the collector efficiency was within 22%. The collector efficiency was thus determined as 0.238 ±0.052. This error was due to tracking error and misalignment of the tracking structure during different times of the day and due to the measurement error as calculated in Eq. (5.11). It is interesting to note that the precision of collector efficiency was within 12% when the first experiments of Day 1 and Day 2 were neglected (see Table 5.3).

From the collector efficiency, the optical efficiency was calculated using Eq. (5.4). Since $\eta_{rec} \approx 1$, and $\eta_{refl} \approx 0.55$, the optical efficiency was determined as 0.43 ±0.095. The optical error of the dish was between 20 mrad and 35 mrad according to Fig. 4.2 for an optical efficiency of between 36% and 54% and for $A' = 0.0035$. The optical error was used to determine the specularity error according to Eq. (3.4). The specularity error was found to be between 17.3 mrad and 33.5 mrad.

In Test B, the surface temperature of the receiver was measured at three different places. The error in temperature measurement was calculated above as 1.12 °C. At the high temperatures reached in Test B, it is assumed that the accuracy of each high-temperature measurement was within 0.5% so that the error in temperature measurement in Test B is neglected. The convection heat transfer coefficient at each time interval can be determined with Eq. (5.6). The convection heat transfer coefficient is a function of the product of the collector efficiency measurement and the solar irradiance measurement. The accuracy of the heat transfer coefficient is thus within 20% according to Eq. (5.12).

$$\frac{\delta h}{h} = \sqrt{\left(\frac{\delta \eta_{col}}{\eta_{col}}\right)^2 + \left(\frac{\delta \dot{Q}_{solar}}{\dot{Q}_{solar}}\right)^2} = \sqrt{(0.2)^2 + (0.02)^2} = 20\% \qquad (5.12)$$

The error analysis has shown that the accuracy in the measurement of the collector efficiency was within 7.3% and the accuracy in the determination of the convection heat transfer coefficient was within 20%.

5.6 Summary

An experimental set-up consisting of a two-axis solar tracker with a 4.8 m diameter dish and solar receiver with aperture area of 0.25 m x 0.25 m and tube diameter of 0.0889 m was built and tested to better understand the difficulties associated with the collector errors. The geometry-dependent and temperature-dependent factors on the performance of the receiver were investigated. The experiments conducted showed that the optimised open-cavity tubular receiver was able to absorb heat. The efficiency of the collector was determined by attaching a blower to the solar receiver so that the neat absorbed heat rate could be determined. A high-temperature test on the solar receiver was conducted to validate the conduction and convection heat loss models. The receiver was heated up to an average steady-state temperature of about 590 K whereafter it was placed back in its resting horizontal position. The solar tracking was done manually by positioning the collector in such a way that the shadow of the receiver was exactly in the middle of the dish. The solar DNI was measured with the SOLYS 2. Temperature measurements on the receiver were taken with K-type weldpad thermocouples. Results showed that SolTrace was a valid tool for ray tracing and that the heat loss models could be used to predict the performance of the solar receiver. It was shown that for the large tube diameter, the arrangement of the insulation was important and

110

that the convection heat loss could be significantly reduced by arranging the insulation correctly around the receiver tube.

111

CHAPTER 6

SUMMARY, CONCLUSION AND RECOMMENDATIONS

_____

6.1 Summary

South Africa has an advantage in terms of solar resource, but this solar resource is not used extensively due to high-cost and low-efficiency solar-to-electricity systems. The dish-mounted solar thermal Brayton cycle with recuperator offers a solution. However, heat losses and pressure losses in the cycle components can decrease the net power output of the system tremendously. In addition, the costs due to solar tracking and perfect dish optics can be high. The small-scale (1-20 kW) dish-mounted open solar thermal Brayton cycle has not been studied before. The purpose of this study was to develop the small-scale dish-mounted open solar thermal Brayton cycle by optimising the receiver and recuperator with the method of total entropy generation minimisation. Modelling methods to predict the performance and to optimise the system were developed and tested and the solar receiver was tested in an experimental set-up.

For the small-scale open solar thermal Brayton cycle, various off-the-shelf micro-turbines are available thanks to the application of micro-turbines as turbochargers in the stationary market. The small-scale open solar thermal Brayton cycle therefore has an advantage in terms of cost. A small-scale system also has a cost benefit since it can be manufactured in a production line. The small-scale aspect of the technology also makes it advantageous in terms of mobility. It can offer an off-grid electricity solution to the people of the water-scarce southern Africa. The small-scale open solar thermal Brayton cycle can also be very competitive in terms of efficiency and environmental impact.

Since the solar thermal Brayton cycle's development in the 1960s, many attempts have been made at improving the efficiency of the cycle and that of the solar receiver. A high solar receiver efficiency, however, does not necessarily mean that the receiver will perform well in an open solar thermal Brayton cycle. A holistic optimisation approach is therefore necessary. A literature study was conducted to identify the different attempts of optimisation, modelling and development of the solar thermal Brayton cycle's components. It was found that the system components are often optimised individually and not as part of a system with a common goal. In a small-scale solar thermal Brayton cycle, entropy generation mechanisms will always be present but components can be optimised for minimum entropy generation.

The method of total entropy generation minimisation allows heat transfer and fluid flow terms to be available for optimisation in a single equation, so that geometry variables of different components of an open solar thermal Brayton cycle can be optimised simultaneously.

The solar collector, consisting of the solar dish and receiver, plays a very important role in the determination of the success of the solar thermal Brayton cycle, as it acts as the heat source in the cycle. An experimental set-up of the collector of a small-scale open solar thermal Brayton cycle was built and tested to better understand the difficulties associated with the solar collector errors.

6.2 Conclusion

The method of total entropy generation minimisation was found to be a holistic optimisation approach whereby the components of the small-scale solar thermal Brayton cycle could be optimised. To maximise the net power output of the cycle, an objective function, based on the method of total entropy generation minimisation, was presented in terms of the geometry variables of an open-cavity tubular solar receiver and counterflow plate-type recuperator.

A method to determine the surface temperatures and net heat transfer rates along the length of the open-cavity receiver tube was presented. The factors contributing to the temperature and net heat transfer rate profiles on the receiver tube were divided into two components: geometry-dependent and temperature-dependent. It was found that many errors existed due to the solar collector – these were modelled with SolTrace, a ray-tracing algorithm. The Koenig and Marvin heat loss model was used to model the convection heat loss rate from an open-cavity receiver. An optimum receiver-to-concentrator-area ratio of $A' \approx 0.0035$ for 1° solar tracking error, 10 mrad optical error and 45° rim angle was found for the open-cavity tubular solar receiver. It was shown that the open-cavity tubular solar receiver surface temperature and net heat transfer rate for heating air depended on the receiver size, mass flow rate through the receiver, receiver tube diameter, receiver inlet temperature and dish errors. Receiver efficiencies of between 43% and 70% were found for the open-cavity tubular receiver with $a = 0.25$ m, $0.06\,\text{kg/s} \leq \dot{m} \leq 0.08\,\text{kg/s}$, $0.05\,\text{m} \leq d \leq 0.0833\,\text{m}$ and $900\,\text{K} \leq T_{in,0} \leq 1\,070\,\text{K}$, operating on a 4.8 m diameter dish with 10 mrad optical error and maximum solar tracking error of 1°. Results showed that the higher the mass flow rate through the receiver, the lower the surface temperatures and the more efficient the receiver became. A smaller tube diameter also allowed for higher efficiency but due to the higher pressure drop, a much lower second

113

law efficiency was obtained, which indicated that a larger tube would be more beneficial in the open solar thermal Brayton cycle. Results showed that a high receiver efficiency was not necessarily beneficial for the small-scale solar thermal Brayton cycle as a whole but that the second law efficiency was more important.

An analytical study showed that with the use of an optimised open-cavity tubular solar receiver, counterflow plate-type recuperator and a standard off-the-shelf turbomachine, the small-scale open solar thermal Brayton cycle could generate a positive net power output with solar-to-mechanical efficiencies in the range of 10-20% with much room for improvement. Results showed that for a 4.8 m diameter solar dish with 0.25 m x 0.25 m receiver aperture area, a receiver tube diameter of 0.0833 m was beneficial. For a receiver with this inner-tube diameter, a recuperator with $a = 225$ mm, $b = 2.25$ mm, $L = 1.5$ m and $n = 45$ was optimal when the recuperator mass was restricted to 500 kg and the maximum receiver surface temperature was restricted to 1 200 K. Analytical results were compared with results generated in Flownex, an integrated systems CFD code. The results showed that for the calculation of the steady-state temperatures and pressures, there was good comparison between the Matlab results and Flownex results (within 8%), except for the recuperator outlet temperature, which differed because of the use of different ε-NTU methods to calculate the recuperator efficiency.

For the experimental study, a 4.8 m parabolic aluminium dish with rim angle of 45° and two-axis tracking system was designed and built. A tubular stainless steel solar cavity receiver with outer-tube diameter of 0.0889 m and with ceramic fibre insulation was built and tested experimentally to determine whether it would be capable of delivering heat to the small-scale open solar thermal Brayton cycle. Weldpads with K-type thermocouples were welded onto the receiver to measure the surface temperatures at the inlet, middle and outlet of the receiver. The efficiency of the collector was determined by attaching a blower to the solar receiver so that the neat absorbed heat rate could be determined. A high-temperature test on the solar receiver was performed so that the conduction and convection heat loss models could be validated. The effects of mass flow rate, receiver tube air inlet temperature and tube diameter on the efficiency of the receiver were shown. The higher the inlet temperature, the less efficient the receiver became and the higher the maximum receiver surface temperature. Experimental results were compared with analytical calculations. The use of SolTrace and the heat loss models were validated to a certain extent. The convection heat transfer coefficient of the cavity receiver was determined experimentally and analytically. Results showed that SolTrace was a valid tool for ray tracing and that the heat loss models could predict the

performance of the solar receiver. Experimental results showed that the heat loss rate from the solar cavity receiver due to convection and conduction was significantly reduced with the proper insulation arrangement.

6.3 Recommendations

From the experimental results, it was concluded that to make the small-scale open solar thermal Brayton cycle a success, a very precise solar tracking system, with a high-specularity, high-reflectivity dish is required, as was also found in the analytical work. A 1° tracking error and 10 mrad optical error with reflectivity above 90% should be sufficient. An open-cavity tubular solar receiver and a counterflow plate-type recuperator were identified as cost-effective solutions for the open solar thermal Brayton cycle. It is recommended that for a 4.8 m dish diameter, a 0.0833 m receiver tube diameter be used. It is suggested that for future work, a smaller but more accurate and efficient dish and tracking system be used for an experimental study, since the larger the dish, the larger the errors due to deflections and wind loadings. The proposed technology can hold endless opportunity for the people of southern Africa as an efficient and cost-effective power solution, especially if the solar collector is small and efficient.

Due to the difficult welds during the manufacturing of the receiver, a 10 mm gap was needed between the receiver tube coils. The relatively large receiver tube diameter also caused air gaps between the receiver tube and the insulation. For these reasons, it is recommended that a moulded receiver cover be used to insulate the receiver so that air cannot flow around the receiver tubes but only on the inner side of the receiver cavity. Furthermore, good thermal contact between the insulation and the receiver should be achieved regardless of thermal expansion. It is also recommended that thermal expansion of the open-cavity tubular receiver be considered when coupling the receiver to the open solar thermal Brayton cycle.

Further research should consider the testing of the optimised open-cavity tubular receiver at a temperature of 1 150 K for fatigue loadings and thermal expansion. The optimised receiver should be coupled to an optimised recuperator and micro-turbine to determine the net power output of the system experimentally. A cost-effective high-temperature and low-emissivity stainless steel receiver coating would be very beneficial for the cycle and it is recommended that such a coating be developed. Further research can also investigate the optimisation of the cycle at receiver surface temperatures below 700 °C so that black chromium can be used as low-emissivity coating.

It is concluded that the small-scale dish-mounted open solar thermal Brayton cycle with tubular receiver and recuperator does have merit and it is recommended that it be investigated further experimentally.

REFERENCES

_____

Allen, K.G., 2010. Performance characteristics of packed bed thermal energy storage for solar thermal power plants. Faculty of Engineering. University of Stellenbosch, Department of Mechanical and Mechatronic Engineering.

Al-Naima, F.M., Yaghobian, N.A., 1990. Design and construction of a solar tracking system. *Solar & Wind Technology*, Vol. 7(5), pp. 611-617.

Ambrosini, A., Lambert, T.N., Staiger, C.L., Hall, A.C., Bencomo, M., Stechel, E.B., 2010. Improved high temperature solar absorbers for use in concentrating solar power central receiver applications. Sandia Laboratory Report SAND2010-7080.

Amsbeck, L., Buck, R., Heller, P., Jedamski, J., Uhlig, R., 2008. Development of a tube receiver for a solar-hybrid microturbine system. In: Proceedings of the 14th Biennial CSP SolarPaces Symposium, Las Vegas, USA.

Amsbeck, L., Denk, T., Ebert, M., Gertig, C., Heller, P., Herrmann, P., Jedamski, J., John, J., Pitz-Paal, R., Prosinečki, T., Rehn, J., Reinalter, W., Uhlig, R., 2010. Test of a solar-hybrid microturbine system and evaluation of storage deployment. In: Proceedings of the SolarPaces International Symposium of Solar Thermal, September, Perpignan, France.

Argeseanu, A., Ritchie, E., Leban, K., 2009. A new solar position sensor using low cost photosensors matrix for tracking systems. *WSEAS Transactions on Power Systems* 6, Vol. 4, pp. 189-198.

Ávila-Marín, A.L., 2011. Volumetric receivers in solar thermal power plants with central receiver system technology: A review. *Solar Energy*, Vol. 85, pp. 891-910.

BASF, The Chemical Company, 2007. Pigment for solar heat management in paints. Available at: www.basf.com/pigment. [Last accessed on 2013/10/07].

Batteh, J.J., Newman, C.E., 2008. Detailed simulation of turbocharged engines with modelica. *The Modelica Association, March 3-4.*

Bejan, A., Kearney, D.W., Kreith, F., 1981. Second law analysis and synthesis of solar collector systems. *Journal of Solar Energy Engineering*, Vol. 103, pp. 23-28.

Bejan, A., 1982a. Entropy generation through heat and fluid flow. Colorado: John Wiley & Sons, Inc.

Bejan, A. 1982b. Extraction of exergy from solar collectors under time-varying conditions. *International Journal of Heat and Fluid Flow*, Vol. 3(2), pp. 67-72.

Bejan, A., 1988. Theory of heat transfer-irreversible power plants. *International Journal of Heat and Mass Transfer*, Vol. 31(6), pp. 1211-1219.

Bejan, A., 1996a. Entropy Generation Minimization. Boca Raton, Florida: CRC Press.

Bejan, A., 1996b. Method of entropy generation minimization, or modelling and optimization based on combined heat transfer and thermodynamics. *Revue Générale de Thermique*, Vol. 35, pp. 637-646.

Bejan, A., 1996c. The equivalence of maximum power and minimum entropy generation rate in the optimization of power plants. *Journal of Energy Resources Technology,* Vol. 118(2), pp. 98-101.

Bejan, A., Tsatsaronis, G., Moran, M., 1996. Thermal design and optimization. New York: John Wiley & Sons, Inc.

Bejan, A., 1997. Advanced engineering thermodynamics, 2nd ed. Durham: John Wiley & Sons, Inc.

118

Bejan, A., 2002. Fundamentals of exergy analysis, entropy generation minimization, and the generation of flow architecture. *International Journal of Energy Research*, Vol. 26, pp. 545-565, DOI: 10.1002/er.804.

Bertocchi, R., Karni, J., Kribus, A., 2004. Experimental evaluation of a non-isothermal high temperature solar particle receiver. *Energy*, Vol. 29, pp. 687-700.

Bode, S.J., Gauché, P., 2012. Review of optical software for use in concentrated solar power systems. In: Proceedings of the 1st Southern African Solar Energy Conference (SASEC 2012), 21-23 May, Stellenbosch, South Africa.

Bogaard, R.H., Desai, P.D., Li, H.H., Ho, C.Y., 1993. Thermophysical properties of stainless steels. *Thermochimica Acta*, Vol. 218, pp. 373-393.

Bogaerts, W.F., Lampert, C.M., 1983. Review materials for photothermal solar energy conversion. *Journal of Materials Science*, Vol. 18, pp. 2847-2875.

Brooks, M.J., 2005. Performance of a parabolic trough solar collector. Dissertation: University of Stellenbosch, South Africa.

Buck, R., Bräuning, T., Denk, T., Pfänder, M., Schwarzbözl, P., Tellez, F., 2002. Solar-hybrid gas turbine-based power tower systems (REFOS). *Journal of Solar Energy Engineering*, Vol. 124, pp. 1-9.

Burrow, B.V., 1969. The effect of recuperator geometry on a regenerated Brayton cycle. Dissertation: United States Naval Postgraduate School, Monterey.

Cameron, H.M., Mueller, L.A., Namkoong, D., 1972. Preliminary design of a solar heat receiver for a Brayton-cycle space power system. Report NASA TM X-2552, National Aeronautics and Space Administration, Lewis Research Center.

Cao, G., Weber, S.J., Martin, S.O., Sridharan, K., Anderson, M.H., Allen, T.R., 2013. Spectral emissivity of candidate alloys for very high temperature reactors in high temperature air environment. *Journal of Nuclear Materials*, Vol. 441, pp. 667-673.

Capobianco, M., Marelli, S., 2011. Experimental analysis of unsteady flow performance in an automotive turbocharger turbine fitted with a waste-gate valve. In: Proceedings of the IMechE, Part D: Journal of Automobile Engineering, Vol. 225.

Çengel, Y.A., 2006. Heat and mass transfer. 3rd ed. McGraw-Hill: Nevada.

Chen, L., Sun, F., Wu, C., Kiang, R.L., 1997. Theoretical analysis of the performance of a regenerative closed Brayton cycle with internal irreversibilities. *Energy Conversion and Management*, Vol. 38(9), pp. 871-877.

Chen, L., Zhang, W., Sun, F., 2007. Power, efficiency, entropy-generation rate and ecological optimization for a class of generalized irreversible universal heat-engine cycles. *Applied Energy*, Vol. 84, pp. 512-525.

Cheng, C., Chen, C., 2000. Maximum power of an endoreversible intercooled Brayton cycle. *International Journal* of *Energy Research*, Vol. 24, pp. 485-494.

Chong, K.K., Wong, C.W., 2009, General formula for on-axis sun-tracking system and its application in improving tracking accuracy of solar collector. *Solar Energy*, Vol. 83, pp. 298-305.

Churchill, S.W., Chu, H.H.S., 1975. Correlating equations for laminar and turbulent free convection from a vertical plate. *International Journal of Heat and Mass Transfer*, Vol. 18, pp. 1323.

Clausing, A.M., 1981. An analysis of convective losses from cavity solar central receivers. *Solar Energy*, Vol. 27(4), pp. 295-300.

Colebrook, C.F., 1939. Turbulent flow in pipes, with particular reference to the transition between the smooth and rough pipe laws. *Journal of the Institute of Civil Engineers London*, Vol. 11, pp. 133-156.

Cui, F., He, Y., Cheng, Z., Li, Y., 2013. Study on combined heat loss of a dish receiver with quartz glass cover. *Applied Energy*, Vol. 112, pp. 690-696.

Cui, H., Hou, X., Yuan, X., 2003. Energy analysis of space solar dynamic heat receivers. *Solar Energy*, Vol. 74, pp. 303-308.

Dickey, B., 2011. Test results from a concentrated solar microturbine Brayton cycle integration. In: Proceedings of ASME TurboExpo, GT2011, June 6-10, Vancouver, British Columbia, Canada.

Dixon, S.L., 2005. Fluid Mechanics and Thermodynamics of Turbomachinery, 5th ed. Liverpool: Elsevier Butterworth-Heinemann.

DoE (Department of Energy, South Africa), 2014. Coal resources. Available at: http://www.energy.gov.za/files/coal_frame.html. [Last accessed on 2014/10/30].

Farahat, S., Sarhaddi, F., Ajam, H., 2009. Exergetic optimization of flat plate solar collectors. *Renewable Energy*, Vol. 34, pp. 1169-1174.

Fluri, T.P., 2009. The potential of concentrating solar power in South Africa. *Energy Policy*, Vol. 37, pp. 5075-5080.

Fork, D.K., Fitch, J., Ziaei, S., Jetter, R.I., 2012. Life estimation of pressurized-air solar-thermal receiver tubes. *Journal of Solar Energy Engineering*, Vol. 134(4), pp. 041016-1-11.

Frei, S.A., 2004. Performance and driveability optimization of turbocharged engine systems. Dissertation: Swiss Federal Institute of Technology, Zurich.

Gandhidasan, P., 1993. Thermodynamic analysis of a closed-cycle solar gas-turbine plant. *Energy Conversion and Management*, Vol. 34(8), pp. 657-661.

Garcia, R.F., Formoso, R.B., Catoira, A.D., Gomez, J.R., 2012. Pressurized concentrated solar power receiver designed to operate with closed Brayton cycles. In: Proceedings of the

International Conference on Renewable Energies and Power Quality (ICREPQ'12), Santiago de Compostela, Spain.

Garrett, 2014. Garrett by Honeywell: Turbochargers, Intercoolers, Upgrades, Wastegates, Blow-Off Valves, Turbo-Tutorials. Available at: http://www.TurboByGarrett.com. [Last accessed on 2014/08/22].

Gee, R., Brost, R., Zhu, G., Jorgensen, G., 2010. An improved method for characterizing reflector specularity for parabolic trough concentrators. In: Proceedings of SolarPaces, 21-24 September 2010, Perpignon, France, Paper 0284.

GeoModel Solar, 2014. Direct normal irradiation. Available at: http://solargis.info/doc/free-solar-radiation-maps-DNI. [Last accessed on 2014/08/22].

Geuder, N., Janotte, N., Wilbert, S., 2009. Precise measurements of solar beam irradiance through improved sensor calibration. In: Proceedings of SolarPaces, 15-18 September 2009, Berlin, Germany.

Gomez, A., Azzaro-Pantel, C., Domenech, S., Pibouleau, L., Latgé, C., Haubensack, D., Dumaz, P., 2010. Exergy analysis for Generation IV nuclear plant optimization. *International Journal of Energy Research*, Vol. 34, pp. 609-625, DOI: 10.1002/er.1575.

Grossman, J.W., Houser, R.M., Erdman, W.W., 1991. Prototype dish testing and analysis at Sandia National Laboratories. Sandia Laboratory Report SAND91-1283C.

Guzzella, L., Onder, C.H., 2010. Introduction to Modeling and Control of Internal Combustion Engine Systems, 2nd ed. Berlin, Germany: Springer-Verlag. DOI 10.1007/978-3-642-10775-7.

Harris, J.A., Lenz, T.G., 1985. Thermal performance of solar concentrator/cavity receiver systems. *Solar Energy*, Vol. 34(2), pp. 135-142.

Haugwitz, S., 2002. Modelling of Microturbine Systems. Dissertation: Department of Automatic Control, Lund Institute of Technology, ISSN 0280-5316, ISRN LUTFD2/TFRT- -5687-SE.

Heller, P., Pfänder, M., Denk, T., Tellez, F., Valverde, A., Fernandez, J., Ring, A., 2006. Test and evaluation of a solar powered gas turbine system. *Solar Energy*, Vol. 80, pp. 1225-1230.

Helwa, N.H., Bahgat, A.B.G., El Shafee, A.M.R, El Shenawy, E.T., 2000. Maximum collectable solar energy by different solar tracking systems. *Energy Sources*, Vol. 22(1), pp. 23-34.

Hepbasli, A., 2008. A key review on exergetic analysis and assessment of renewable energy resources for a sustainable future. *Renewable and Sustainable Energy Reviews*, Vol. 12, pp. 593-661.

Hesselgreaves, J.E., 2000. Rationalisation of second law analysis of heat exchangers. *International Journal of Heat and Mass Transfer*, Vol. 43(22), pp. 4189-4204.

Hischier, I., Hess, D., Lipiński, W., Modest, M., Steinfeld, A., 2009. Heat transfer analysis of a novel pressurized air receiver for concentrated solar power via combined cycles. *Journal of Thermal Science and Engineering Applications*, Vol. 1, pp. 041002-1-6.

Ho, C.K., 2008. Software and codes for analysis of concentrating solar power technologies. Sandia Laboratory Report: SAND2008-8053.

Ho, C.K., Iverson, B.D., 2014. Review of high-temperature central receiver designs for concentrating solar power. *Renewable and Sustainable Energy Reviews*, Vol. 29, pp. 835-846.

Holmberg, H., Ruohonen, P., Ahtila, P., 2009. Determination of the real loss of power for a condensing and a backpressure turbine by means of second law analysis. *Entropy*, Vol. 11, pp. 702-712; doi:10.3390/e11040702.

Hu, Y., Schaefer, L.A., Hartkopf, V., 2011. Detailed energy and exergy analysis for a solar lithium bromide absorption chiller and a conventional electric chiller (R134a). In: Proceedings of the ASME 2011 International Mechanical Engineering Congress & Exposition (IMECE 2011-64266).

Hunt, A.J., 1979. A new solar thermal receiver utilizing a small particle heat exchanger. In: Proceedings of the 13th Intersociety Energy Conversion Engineering Conference, August, Boston, MA.

Hutchins, M.G., 1979. Spectrally selective solar absorber coatings. *Applied Energy*, Vol. 5(4), pp. 251-262.

Izquierdo Millan, M., Hernandez, F. and Martin, E., 1996. Available solar exergy in an absorption cooling process. *Solar Energy*, Vol. 56(6), pp. 505-511.

Janecek, M., Moses, W.M., 2008. Optical reflectance measurements for commonly used reflectors. *IEEE Transactions on Nuclear Science*, Vol. 55(4), pp. 2432-7.

Jilte, R.D., Kedare, S.B., Nayak, J.K., 2013. Natural convection and radiation heat loss from open cavities of different shapes and sizes used with dish concentrator. *Mechanical Engineering Research*, Vol. 3(1), pp. 25-43.

Johnson, G., 2009. Plugging into the sun. *National Geographic*, Vol. 216(3), pp. 28-53.

Jones, P.D., Nisipeanu, E., 1996. Spectral-directional emittance of thermally oxidized 316 stainless steel. *International Journal of Thermophysics*, Vol. 17(4), pp. 967-978.

Jubeh, N.M., 2005. Exergy analysis and second law efficiency of a regenerative Brayton cycle with isothermal heat addition. *Entropy*, Vol. 7(3), pp. 172-187.

Jung, M., Ford, R.G., Glover, K., Collings, N., Christen, U., Watts, M.J., 2002. Parameterization and transient validation of a variable geometry turbocharger for mean-value modeling at low and medium speed-load points. *Society of Automotive Engineers, Inc. 2002-01-2729*.

Kalogirou, S.A., 2003. Entropy generation minimization of imaging concentrating solar collectors. In: Proceedings of ISES 2003 Solar World Congress, Goteborg, Sweden.

Kalogirou, S.A., 2004. Solar thermal collectors and applications. *Progress in Energy and Combustion Science*, Vol. 30, pp. 231-295.

Karni, J., Kribus, A., Doron, P., Rubin, R., Filterman, A., Sagie, D., 1997. The DIAPR: A high-pressure high-temparture solar receiver. *Journal of Solar Energy Engineering*, Vol. 119, pp. 74-78.

Karni, J., Kribus, A., Rubin, R., Doron, P., 1998. The "Porcupine": A novel high-flux absorber for volumetric solar receivers. *Journal of Solar Energy Engineering*, Vol. 120, pp. 85-95.

Karsli, S., 2007. Performance analysis of new-design solar air collectors for drying applications. *Renewable Energy*, Vol. 32, pp. 1645-1660.

Kaushik, S.C., Tyagi, S.K, 2002. Finite time thermodynamic analysis of an irreversible regenerative closed cycle Brayton heat engine. *International Journal of Solar Energy*, Vol. 22(3-4), pp. 141-151.

Keenan, J.H., 1951. Availability and irreversibility in thermodynamics. *British Journal of Applied Physics*, Vol. 2, pp. 183-192.

Kim, K., Siegel, N., Kolb, G., Rangaswamy, V., Moujaes, S.F., 2009. A study of solid particle flow characterization in solar particle receiver. *Solar Energy*, Vol. 83, pp. 1784-1793.

Kobayashi, M., Ono, A., Otsuki, M., Sakate, H., Sakum, F., 1999. A database of normal spectral emissivities of metals at high temperatures. *International Journal of Thermophysics*, Vol. 20(1), pp. 299-308.

Kreith, F., Kreider, J.F., 1978. Principles of solar engineering. Colorado: Hemisphere.

Kretzsmar, H., Gauché, P., 2012. Hybrid pressurised air receiver for the sunspot cycle. In: Proceedings of the 1st Southern African Solar Energy Conference (SASEC 2012), 21-23 May, Stellenbosch, South Africa.

Kribus, A., Doron, P., Rubin, R., Karni, J., Reuven, R., Duchan, S., Taragan, E., 1999. A multistage solar receiver: the route to high temperature. *Solar Energy*, Vol. 67(1–3), pp. 3-11.

Lampert, C.M., 1979. Coatings for enhanced photothermal energy collection. *Solar Energy Materials*, Vol. 1, pp. 319-341.

Lampinen, M.J., Wikstén, R., 2006. Theory of effective heat-absorbing and heat-emitting temperatures in entropy and exergy analysis with applications to flow systems and combustion processes. *Journal of Non-Equilibrium Thermodynamics*, Vol. 31(3), pp. 257-291, DOI 10.1515/JNETDY.2006.012.

Le Roux, W.G., Bello-Ochende, T., Meyer, J.P., 2011. Operating conditions of an open and direct solar thermal Brayton cycle with optimised cavity receiver and recuperator. *Energy*, Vol. 36, pp. 6027-6036.

Le Roux, W.G., Bello-Ochende, T., Meyer, J.P., 2012a. Optimum performance of the small-scale open and direct solar thermal Brayton cycle at various environmental conditions and constraints. *Energy*, Vol. 46, pp. 42-50.

Le Roux, W.G., Bello-Ochende, T., Meyer, J.P., 2012b. Thermodynamic optimisation of the integrated design of a small-scale solar thermal Brayton cycle. *International Journal of Energy Research*, Vol. 36, pp. 1088-1104.

Le Roux, W.G., Bello-Ochende, T., Meyer, J.P., 2012c. Optimum small-scale open and direct solar thermal Brayton cycle for Pretoria, South Africa. In: Proceedings of the ASME, 6th International Conference on Energy Sustainability (ES 2012-91135), 23-26 July, San Diego, CA, USA.

Le Roux, W.G., Bello-Ochende, T., Meyer, J.P., 2012d. Optimum small-scale open and direct solar thermal Brayton cycle for Pretoria, South Africa. In: Proceedings of the 1st Southern African Solar Energy Conference (SASEC 2012), 21-23 May, Stellenbosch, South Africa.

Le Roux, W.G., Bello-Ochende, T., Meyer, J.P., 2013. A review on the thermodynamic optimisation and modelling of the solar thermal Brayton cycle. *Renewable and Sustainable Energy Reviews*, Vol. 28, pp. 677-690.

Le Roux, W.G., Mwesigye, A., Bello-Ochende, T., Meyer, J.P., 2014a. Tracker and collector for an experimental setup of a small-scale solar thermal Brayton cycle. In: Proceedings of the 2nd Southern African Solar Energy Conference (SASEC 2014), 27-29 January, Port Elizabeth, South Africa.

Le Roux, W.G., Bello-Ochende, T., Meyer, J.P., 2014b. The efficiency of an open-cavity solar receiver for a small-scale solar thermal Brayton cycle. *Energy Conversion and Management*, Vol. 84, pp. 457-470.

Le Roux, W.G., Bello-Ochende, T., Meyer, J.P., 2014c. Optimisation of an open rectangular cavity receiver and recuperator used in a small-scale solar thermal Brayton cycle with thermal losses. In: Proceedings of the 10th International Conference on Heat Transfer, Fluid Mechanics and Thermodynamics (HEFAT2014), 14-16 July, Orlando, Florida.

Lerou, P.P.P.M., Veenstra, T.T., Burger, J.F., Ter Brake, H.J.M., Rogalla, H., 2005. Optimization of counterflow heat exchanger geometry through minimization of entropy generation. *Cryogenics*, Vol. 45, pp. 659-669.

Li, Y., He, Y., Wang, Z., Xu, C., Wang, W., 2012. Exergy analysis of two phase change materials storage system for solar thermal power with finite-time thermodynamics. *Renewable Energy*, Vol. 39, pp. 447-454.

Lidsky, L.M., Lanning, D.D., Staudt, J.E., Yan, X.L., Kaburaki, H., Mori, M., et al., 1991. A direct-cycle gas turbine power plant for near-term application: MGR-GT. *Energy*, Vol. 16, pp. 177-186.

Lloyd, J.R., Sparrows, E.M., 1970. Combined force and free convection flow on vertical surfaces. *International Journal of Heat and Mass Transfer*, Vol. 13.

Ma, R.Y., 1993. Wind effects on convective heat loss from a cavity receiver for a parabolic concentrating solar collector. Sandia Laboratory Report SAND92-7293.

Mandich, N.V., Snyder, D.L., 2010. Modern electroplating. Chapter 7. 5th ed. New York: John Wiley & Sons, Inc.

McDonald, C.G., 1995. Heat loss from an open cavity. Sandia Laboratory Report SAND95-2939.

McDonald, C.F., 2000. Low-cost compact primary surface recuperator concept for microturbines. *Applied Thermal Engineering*, Vol. 20, pp. 471-497.

McDonald, C.F., Rodgers, C., 2002. The ubiquitous personal turbine - a power vision for the 21st century. *Journal of Engineering for Gas Turbines and Power*, Vol. 124, pp. 835-844.

McDonald, C.F., 2003. Recuperator considerations for future higher efficiency microturbines. *Applied Thermal Engineering*, Vol. 23, pp. 1463-1487.

McDonald, C.F., Rodgers, C., 2008. Small recuperated ceramic microturbine demonstrator concept. *Applied Thermal Engineering*, Vol. 28, pp. 60-74.

Miller, F., Koenigsdorff, R., 1991. Theoretical analysis of a high-temperature small-particle solar receiver. *Solar Energy Materials*, Vol. 24, pp. 210-221.

Mills, D., 2004. Advances in solar thermal electricity technology. *Solar Energy*, Vol. 76, pp. 9-31.

Moraal, P., Kolmanovsky, I., 1999. Turbocharger modeling for automotive control applications. In: Proceedings of the International Congress and Exposition, Detroit, Michigan. March 1-4.

Moynihan, P.I., 1983. Second-law efficiency of solar-thermal cavity receivers. Report no. JPL 83-97 Pasadena, CA: Jet Propulsion Laboratory.

Naidoo, P., Van Niekerk, T.I., 2011. Optimising position control of a solar parabolic trough. *South African Journal of Science*, Vol. 107(3/4), pp. 452.

NDI, Nickel Development Institute, 2014. High temperature characteristics of stainless steel, a designers' handbook series. 9004. American Iron and Steel Institute. Available at: www.nickelinstitute.org. [Last accessed on 2014/03/11].

Neber, M., Lee, H., 2012, Design of a high temperature cavity receiver for residential scale concentrated solar power. *Energy*, Vol. 47, pp. 481-487.

Nellis, G.F., Pfotenhauer, J.M., 2005. Effectiveness-NTU relationship for a counterflow heat exchanger subjected to an external heat transfer. *Journal of Heat Transfer*, Vol. 127, pp. 1071-1073.

Newton, P., Copeland, C., Martinez-Botas, R., Seiler, M., 2012. An audit of aerodynamic loss in a double entry turbine under full and partial admission. *International Journal of Heat and Fluid Flow*, Vol. 33, pp. 70-80.

Nogueira, R.M., Martins, M.A., Ampessan, F., 2011. Natural convection in rectangular cavities with different aspect ratios. *Thermal Engineering*, Vol. 10, pp. 44-49.

Oğulata, R.T., Doba, F., Yilmaz, T., 2000. Irreversibility analysis of cross flow heat exchangers. *Energy Conversion and Management*, Vol. 41(15), pp. 1585-1599.

Onyegegbu, S.O., Morhenne, J., 1993. Transient multidimensional second law analysis of solar collectors subjected to time-varying insolation with diffuse components. *Solar Energy*, Vol. 50(1), pp. 85.

Ordóñez, J.C., Bejan, A., 2000. Entropy generation minimization in parallel-plates counterflow heat exchangers. *International Journal of Energy Research*, Vol. 24, pp. 843-864.

Otsuka, A., Hosono, K., Tanaka, R., Kitagawa, K., Arai, N., 2005. A survey of hemispherical total emissivity of the refractory metals in practical use. *Energy*, Vol. 30, pp. 535-543.

Outukumpu, 2013. High temperature austenitic stainless steel. Available at: www.outokumpu.com. [Last accessed on 2013/10/07].

Ozturk, M., 2010. Clean energy systems and experiences: Exergy analysis of low and high temperature water gas shift reactor with parabolic concentrating collector. Sciyo: Croatia.

Pattanasethanon, S., 2010. The solar tracking system by using digital solar position sensor. *American Journal of Engineering and Applied Sciences*, Vol. 3(4), pp. 678-682.

Paul Schertz, R.E., Shabbar, S., Luke, L., 1991. Development of an improved mirror facet for space applications. NASA CR-189109, National Aeronautics and Space Administration, Lewis Research Center.

Petela, R., 1964. Exergy of heat radiation. *ASME Journal of Heat Transfer*, Vol. 86, pp. 187-192.

Pietsch, A., Brandes, D.J., 1989. Advanced solar Brayton space power systems. In: Proceedings of the Intersociety Energy Conversion Engineering Conference (IECEC), Los Alamitos, CA, pp. 911-916.

Pitz-Paal, R., 2007. High temperature solar concentrators. Solar Energy Conversion and Photoenergy Systems, [Ed. Galvez, J.B. and Rodriguez, S.M.], in Encyclopedia of Life Support Systems (EOLSS), Developed under the Auspices of UNESCO, Eolss Publishers, Oxford. Available at: http://www.eolss.net. [Last accessed on 2014/08/24].

Pra, F., Tochona, P., Mauget, C., Fokkens, J., Willemsen, S., 2008. Promising designs of compact heat exchangers for modular HTRs using the Brayton cycle. *Nuclear Engineering and Design*, Vol. 238, pp. 3160-3173.

Prakash, M., Kedare, S.B., Nayak, J.K., 2009. Investigations on heat losses from a solar cavity receiver. *Solar Energy*, Vol. 83, pp. 157-170.

Prakash, M., 2013. Numerical studies on natural convection heat losses from open cubical cavities. *Journal of Engineering*, pp. 1-9.

Quero, M., Korzynietz, R., Ebert, M., Jiménez, A.A., del Río, A., Brioso, J.A., 2013. Solugas – operation experience of the first solar hybrid gas turbine system at MW scale. In: Proceedings of SolarPaces International Symposium of Solar Thermal.

Rayegan, R., Tao, Y.X., 2011. A procedure to select working fluids for Solar Organic Rankine Cycles (ORCs). *Renewable Energy*, Vol. 36, pp. 659-670.

Reddy, K.S., Sendhil Kumar, N., 2008. Combined laminar natural convection and surface radiation heat transfer in a modified cavity receiver of solar parabolic dish. *International Journal of Thermal Sciences*, Vol. 47, pp. 1647-1657.

Reddy, K.S., Sendhil Kumar, N., 2009. An improved model for natural convection heat loss from modified cavity receiver of solar dish concentrator. *Solar Energy*, Vol. 83, pp. 1884-1892.

Reddy, R.S., Kaushik, S.C., Tyagi, S.K., 2012. Exergetic analysis and performance evaluation of parabolic trough concentrating solar thermal power plant (PTCSTPP). *Energy*, Vol. 39, pp. 258-273.

Remund, J., Kunz, S., Lang, R., 1999. METEONORM: Global meteorological database for solar energy and applied climatology. Available at: www.meteonorm.com. [Last accessed on 2014/10/30].

Renberg, U., 2008. 1D engine simulation of a turbocharged SI engine with CFD computation on components. Dissertation: Department of Machine Design, Royal Institute of Technology, S-100 44 Stockholm, ISSN 1400-1179.

Reuter S, Koch A, Kaufmann A., 2010. Extension of performance maps of radial turbocharger turbines using pulsating hot gas flow. In: Proceedings of the 9th International Conference on Turbocharging and Turbochargers, London, pp. 262-280.

Richmond, J.C., Stewart, J.E., 1959. Spectral emittance of ceramic-coated and uncoated specimens of inconel and stainless steel. *Journal of the American Ceramic Society*, Vol. 42(1).

Roco, J.M.M., Velasco, S., Medina, A., Calvo Hernández, A., 1997. Optimum performance of a regenerative Brayton thermal cycle. *Journal of Applied Physics*, Vol. 82(6), pp. 2735-2741.

Rogiers, F., Stevens, T., Baelmans, M., 2006. Optimal recuperator design for use in a micro gas turbine. In: Proceedings of the Sixth International Workshop on Micro and Nanotechnology for Power Generation and Energy Conversion Applications, Nov. 29 - Dec. 1, 2006, Berkeley, USA, pp. 133-136.

Saitoh, T., Hirose, K., 1989. High-accuracy bench mark solutions to natural convection in a square cavity. *Computational Mechanics*, Vol. 4, pp. 417-427.

Salamon, P., Hoffmann, K.H., Schubert, S., Berry, S., Andresen, B., 2001. What Conditions Make Minimum Entropy Production Equivalent to Maximum Power Production? *Journal of Non-Equilibrium Thermodynamics,* Vol. 26, pp. 73-83.

Sendhil Kumar, N., Reddy, K.S., 2008. Comparison of receivers for solar dish collector system. *Energy Conversion and Management*, Vol. 49, pp. 812-819.

Shaaban, S., 2004. Experimental investigation and extended simulation of turbocharger non-adiabatic performance. Dissertation: Hannover.

Shah, R.K., 2005. Compact heat exchangers for micro-turbines. Available at: https://www.cso.nato.int/pubs/rdp.asp?RDP=RTO-EN-AVT-131. [Last accessed on 2014/10/30].

Shiraishi, K., Ono, Y., 2007. Hybrid turbocharger with integrated high speed motorgenerator. Mitsubishi Heavy Industries, Ltd. Technical Review, Vol. 44 (1).

Shuai, Y., Xia, X., Tan, H., 2008. Radiation performance of dish solar concentrator/cavity receiver systems. *Solar Energy*, Vol. 82, pp. 13-21.

Snyman, J.A., 2009. Practical mathematical optimization, Pretoria: University of Pretoria.

SolarPaces Guidelines, 2011. Measurement of solar weighted reflectance of mirror materials for concentrating solar power technology with commercially available instrumentation. Interim Version 1.1, May; 2011.

Sonntag, R.E., Borgnakke, C., Van Wylen, G.J., 2003. Fundamentals of thermodynamics. New York: John Wiley & Sons, Inc.

Spisz, E.W., Weigand, A.J., Bowman, R.L., Jack, J.R., 1969. Solar absorptances and spectral reflectances of 12 metals for temperatures ranging from 300 to 500 K. NASA Technical Note TN D-5353, National Aeronautics and Space Administration, Lewis Research Center.

Stafford, B., Davis, M., Chambers, J., Martínez, M., Sanchez, D., 2009. Tracker accuracy: field experience, analysis, and correlation with meteorological conditions. In: Proceedings of the 34th Photovoltaic Specialists Conference.

Steinfeld, A., Schubnell, M., 1993. Optimum aperture size and operating temperature of a solar cavity-receiver. *Solar Energy*, Vol. 50(1), pp. 19-25.

Stevens, T., Verplaetsen, F., Baelmans, M., 2004. Requirements for recuperators in micro gas turbines. In: Proceedings of the Fourth International Workshop on Micro and Nanotechnology for Power Generation and Energy Conversion Applications, Kyoto, Japan, pp. 96-99.

Stevens, T., Baelmans, M., 2008. Optimal pressure drop ratio for micro recuperators in small sized gas turbines. *Applied Thermal Engineering*, Vol. 28, pp. 2353-2359.

Stine, B.S., Harrigan, R.W., 1985, Solar energy fundamentals and design. New York: John Wiley & Sons, Inc.

SunEarthTools, 2014, SunEarthTools.com, Tools for consumers and designers of solar. Available at: http://www.sunearthtools.com/dp/tools/pos_sun. [Last accessed on 2014/07/29].

Swift, W., 1993. Preliminary design for a reversible Brayton cycle cryogenic cooler. Hanover: Creare Inc.

Tiasa, 2001. Thermal Insulation Handbook. The Thermal Insulation Association of Southern Africa, Association of Architectural Aluminium Manufacturers of South Africa. Available at: www.aaamsa.co.za. [Last accessed on 2014/08/16].

Torchia-Nunez, J.C., Porta-Gandara, M.A., Cervantes-de Gortari, J.G., 2008. Exergy analysis of a passive solar still. *Renewable Energy*, Vol. 33, pp. 608-616.

Torres-Reyes, E., Cervantes de Gortari, J.G., Ibarra-Salazar, B.A., Picon-Nunez, M., 2001. A design method of flat-plate solar collectors based on minimum entropy generation. *Exergy*, Vol. 1(1), pp. 46-52.

Traverso, A., Massardo, A.F., 2005. Optimal design of compact recuperators for microturbine application. *Applied Thermal Engineering*, Vol. 25, pp. 2054-2071.

Tsai, B., Wang, Y.L., 2009. A novel Swiss-Roll recuperator for the microturbine engine. *Applied Thermal Engineering*, Vol. 29, pp. 216-223.

Tyagi, S.K., Chen, J., Kaushik, S.C., 2005. Optimal criteria based on the ecological function of an irreversible intercooled regenerative modified Brayton cycle. *International Journal of Exergy*, Vol. 2(1), pp. 90-107.

Tyagi, S.K., Chen, G.M., Wang, Q., Kaushik, S.C., 2006. Thermodynamic analysis and parametric study of an irreversible regenerative-intercooled-reheat Brayton cycle. *International Journal of Thermal Sciences*, Vol. 45:829-40.

Ultiainen, E., Sundén, B., 2002. Evaluation of the cross corrugated and some other candidate heat transfer surfaces for microturbine recuperators. *Transactions of the ASME*, Vol. 124, pp. 550-560.

Valkonen, E., Karlsson, B., 1982. Spectral selectivity of a thermally oxidized stainless steel. *Solar Energy Materials*, Vol. 7, pp. 43-50.

Vasseur, P., Robillard, L., 1982. Natural convection in a rectangular cavity with wall temperature decreasing at a uniform rate. *Wärme- und Stoffübertragung*, Vol. 16, pp. 199-207.

Wahlström, J., Eriksson, L., 2011. Modeling diesel engines with a variable-geometry turbocharger and exhaust gas recirculation by optimization of model parameters for capturing non-linear system dynamics. In: Proceedings of the Institution of Mechanical Engineers, Part D, Journal of Automobile Engineering, Vol. 225(7), July.

Wallis, R.A., 1989. The thermal performance of an Ultra High Power (UHP) electrical furnace for the reheating of steel slabs, Appendix A, Properties of High Temperature Ceramic Fibres. Dissertation: Cranfield Institute of Technology.

Wang, W., Chen, L., Sun, F., Wu, C., 2005. Power optimization of an endoreversible closed intercooled regenerated Brayton cycle. *International Journal of Thermal Sciences*, Vol. 44, pp. 89-94.

Watson, N., Janota, M., 1982. Turbocharging the internal combustion engine. Hong Kong: The Mechanical Press Ltd.

Wen, C., 2010. Investigation of steel emissivity behaviors: examination of multispectral radiation thermometry (MRT) emissivity models. *International Journal of Heat and Mass Transfer*, Vol. 53, pp. 2035-2043.

Westin, F., 2005. Simulation of turbocharged SI-engines - with focus on the turbine. Dissertation: KTH School of Industrial Engineering and Management, TRITA – MMK 2005:05, Royal Institute of Technology, Stockholm.

Weston, K.C., 2000. Energy Conversion. [e-book]. Tulsa: Brooks/Cole. Available at: http://www.personal.utulsa.edu/~kenneth-weston. [Last accessed on 2014/08/25].

White, F.M., 2005. Fluid mechanics. 5th ed., Rhode Island: McGraw-Hill.

Willis, H.L., Scott, W.G., 2000. Distributed power generation. Taylor and Francis Group.

Wilson, D.G., Korakianitis T., 1998. The design of high-efficiency turbomachinery and gas turbines, 2nd ed., New Jersey: Prentice Hall.

Wong, L.T., Chow, W.K., 2001. Solar radiation model. *Applied Energy*, Vol. 69, pp. 91-224.

Wu, C., Chen, L., Sun, F., 1996. Performance of a regenerative Brayton heat engine. *Energy*, Vol. 21(2), pp. 71-76.

Xin S, Le Quéré P., 2006. Natural-convection flows in air-filled, differentially heated cavities with adiabatic horizontal walls. *Numerical Heat Transfer Part A*, Vol. 50(5), pp. 437-466.

Xu, C., Wang, Z., Li, X., Sun, F., 2011. Energy and exergy analysis of solar power tower plants. *Applied Thermal Engineering*, Vol. 31, pp. 3904-3913.

Yilmaz, M., Sara, O.N., Karsli, S., 2001. Performance evaluation criteria for heat exchangers based on second law analysis. *Exergy, an International Journal*, Vol. 1(4), pp. 278-294.

Zhang, Y., Lin, B., Chen, J., 2007. Optimum performance characteristics of an irreversible solar-driven Brayton heat engine at the maximum overall efficiency. *Renewable Energy*, Vol. 32, pp. 856-867.

Zhuge, W., Zhang, Y., Zheng, X, Yang, M., He, Y., 2009. Development of an advanced turbocharger simulation method for cycle simulation of turbocharged internal combustion engines. In: Proceedings of the Institution of Mechanical Engineers, Part D: Journal of Automobile Engineering. 223: 661. DOI: 10.1243/09544070JAUTO975.

Zukauskas, A., 1972. Convection heat transfer in cross flow. *Advances in Heat Transfer,* Vol. 8, pp. 93-106.

APPENDIX A – MEASURED DATA (SOLYS 2)

Date and time	Record Number	Global Horizontal Irradiance (GHI) (W/m²)	Direct Normal Irradiance (DNI) (W/m²)	Diffuse Horizontal Irradiance (DHI) (W/m²)	Air Temperature (°C)	Barometric Pressure (mbar)	Relative Humidity (%)	Rain (mm)	Wind Speed (m/s)	Wind Direction (Deg)	Wind Direction (Standard Deviation) (Deg)	Elevation (Deg)	Azimuth (Deg)
SAURAN, TOA5, UPR - GIZ University of Pretoria, Latitude: -25.75308, Longitude: 28.22859, Elevation: 1410 m **From www.sauran.net**												**Sun position** **From www.sunearthtools.com**	
Day 1, Test 1													
2014/07/01 12:38	248528	622.159	787.896	102.371	21.68	870	31.7	0	0.271	211.1	12.98		
2014/07/01 12:39	248529	621.347	785.933	102.678	21.97	870	30.33	0	0.898	207.4	18.66		
2014/07/01 12:40	248530	628.43	795.712	103.641	22.2	870	28.86	0	0.604	161.1	15.85	40.58°	9.39°
2014/07/01 12:41	248531	630.343	798.125	104.844	22.31	870	29.55	0	0.088	223.1	16.45		
2014/07/01 12:42	248532	629.519	795.717	105.844	22.7	869	29.08	0	0.479	200.3	26.07		
2014/07/01 12:43	248533	630.137	796.278	106.734	23.02	870	28.1	0	0.461	196.7	14.37		
2014/07/01 12:44	248534	621.663	783.661	106.359	22.87	869	28.37	0	1.529	192	17.8		
2014/07/01 12:45	248535	612.059	769.607	106.329	22.53	869	28.27	0	0.696	97.4	29.94		
2014/07/01 12:46	248536	602.685	756.641	106.464	21.81	869	30.02	0	0.464	202.6	30.18		
2014/07/01 12:47	248537	601.07	755.123	106.2	21.8	869	29.1	0	0.338	193.9	18.54		
2014/07/01 12:48	248538	596.003	748.618	106.052	21.92	869	28.83	0	0.075	89.7	22.63		
2014/07/01 12:49	248539	602.843	759.236	106.052	22.01	869	30.33	0	1.022	240.2	24.08		
2014/07/01 12:50	248540	608.535	768.359	106.052	22.04	870	28.19	0	0.405	215.8	16.89	40.89°	6.38°
2014/07/01 12:51	248541	613.346	776.234	106.052	21.91	869	28.43	0	0.361	192.1	19.39		
2014/07/01 12:52	248542	618.84	784.934	106.224	21.91	869	27.88	0	0.309	265	56.69		
2014/07/01 12:53	248543	624.8	793.977	106.647	21.62	869	28.86	0	0.405	287.9	38.39		
2014/07/01 12:54	248544	620.678	788.938	106.789	21.6	869	28.71	0	0.265	63.95	39.59		
2014/07/01 12:55	248545	617.372	784.788	106.985	21.55	869	29.2	0	1.045	79.68	20.65		
2014/07/01 12:56	248546	614.851	781.127	107.537	21.34	869	29.67	0	1.357	70.87	25.37		
2014/07/01 12:57	248547	614.016	779.887	108.083	20.78	869	30.16	0	1.777	50.61	24.13		
2014/07/01 12:58	248548	617.653	785.466	108.562	20.4	869	30.43	0	3	80.2	12.82		
2014/07/01 12:59	248549	618.769	787.748	108.998	19.97	869	30.93	0	2.507	71.02	12.01		
2014/07/01 13:00	248550	612.663	780.018	108.814	19.71	869	31.03	0	1.661	73.29	25.52	41.08°	3.34°
2014/07/01 13:01	248551	608.343	774.658	108.63	19.75	869	31.33	0	2.434	69.99	24.2		
Day 1, Test 2													

A1

2014/07/01 14:36	248646	457.528	722.349	92.2003	21.44	868	27.26	0	0.003	144.7	0.003		
2014/07/01 14:37	248647	453.152	717.574	91.6604	21.75	868	26.67	0	0.191	137.8	28.33		
2014/07/01 14:38	248648	451.347	717.254	91.6604	22.1	868	25.75	0	0.039	112.7	27.64		
2014/07/01 14:39	248649	449.019	715.796	91.4395	22.39	868	25.94	0	0.286	223.2	39.4		
2014/07/01 14:40	248650	446.04	714.155	90.9364	22.59	868	25.63	0	1.022	57.7	29.11	36.61°	334.28°
2014/07/01 14:41	248651	443.75	711.655	91.2003	22.01	868	25.89	0	3	63.98	12.8		
2014/07/01 14:42	248652	439.131	703.533	91.9672	20.96	868	27.52	0	3.904	79.55	10.97		
2014/07/01 14:43	248653	437.715	702.746	92.3966	20.43	868	28.3	0	2.532	104.9	19.96		
2014/07/01 14:44	248654	438.302	707.368	92.3966	20.46	868	28.25	0	2.241	62.85	19.45		
2014/07/01 14:45	248655	438.136	710.226	92.3966	20.51	868	27.64	0	1.999	49.07	26.43		
2014/07/01 14:46	248656	432.472	701.937	92.3966	20.44	868	28.04	0	1.87	80.6	8.92		
2014/07/01 14:47	248657	427.33	695.733	92.2494	20.4	868	28.28	0	1.916	38.65	24.56		
2014/07/01 14:48	248658	425.997	696.469	91.6972	20.41	868	27.57	0	3.575	66.95	16.05		
2014/07/01 14:49	248659	427.496	701.725	92.323	20.22	868	28.36	0	3.992	82	9.62		
2014/07/01 14:50	248660	424.658	698.489	92.3721	20.09	868	28.14	0	3.763	88.6	7.915	35.59°	331.73°
2014/07/01 14:51	248661	424.683	701.915	92.2739	19.92	868	28.2	0	3.237	89.1	13.07		
2014/07/01 14:52	248662	423.624	703.891	91.7034	19.92	868	28.68	0	2.901	83.2	14.18		
2014/07/01 14:53	248663	420.371	701.893	91.3536	20.12	868	28.6	0	2.569	93.1	18.01		
2014/07/01 14:54	248664	415.089	695.769	90.4579	20.38	868	27.57	0	2.37	98	22.69		
2014/07/01 14:55	248665	409.431	687.553	90.1389	20.35	868	27.69	0	3.255	89	7.259		
2014/07/01 14:56	248666	403.04	678.163	89.4579	20.16	868	28.02	0	3.043	79.16	12.04		
Day 2, Test 1													
2014/07/02 11:17	249887	639.296	855.084	86.7415	16.09	870	40.26	0	1.168	349.9	33.76		
2014/07/02 11:18	249888	639.467	854.944	86.594	16.15	870	39.29	0	1.463	334	16.3		
2014/07/02 11:19	249889	639.881	854.789	86.2622	16.01	870	39.32	0	1.656	346.6	22.63		
2014/07/02 11:20	249890	640.653	855.292	85.869	15.94	870	39.76	0	1.192	37.34	29.24	26°	44.06°
2014/07/02 11:21	249891	643.634	859.815	85.8566	15.95	870	39.5	0	1.31	62.96	12.67		
2014/07/02 11:22	249892	645.242	860.624	85.8565	15.87	870	40.2	0	2.097	23.33	23.14		
2014/07/02 11:23	249893	645.925	859.857	86.1819	15.97	870	40.26	0	0.738	2.32	71.38		
2014/07/02 11:24	249894	646.263	859.849	86.5933	16.42	870	39.39	0	0.485	198.7	29.26		
2014/07/02 11:25	249895	646.32	859.301	86.3537	16.94	870	37.66	0	0.229	226.3	41.55		
2014/07/02 11:26	249896	646.224	858.672	85.9975	17.26	870	37.4	0	0.526	255.5	45.4		
2014/07/02 11:27	249897	647.245	860.321	85.8562	17.51	870	37.49	0	0.417	156.5	57.31		
2014/07/02 11:28	249898	647.966	860.868	85.5184	17.63	870	37.3	0	0.323	260.8	32.96		
2014/07/02 11:29	249899	647.966	859.897	85.7394	17.68	870	36.2	0	0.534	97.5	51.54		
2014/07/02 11:30	249900	649.479	860.524	85.8684	17.6	870	36.34	0	0.42	101	65.62	27.54°	42.15°
2014/07/02 11:31	249901	648.323	857.539	86.2859	17.53	870	37.04	0	0.691	185.2	22.87		
2014/07/02 11:32	249902	649.147	857.51	86.2245	17.73	870	35.87	0	0.946	272.6	59.59		
2014/07/02 11:33	249903	651.317	857.43	86.5868	17.42	870	36.6	0	0.389	148.3	52.46		
2014/07/02 11:34	249904	653.271	858.575	86.7956	16.99	870	37.54	0	0.882	258.5	52.84		

A2

Day 2, Test 2													
2014/07/02 12:27	249957	650.183	832.678	95.2787	19.22	869	32.47	0	0.15	205.8	24.03		
2014/07/02 12:28	249958	647.728	828.88	95.1493	19.14	869	32.13	0	1.831	202.7	13.97		
2014/07/02 12:29	249959	649.118	830.081	95.6709	18.93	869	33.35	0	2.084	169.1	15.57		
2014/07/02 12:30	249960	648.593	829.277	96.4015	18.44	869	33.76	0	1.225	147.6	27.99	40.21°	12.43°
2014/07/02 12:31	249961	651.389	832.458	97.525	17.93	869	34.71	0	0.541	34.76	41.9		
2014/07/02 12:32	249962	651.165	831.574	98.3539	17.96	869	34.26	0	0.619	319	45.93		
2014/07/02 12:33	249963	647.631	825.959	98.8691	17.83	869	34.11	0	0.684	76.42	23.73		
2014/07/02 12:34	249964	650.834	830.816	99.1145	17.74	869	35.3	0	0.444	253.7	65.75		
2014/07/02 12:35	249965	651.21	831.844	99.1266	18.19	869	33.85	0	0.776	42.26	32.44		
2014/07/02 12:36	249966	649.646	830.07	99.1143	18.63	869	33.29	0	0.465	284.3	25.63		
2014/07/02 12:37	249967	649.614	829.815	99.0898	18.89	869	32.6	0	1.086	333.9	34.23		
2014/07/02 12:38	249968	644.667	822.972	98.746	18.77	869	33.02	0	0.885	290.8	30.09		
2014/07/02 12:39	249969	640.62	817.02	98.9058	18.83	869	32.64	0	1.9	286.8	21.99		
2014/07/02 12:40	249970	636.944	810.49	99.5629	18.66	869	32.92	0	1.625	335.8	20.72	40.64°	9.46°
2014/07/02 12:41	249971	634.547	806.846	100.152	18.14	869	33.81	0	1.081	294.6	18.01		
2014/07/02 12:42	249972	628.29	798.353	100.213	18.12	869	33.73	0	0.934	296.7	18.34		
2014/07/02 12:43	249973	629.981	801.891	100.44	18.43	869	33.54	0	0.108	347.4	30.5		
2014/07/02 12:44	249974	626.93	799.024	99.5623	18.89	869	32.52	0	0.715	24.83	46.81		
2014/07/02 12:45	249975	630.869	805.825	99.894	18.69	869	33.93	0	2.161	57.44	17.53		
2014/07/02 12:46	249976	636.054	814.136	100.207	18.23	869	33.76	0	1.21	13.7	42.58		
2014/07/02 12:47	249977	640.165	820.125	100.213	18.03	869	34.26	0	1.4	4.001	38.83		
2014/07/02 12:48	249978	638.656	818.291	100.778	17.69	869	34.74	0	2.607	55.43	28.67		
2014/07/02 12:49	249979	641.262	822.276	101.231	17.14	869	35.66	0	2.069	55.59	10.88		
2014/07/02 12:50	249980	642.592	825.356	101.513	16.78	869	36.29	0	2.659	67.52	12.03	40.95°	6.45°
2014/07/02 12:51	249981	643.87	828.246	101.678	16.57	869	36.82	0	2.293	52.84	6.369		
2014/07/02 12:52	249982	646.444	832.887	101.917	16.38	869	37.1	0	1.545	59.2	14.69		
Day 2, Test 3													
2014/07/02 14:26	250076	495.468	758.388	92.82	18.45	868	31.33	0	1.999	279.6	13.27		
2014/07/02 14:27	250077	493.139	757.878	92.55	18.31	868	32	0	2.078	275.8	16.68		
2014/07/02 14:28	250078	489.323	754.946	91.9792	18.49	868	31.26	0	1.176	235.4	32.17		
2014/07/02 14:29	250079	485.074	751.234	91.476	18.78	868	30.72	0	0.99	317.8	44.05		
2014/07/02 14:30	250080	479.879	745.495	91.0095	18.91	868	31.11	0	1.715	347.3	32.09	37.62°	336.93°
2014/07/02 14:31	250081	478.291	744.955	91.0893	18.62	868	31.27	0	2.176	356.9	12.81		
2014/07/02 14:32	250082	476.395	744.043	91.3225	18.07	868	32.58	0	2.145	354.6	29.23		
2014/07/02 14:33	250083	474.194	743.351	90.9788	18.07	868	31.56	0	2.804	322.7	12.45		
2014/07/02 14:34	250084	473.441	744.955	90.7149	18.25	868	31.45	0	2.293	327.7	21.97		
2014/07/02 14:35	250085	471.903	744.955	90.5861	18.1	868	31.71	0	1.543	286.7	29.31		
2014/07/02 14:36	250086	469.185	743.008	90.3344	18.02	868	32.96	0	1.114	290	45.31		
2014/07/02 14:37	250087	467.06	743.329	89.8496	18.29	868	31.47	0	0.461	294.5	48.3		

A3

2014/07/02 14:38	250088	464.61	742.541	89.3525	18.37	868	31.74	0	0.844	306.8	51.97		
2014/07/02 14:39	250089	462.485	742.592	89.0456	18.59	868	31.09	0	1.147	291.4	21.78		
2014/07/02 14:40	250090	459.243	740.66	88.5055	18.73	868	31.48	0	0.616	244.2	52.34	36.69°	334.29°
Day 3, Test 1													
2014/07/03 10:13	251263	525.546	780.279	88.182	17.75	870	37.76	0	0.165	202.1	43.75		
2014/07/03 10:14	251264	527.836	779.508	89.06	17.62	870	38.05	0	0.367	296.9	21.53		
2014/07/03 10:15	251265	525.782	772.472	89.5755	17.25	870	39.26	0	0.245	165.2	37.56		
2014/07/03 10:16	251266	526.877	771.555	89.5749	17.29	870	39.17	0	0.212	160.4	24.86		
2014/07/03 10:17	251267	527.078	769.724	89.5619	17.38	870	38.56	0	0.946	293.5	39.47		
2014/07/03 10:18	251268	541.582	792.942	89.1315	17.16	870	39.27	0	0.416	190.9	70.86		
2014/07/03 10:19	251269	542.007	791.267	89.0021	16.97	870	39.16	0	0.361	250.7	47.78		
2014/07/03 10:20	251270	536.927	779.014	89.825	16.99	870	40.21	0	0.243	177.8	23.3	26.02°	44.16°
2014/07/03 10:21	251271	535.385	773.886	90.3099	17.26	870	39.4	0	0.64	249.1	45.1		
2014/07/03 10:22	251272	542.084	783.308	90.3096	17.39	870	38.37	0	0.31	211.3	53.89		
2014/07/03 10:23	251273	545.628	787.343	89.9961	17.25	870	38.78	0	0.286	312	69.6		
2014/07/03 10:24	251274	542.758	779.165	90.2846	16.72	870	40.99	0	0.108	140	27.22		
2014/07/03 10:25	251275	545.305	779.784	91.0461	16.57	870	40.13	0	0.47	293.7	46.49		
2014/07/03 10:26	251276	546.122	778.081	91.6173	16.38	870	40.71	0	0.265	150.3	19.72		
2014/07/03 10:27	251277	556.648	792.724	92.5326	16.51	870	40.31	0	0.351	211.1	58.91		
2014/07/03 10:28	251278	551.128	779.123	93.2573	16.63	870	40.03	0	0.123	23.28	37.55		
2014/07/03 10:29	251279	546.605	770.821	92.7903	16.76	870	39.47	0	0.16	185.1	35.12		
2014/07/03 10:30	251280	552.985	781.063	91.3158	16.79	870	39.46	0	0.686	284	60.13	27.57°	42.24°
2014/07/03 10:31	251281	562.847	793.683	92.2495	16.58	870	40.07	0	1.168	278.1	30.02		
2014/07/03 10:32	251282	563.677	790.734	93.6992	16.31	870	40.73	0	0.374	228	62.71		
2014/07/03 10:33	251283	563.181	787.662	93.9935	16.38	870	40.31	0	0.335	139.5	45.31		
2014/07/03 10:34	251284	566.156	790.068	94.1037	16.26	870	40.76	0	1.016	267.4	34.29		
2014/07/03 10:35	251285	560.603	776.75	95.3873	16.16	870	41.18	0	0.928	281	21.78		
2014/07/03 10:36	251286	570.723	792.293	95.4603	16.21	870	41.41	0	0.412	267.3	55.99		
2014/07/03 10:37	251287	579.067	806.324	94.0519	16.51	870	39.92	0	1.346	289.1	42.15		
2014/07/03 10:38	251288	577.987	802.132	93.6576	16.18	870	40.97	0	2.522	294.7	15.76		
2014/07/03 10:39	251289	580.855	802.897	94.7316	15.67	870	42.59	0	1.904	289.8	39.49		
2014/07/03 10:40	251290	584.77	808.253	94.4172	15.72	870	41.54	0	0.328	131.6	62.61	29.05°	40.24°
2014/07/03 10:41	251291	584.961	804.154	96.007	15.88	870	41.16	0	1.008	293.6	30.45		
2014/07/03 10:42	251292	582.442	795.969	97.5608	15.82	870	42.12	0	0.462	250.4	26.48		
2014/07/03 10:43	251293	580.35	791.606	96.9582	16.04	870	41.57	0	1.039	207	57.63		
2014/07/03 10:44	251294	584.578	799.628	95.2311	16.14	870	41.09	0	1.61	277.9	37.41		
2014/07/03 10:45	251295	581.918	791.724	96.1202	15.93	870	41.4	0	1.24	283.7	33.39		
2014/07/03 10:46	251296	586.534	795.881	97.3598	15.84	870	41.91	0	0.66	122.7	40.23		
2014/07/03 10:47	251297	583.001	787.28	98.1078	16.12	870	41.01	0	0.304	145.8	39.5		
2014/07/03 10:48	251298	582.763	784.064	98.9417	16.29	870	40.45	0	0.622	260.9	52.86		
2014/07/03 10:49	251299	584.439	786.504	98.2102	16.4	870	40.52	0	0.531	204.2	56.12		

A4

2014/07/03 10:50	251300	591.376	798.308	96.8766	16.54	870	39.99	0	0.536	107.5	43.33	30.47°	38.16°
2014/07/03 10:51	251301	592.176	797.367	96.9004	16.48	870	40.64	0	0.668	159	45.54		
2014/07/03 10:52	251302	599.776	806.563	97.5812	16.35	870	40.57	0	1.003	277	24.05		
2014/07/03 10:53	251303	597.661	800.378	98.7224	16.33	870	40.54	0	1.379	268.6	33.57		
2014/07/03 10:54	251304	595.81	795.487	99.133	16.44	870	40.21	0	0.905	275.4	26.26		
2014/07/03 10:55	251305	598.774	797.772	99.476	16.53	870	40.37	0	0.921	272.8	27.09		
2014/07/03 10:56	251306	596.801	792.582	100.016	16.58	870	40.35	0	0.513	232.5	42.61		
2014/07/03 10:57	251307	596.581	790.709	100.605	16.75	870	39.61	0	0.069	162.6	11.55		
2014/07/03 10:58	251308	596.865	789.538	100.451	16.99	870	38.79	0	0.666	145.7	27.53		
2014/07/03 10:59	251309	599.717	792.6	100.186	17.07	869	37.88	0	0.126	183.4	32.73		
2014/07/03 11:00	251310	603.095	795.781	100.604	17.01	869	39.04	0	0.83	269.3	50.76	31.83°	35.99°
2014/07/03 11:01	251311	613.32	810.995	100.603	17.09	869	38.31	0	0.563	153.5	30.47		
2014/07/03 11:02	251312	617.503	817.245	100.253	17.18	869	38.19	0	0.626	212.8	51.51		
2014/07/03 11:03	251313	614.307	810.856	100.418	17.18	869	38.29	0	0.67	149.6	41.32		
2014/07/03 11:04	251314	606.309	795.49	101.658	17.21	869	38.54	0	0.47	235.4	56.05		
2014/07/03 11:05	251315	604.23	789.588	102.659	17.26	870	37.36	0	0.176	202.3	45.76		
2014/07/03 11:06	251316	609.802	797.349	102.812	17.52	869	36.68	0	0.586	257.3	18.8		
2014/07/03 11:07	251317	614.856	804.68	102.185	17.76	869	36.53	0	0.1	232.8	31.9		
2014/07/03 11:08	251318	614.808	804.165	101.337	17.64	869	36.82	0	0.198	25.23	54.93		
2014/07/03 11:09	251319	607.755	790.703	101.496	17.27	869	36.5	0	0.444	29.19	67.25		
2014/07/03 11:10	251320	609.554	791.255	102.073	17.18	870	37.87	0	0.784	259	69.5	33.12°	33.73°
2014/07/03 11:11	251321	620.171	806.453	102.165	17.32	869	37.31	0	0.294	138.7	48.02		
2014/07/03 11:12	251322	625.398	812.894	102.735	17.54	869	36.64	0	0.475	298.3	45.84		
2014/07/03 11:13	251323	616.092	795.844	103.638	17.67	869	36.53	0	0.603	250.1	45.75		
2014/07/03 11:14	251324	611.812	787.274	104.233	17.71	869	36.72	0	0.501	113.8	64.44		
2014/07/03 11:15	251325	615.246	790.805	104.823	17.78	869	35.16	0	0.542	189.5	58.28		
2014/07/03 11:16	251326	617.633	792.291	105.688	17.79	869	35.55	0	0.679	243.7	45.24		
2014/07/03 11:17	251327	616.143	787.692	106.21	17.8	869	36.34	0	0.547	234.1	50.17		
2014/07/03 11:18	251328	617.981	790.806	105.534	17.84	869	36.02	0	0.557	248.1	24.58		
2014/07/03 11:19	251329	622.661	797.3	105.061	17.9	869	34.78	0	1.181	224.1	19.06		
2014/07/03 11:20	251330	626.619	803.64	104.355	17.9	869	32.97	0	1.442	279.4	20.02	34.33°	31.37°
2014/07/03 11:21	251331	627.627	803.252	104.76	17.74	869	32.8	0	0.857	279.3	28.15		
2014/07/03 11:22	251332	632.204	809.25	105.018	17.71	869	33.19	0	0.585	297.9	30.49		
2014/07/03 11:23	251333	634.77	812.299	105.018	17.66	869	34.18	0	0.234	316.6	35.61		
2014/07/03 11:24	251334	632.873	807.606	105.54	17.72	869	33.64	0	1.117	327.2	16.29		
2014/07/03 11:25	251335	627.458	797.294	106.24	17.43	869	34.32	0	1.076	348.9	21.93		
2014/07/03 11:26	251336	624.131	790.478	107.087	17.33	869	35.01	0	0.25	204.9	35.68		
2014/07/03 11:27	251337	624.743	790.091	107.197	17.63	869	34.17	0	0.361	131.8	35.57		
2014/07/03 11:28	251338	629.04	794.804	107.836	17.73	869	33.99	0	0.301	122.8	12.47		
2014/07/03 11:29	251339	629.276	793.308	108.045	17.85	869	33.79	0	0.813	223.3	66.1		
2014/07/03 11:30	251340	633.439	797.489	108.702	17.84	869	34.72	0	0.248	294	47.67	35.46°	28.93°
2014/07/03 11:31	251341	632.028	792.804	109.58	17.99	869	33.32	0	0.438	175.7	57.06		
2014/07/03 11:32	251342	628.35	786.236	110.028	18.1	869	33.1	0	0.366	249.5	54.11		

A5

2014/07/03 11:33	251343	625.202	780.266	110.231	18.26	869	33.57	0	0.452	190.7	24.17		
2014/07/03 11:34	251344	626.913	782.55	110.489	18.29	869	32.58	0	0.167	219.1	30.91		
2014/07/03 11:35	251345	626.51	781.711	110.409	18.27	869	33.05	0	0.333	105.2	29.67		
2014/07/03 11:36	251346	626.114	780.477	110.544	18.47	869	32.54	0	0.652	245.6	30.24		
2014/07/03 11:37	251347	629.639	784.564	110.544	18.54	869	31.87	0	1.45	277.3	17.83		
2014/07/03 11:38	251348	631.682	785.899	110.777	18.19	869	32.7	0	0.926	275	34.4		
2014/07/03 11:39	251349	630.724	782.265	111.453	18.03	869	32.66	0	0.568	169.3	45.36		
2014/07/03 11:40	251350	630.392	779.835	112.245	17.96	869	32.19	0	0.461	166.6	51.22	36.51°	26.39°
2014/07/03 11:41	251351	630.162	777.74	112.847	17.81	869	32.2	0	0.585	238	68.18		
2014/07/03 11:42	251352	631.241	777.58	113.136	17.6	869	32.25	0	0.412	177.6	56.18		
2014/07/03 11:43	251353	630.96	776.96	113.283	17.5	869	32.78	0	0.364	173.8	57.49		
2014/07/03 11:44	251354	630.839	776.872	113.123	17.62	869	32.92	0	0.32	199.7	52.14		
2014/07/03 11:45	251355	629.843	775.354	113.123	17.76	869	32.22	0	1.071	266.8	26.51		
2014/07/03 11:46	251356	628.859	773.603	113.123	17.98	869	31.38	0	0.575	267.7	31.01		
2014/07/03 11:47	251357	628.808	772.267	113.467	17.86	869	32.37	0	0.689	263.9	30.81		
2014/07/03 11:48	251358	628.61	772.158	113.486	17.84	869	32.55	0	0.252	270.3	31.53		
2014/07/03 11:49	251359	630.571	775.697	113.031	18.12	869	31.33	0	0.149	244.7	48.5		
2014/07/03 11:50	251360	632.288	778.572	112.491	18.47	869	30.23	0	0.603	292.9	22.68	37.46°	23.77°
2014/07/03 11:51	251361	632.129	778.521	112.104	18.59	869	31.3	0	0.106	216.5	15.4		
2014/07/03 11:52	251362	631.503	778.273	111.92	18.86	869	30.79	0	1.236	212.6	18.61		
2014/07/03 11:53	251363	631.963	778.696	111.668	18.94	869	30.19	0	0.482	215.5	32.94		
2014/07/03 11:54	251364	633.751	781.112	111.65	18.73	869	30.22	0	0.054	144.7	36.04		
2014/07/03 11:55	251365	635.621	783.965	111.551	18.4	869	31.51	0	0.488	196.4	27.18		
2014/07/03 11:56	251366	638.61	789.219	111.115	18.63	869	29.81	0	0.281	127.6	66.76		
2014/07/03 11:57	251367	641.266	793.233	110.661	18.83	869	29.89	0	0.552	262.9	56.61		
2014/07/03 11:58	251368	641.074	792.452	110.538	18.99	869	30.86	0	0.482	141.1	57.34		
2014/07/03 11:59	251369	641.617	792.072	110.544	18.7	869	32.1	0	1.163	273.1	36.41		
2014/07/03 12:00	251370	641.438	792.554	110.206	18.37	869	32.17	0	0.421	264.1	13.7	38.32°	21.07°
Day 3, Test 2													
2014/07/03 12:25	251395	642.789	797.846	108.328	18.82	868	30.06	0	0.203	250.3	30.86		
2014/07/03 12:26	251396	643.941	799.636	108.426	18.96	868	28.91	0	1.911	340.3	17.34		
2014/07/03 12:27	251397	645.775	800.549	109.156	18.22	868	30.86	0	2.31	328.5	28.41		
2014/07/03 12:28	251398	643.091	797.234	109.431	17.73	868	31.27	0	2.491	343.5	18.39		
2014/07/03 12:29	251399	642.185	795.576	109.742	17.51	868	32.04	0	2.604	326.3	29.36		
2014/07/03 12:30	251400	645.248	801.521	109.649	17.61	868	30.92	0	0.898	349	30.32	40.28°	12.5°
2014/07/03 12:31	251401	649.079	806.774	109.568	17.57	868	31.24	0	2.246	347.5	20.83		
2014/07/03 12:32	251402	649.545	808.335	109.431	17.22	868	31.63	0	1.534	316.1	21.42		
2014/07/03 12:33	251403	648.831	807.372	109.467	17.22	868	31.99	0	2.391	346.6	9.98		
2014/07/03 12:34	251404	648.08	806.973	109.718	17.27	868	32.17	0	1.119	315.4	24.26		
2014/07/03 12:35	251405	646.309	805.78	109.325	17.61	868	31.53	0	0.831	32.45	69.54		
2014/07/03 12:36	251406	645.955	805.82	109.054	18.17	868	30.48	0	0.168	143.6	29.29		

A6

2014/07/03 12:37	251407	644.662	804.38	109.054	18.56	868	29.37	0	0.372	159.2	61.98		
2014/07/03 12:38	251408	642.573	801.605	109.054	18.72	868	29.72	0	0.472	140.8	43.66		
2014/07/03 12:39	251409	639.52	797.203	109.053	18.9	868	29.59	0	0.706	279.6	67.33		
2014/07/03 12:40	251410	637.788	795.159	109.053	18.88	868	29.32	0	0.498	215.1	48.55	40.71°	9.53°
2014/07/03 12:41	251411	636.549	793.319	109.053	18.75	868	29.37	0	1.423	292.3	22		
2014/07/03 12:42	251412	637.014	795.31	109.053	18.73	868	29.26	0	0.217	35.45	56.53		
2014/07/03 12:43	251413	637.536	796.475	109.052	19.08	868	28.58	0	0.139	181.7	32.26		
2014/07/03 12:44	251414	636.434	795.303	109.052	19.14	868	29.77	0	0.423	318.4	51.04		
2014/07/03 12:45	251415	633.884	792.548	109.051	19.24	868	29.16	0	0.054	293.1	28.74		
Day 3, Test 3													
2014/07/03 14:28	251518	468.04	702.965	98.5257	19.52	867	27.3	0	0.557	103.7	20.01		
2014/07/03 14:29	251519	465.445	700.034	98.6475	19.4	867	27.75	0	0.591	122.9	29.73		
2014/07/03 14:30	251520	463.755	699.194	99.0084	19.27	867	27.35	0	0.511	192	49.76	37.71°	336.94°
2014/07/03 14:31	251521	463.571	698.64	99.8359	18.86	867	28.49	0	1.722	148.5	21		
2014/07/03 14:32	251522	463.166	701.093	100.523	18.34	867	29.41	0	0.955	149.1	21.47		
2014/07/03 14:33	251523	461.056	671.465	100.503	18.36	867	28.27	0	0.465	126.3	8.62		
2014/07/03 14:34	251524	427.223	702.328	97.569	18.29	867	30.81	0	0.514	155.7	24.13		
2014/07/03 14:35	251525	457.291	699.902	99.8758	18.47	867	28.69	0	1.187	197.7	29.78		
2014/07/03 14:36	251526	453.472	696.097	99.4823	18.74	867	28.29	0	1.199	225.9	14.4		
2014/07/03 14:37	251527	451.101	695.413	98.7572	18.98	867	28.27	0	0.941	212.4	16.08		
2014/07/03 14:38	251528	448.921	696.084	97.9462	19.19	867	27.75	0	0.314	189.9	24.06		
2014/07/03 14:39	251529	445.58	694.335	97.2151	19.52	867	27.52	0	0.087	212.3	23.9		
2014/07/03 14:40	251530	442.717	692.506	96.8276	19.85	867	27.73	0	0.611	189.5	16.49	36.78°	334.29°
2014/07/03 14:41	251531	437.645	685.707	96.7096	19.98	867	27.04	0	0.374	227.7	48.12		
Day 4, Test 1													
2014/07/04 10:22	252712	547.975	794.784	89.2231	17.7	867	35.13	0	1.575	321	15.19		
2014/07/04 10:23	252713	550.869	796.66	89.5478	17.28	867	36.26	0	1.651	306	26.44		
2014/07/04 10:24	252714	558.315	807.46	89.2705	16.86	867	37.07	0	1.976	328	23.19		
2014/07/04 10:25	252715	561.548	810.919	88.7968	16.49	867	36.71	0	2.898	335.6	15.35		
2014/07/04 10:26	252716	558.307	802.66	89.3183	16.3	867	37.09	0	1.967	359.9	21.74		
2014/07/04 10:27	252717	564.485	808.625	90.1284	15.97	867	38.14	0	3.726	356.8	13.22		
2014/07/04 10:28	252718	570.241	815.881	90.1033	15.59	867	37.91	0	3.141	353.9	10.06		
2014/07/04 10:29	252719	570.001	813.074	90.4651	15.43	867	39.13	0	2.43	347	24.59		
2014/07/04 10:30	252720	570.88	811.312	91.3491	15.66	867	38.6	0	1.445	315.6	49.68	27.6°	42.34°
2014/07/04 10:31	252721	575.635	817.695	90.9312	16	867	37.52	0	1.726	297.9	22.23		
2014/07/04 10:32	252722	575.18	816.079	90.1877	16.15	867	37.96	0	1.207	307.4	35.22		
2014/07/04 10:33	252723	578.23	818.98	90.2795	16.28	867	37.42	0	0.728	293.2	37.38		
2014/07/04 10:34	252724	578.969	817.826	90.4267	16.47	867	36.99	0	0.183	242.5	31.43		
2014/07/04 10:35	252725	575.686	810.614	90.187	16.62	867	36.78	0	1.86	307.1	31.64		

A7

2014/07/04 10:36	252726	579.03	813.553	90.3526	16.56	867	36.56	0	2.029	324.5	18.67		
2014/07/04 10:37	252727	588.365	827.402	90.4875	16.3	867	37.35	0	1.364	299.4	30.99		
2014/07/04 10:38	252728	594.111	836.501	89.3758	16.33	867	36.22	0	2.46	339.6	22.41		
2014/07/04 10:39	252729	593.797	832.778	89.7994	16.16	867	37.38	0	3.629	338.4	5.813		
2014/07/04 10:40	252730	591.102	824.574	90.9969	15.85	867	37.94	0	3.054	341.2	16.61	29.09°	40.34°
2014/07/04 10:41	252731	587.851	815.481	92.3786	15.78	867	38.14	0	2.47	334.8	9.79		
2014/07/04 10:42	252732	590.385	819.07	91.8504	15.95	867	38.32	0	1.975	322.1	17.11		
2014/07/04 10:43	252733	598.724	832.008	90.6773	15.88	867	38.59	0	2.819	342.4	18.55		
2014/07/04 10:44	252734	594.624	823.885	90.8307	15.88	867	38.13	0	1.833	327.4	18.67		
2014/07/04 10:45	252735	597.427	826.198	91.0333	16.21	867	37.23	0	1.624	319.1	22.05		
2014/07/04 10:46	252736	600.44	828.73	91.3342	16.37	867	37.09	0	2.67	336.1	18.07		
2014/07/04 10:47	252737	602.771	830.467	91.6106	16.16	867	37.54	0	1.741	324.5	21.95		
2014/07/04 10:48	252738	597.72	819.921	92.1203	16.3	867	37.42	0	0.799	301.8	32.61		
2014/07/04 10:49	252739	595.81	815.44	92.1202	16.44	867	36.93	0	1.356	310.5	26.14		
2014/07/04 10:50	252740	604.52	827.685	92.0526	16.71	867	35.51	0	3.428	337.7	14.63	30.52°	38.26°
2014/07/04 10:51	252741	608.874	831.772	92.3413	16.43	867	37.38	0	3.42	324.2	10.32		
2014/07/04 10:52	252742	615.719	842.769	91.2419	16.29	867	36.12	0	3.572	330.4	12.5		
2014/07/04 10:53	252743	611.837	833.224	92.1508	16.11	867	36.67	0	3.294	357.2	16.66		
2014/07/04 10:54	252744	604.787	818.38	93.5633	15.93	867	37.42	0	2.189	10.87	20.34		
2014/07/04 10:55	252745	608.286	822.788	93.6063	16.07	867	37.6	0	1.64	347.4	38.54		
2014/07/04 10:56	252746	613.235	830.129	93.1273	16.42	867	37.38	0	1.267	303.6	36.42		
2014/07/04 10:57	252747	613.963	830.056	92.5254	16.66	867	36.89	0	2.301	293.7	23.19		
2014/07/04 10:58	252748	614.174	828.618	92.2368	16.79	867	35.25	0	2.087	288.5	31.84		
2014/07/04 10:59	252749	616.459	829.348	92.8816	16.59	867	35.89	0	3.275	318.6	18.18		
2014/07/04 11:00	252750	617.934	829.946	93.1457	16.34	867	35.99	0	2.246	297.5	22.93	31.88°	36.08°
2014/07/04 11:01	252751	621.025	833.916	92.9062	16.31	867	36.39	0	2.479	310.2	21.12		
2014/07/04 11:02	252752	623.988	837.82	92.6666	16.36	867	36.64	0	2.504	310.2	16.91		
2014/07/04 11:03	252753	628.713	843.95	92.5684	16.17	867	36.36	0	2.385	343.7	19.3		
2014/07/04 11:04	252754	630.992	846.249	92.8202	16.18	867	36.7	0	1.449	314.8	20.37		
2014/07/04 11:05	252755	629.888	843.315	92.6789	16.45	867	36.41	0	0.717	321.7	46.9		
2014/07/04 11:06	252756	621.453	827.728	93.508	16.75	867	36.06	0	0.619	6.023	46.42		
2014/07/04 11:07	252757	626.529	833.807	93.9072	17.12	867	35.05	0	0.492	138.5	42.63		
2014/07/04 11:08	252758	626.676	830.968	94.5152	17.35	867	34.57	0	0.828	154.8	57.37		
2014/07/04 11:09	252759	628.866	831.902	94.9021	17.38	867	34.3	0	0.629	212.9	49.92		
2014/07/04 11:10	252760	627.263	826.619	95.8847	17.31	867	34.56	0	1.091	313.2	38.6	33.17°	33.82°
2014/07/04 11:11	252761	622.538	816.468	96.9042	17.25	867	34.99	0	3.131	354.9	19.16		
2014/07/04 11:12	252762	630.335	828.246	96.4128	16.76	867	35.77	0	2.958	344.3	15.81		
2014/07/04 11:13	252763	630.775	828.063	96.2163	16.59	867	34.86	0	3.405	311.9	26.83		
2014/07/04 11:14	252764	631.19	824.612	97.7394	16.61	867	34.88	0	2.357	291.4	26.1		
2014/07/04 11:15	252765	631.72	821.62	99.4958	16.71	867	34.68	0	0.565	253.1	56.47		
2014/07/04 11:16	252766	631.669	818.818	100.423	16.9	867	34.62	0	0.822	261.2	55.14		
2014/07/04 11:17	252767	636.528	825.385	100.349	16.94	867	34.81	0	1.254	295	27.08		
2014/07/04 11:18	252768	638.437	828.472	99.7046	16.95	867	35.02	0	0.653	307.1	39.96		

A8

2014/07/04 11:19	252769	639.204	829.771	98.9861	17.18	867	34.27	0	0.97	329	27.82		
2014/07/04 11:20	252770	638.214	827.319	99.1212	17.37	867	32.5	0	1.222	341.9	35.32	34.38°	31.47°
2014/07/04 11:21	252771	636.484	822.802	99.5879	17.27	867	33.06	0	3.285	348.3	18.94		
2014/07/04 11:22	252772	638.533	823.97	100.018	16.9	867	34.08	0	3.307	329	9.83		
2014/07/04 11:23	252773	636.713	820.635	100.122	16.61	867	34.66	0	1.607	318.4	28.83		
2014/07/04 11:24	252774	635.066	817.884	99.6125	16.74	867	34.55	0	3.218	342.7	13.06		
2014/07/04 11:25	252775	640.96	826.101	99.5634	16.86	867	34.26	0	2.966	331.1	12.21		
2014/07/04 11:26	252776	645.41	832.61	99.072	17.01	867	33.53	0	1.935	302.6	37.02		
2014/07/04 11:27	252777	646.943	834.894	98.3105	17.12	867	32.94	0	1.101	320.7	31.72		
2014/07/04 11:28	252778	649.248	837.769	98.0157	17.13	866	33.41	0	0.668	294.5	49.08		
2014/07/04 11:29	252779	648.411	836.864	97.4876	17.44	866	32.72	0	1.161	118.6	51.13		
2014/07/04 11:30	252780	650.122	839.163	96.7199	17.75	866	31.82	0	0.312	163.1	32.51	35.52°	29.02°
2014/07/04 11:31	252781	654.056	845.468	95.725	17.79	866	32.3	0	0.508	211.1	68.16		
2014/07/04 11:32	252782	655.78	848.431	94.9082	17.78	866	32.41	0	1.094	149.8	71.45		
2014/07/04 11:33	252783	660.147	854.831	94.2081	17.79	867	32.34	0	0.983	212.9	65.43		
2014/07/04 11:34	252784	661.891	857.027	93.6554	17.63	866	32.52	0	0.608	279.9	61.55		
2014/07/04 11:35	252785	660.141	853.729	93.594	17.62	866	32.82	0	0.554	153.5	28.03		
2014/07/04 11:36	252786	660.843	853.327	93.7536	17.59	866	32.15	0	0.361	153	34.19		
2014/07/04 11:37	252787	661.916	853.751	93.9625	17.4	866	32.37	0	0.825	257.6	57.61		
2014/07/04 11:38	252788	662.184	853.451	93.9747	17.31	866	32.63	0	0.621	213.8	67.47		
2014/07/04 11:39	252789	664.853	857.662	93.7966	17.38	866	32.54	0	0.782	262.8	57.24		
2014/07/04 11:40	252790	663.634	854.634	94.3862	17.53	866	32.36	0	0.903	231.5	64.08	36.57°	26.49°
2014/07/04 11:41	252791	666.041	859.676	93.1702	17.79	866	34.29	0	0.771	271.8	47.21		
2014/07/04 11:42	252792	665.639	858.45	93.5203	18.16	866	31.53	0	0.58	298.2	55.2		
2014/07/04 11:43	252793	665.568	860.201	92.0464	18.5	866	30.03	0	1.248	338.8	35.48		
2014/07/04 11:44	252794	667.516	863.318	91.7823	18.44	866	31.01	0	0.818	31.58	37.29		
2014/07/04 11:45	252795	664.413	857.99	91.7884	18.33	866	30.39	0	2.502	3.642	24.83		
2014/07/04 11:46	252796	664.579	857.669	91.7823	17.92	866	30.56	0	2.331	332.1	26.54		
2014/07/04 11:47	252797	667.644	862.055	91.7639	17.68	866	31.21	0	0.652	293.3	62.84		
2014/07/04 11:48	252798	666.941	861.603	91.3831	17.86	866	30.91	0	0.379	346	22.24		
2014/07/04 11:49	252799	665.894	859.661	91.291	18.08	866	30.53	0	0.443	120.7	62.78		
2014/07/04 11:50	252800	667.433	861.048	90.9962	18.29	866	30.01	0	0.539	158.8	38.63	37.53°	23.86°
2014/07/04 11:51	252801	660.85	850.445	91.0146	18.4	866	29.89	0	0.678	148.6	32.67		
2014/07/04 11:52	252802	659.036	847.278	91.2357	18.52	866	29.09	0	1.019	310.3	16.33		
2014/07/04 11:53	252803	664.617	854.896	91.1129	18.34	866	29.6	0	1.914	284.5	35.5		
2014/07/04 11:54	252804	666.667	855.312	92.2797	18.05	866	29.98	0	0.884	289.4	39.43		
2014/07/04 11:55	252805	667.355	856.982	91.8743	17.94	866	30.04	0	0.224	207.6	49.2		
2014/07/04 11:56	252806	666.183	857.109	90.3692	17.95	866	30.19	0	2.145	18.55	24.49		
2014/07/04 11:57	252807	667.803	858.989	90.6391	17.51	866	31.25	0	3.12	39.36	19.71		
2014/07/04 11:58	252808	671.614	864.117	91.0074	17.27	866	31.47	0	3.045	28.14	12.6		
2014/07/04 11:59	252809	672.417	864.598	91.2959	17.11	866	31.78	0	3.113	17.77	13.25		
2014/07/04 12:00	252810	672.883	865.24	91.0871	16.97	866	31.94	0	2.267	26.44	17.25	38.39°	21.15°
2014/07/04 12:01	252811	672.468	864.751	90.8168	16.88	866	32.32	0	1.736	5.141	12.91		

A9

2014/07/04 12:02	252812	671.223	864.079	90.3931	16.89	866	32.6	0	1.449	31.85	32.47		
2014/07/04 12:03	252813	669.072	862.073	89.908	17.25	866	31.72	0	1.731	34.22	16.69		
2014/07/04 12:04	252814	667.591	859.527	89.9081	17.53	866	31	0	1.41	15.39	32.81		
2014/07/04 12:05	252815	668.564	860.121	90.0673	17.59	866	30.96	0	3.396	0.345	26.64		
2014/07/04 12:06	252816	670.217	860.914	90.6444	17.37	866	31.65	0	3.443	305.5	21.54		
2014/07/04 12:07	252817	674.664	867.478	90.7238	17.38	866	31.61	0	3.739	304.4	19.64		
2014/07/04 12:08	252818	670.366	861.324	90.6491	17.39	866	31.45	0	2.141	294.8	20.01		
2014/07/04 12:09	252819	670.016	861.406	90.3414	17.45	866	31.86	0	1.263	263	70.86		
2014/07/04 12:10	252820	661.459	849.903	89.8744	17.76	866	31.1	0	1.824	309.6	23.4	39.15°	18.37°
2014/07/04 12:11	252821	665.594	856.57	89.561	17.95	866	30.6	0	1.642	336.1	13.97		
2014/07/04 12:12	252822	667.87	860.331	89.4377	17.95	866	30.85	0	1.194	306.9	21.79		
2014/07/04 12:13	252823	667.616	859.872	89.1668	18.2	866	30	0	1.156	286.1	37.72		
2014/07/04 12:14	252824	667.761	859.65	89.1727	18.03	866	30.77	0	1.942	315.1	21.63		
2014/07/04 12:15	252825	669.335	861.894	89.3688	18.04	866	30.26	0	1.914	305.8	23.22		
2014/07/04 12:16	252826	666.857	857.405	89.7793	17.87	866	30.8	0	2.657	318.6	7.031		
2014/07/04 12:17	252827	669.076	861.283	89.9018	17.49	866	31.36	0	2.027	302.3	6.774		
2014/07/04 12:18	252828	669.582	862.036	89.9502	17.64	866	31.04	0	1.694	330.9	20.78		
2014/07/04 12:19	252829	669.455	861.831	90.2749	17.64	866	31.48	0	0.959	0.75	52.94		
2014/07/04 12:20	252830	670.49	862.904	90.3171	18.01	865	31.12	0	0.358	262.2	64.97	39.81°	15.51°
2014/07/04 12:21	252831	671.486	863.108	90.6356	18.19	865	30.53	0	2.13	288.7	22.76		
2014/07/04 12:22	252832	669.808	860.481	90.8436	18.08	865	30.97	0	2.308	297.2	17.68		
2014/07/04 12:23	252833	666.851	855.904	91.2971	17.97	865	31.4	0	1.147	284.2	39.29		
2014/07/04 12:24	252834	666.804	855.287	91.9651	18.06	865	31.39	0	1.566	278.4	51.13		
2014/07/04 12:25	252835	662.653	849.361	92.1054	18.4	865	30.89	0	0.712	195.4	21.81		
2014/07/04 12:26	252836	665.088	853.252	92.1049	18.7	865	30.35	0	0.737	291.1	47.91		
2014/07/04 12:27	252837	666.509	854.948	92.479	18.81	865	30.49	0	1.713	321.9	19.22		
2014/07/04 12:28	252838	671.888	862.066	93.2155	18.46	865	31.21	0	2.465	330.4	17.3		
2014/07/04 12:29	252839	675.676	867.913	93.6087	18.35	865	31.27	0	0.826	12.93	26.32		
2014/07/04 12:30	252840	672.466	863.836	93.8484	18.5	865	30.96	0	1.034	354.8	53.43	40.35°	12.58°
2014/07/04 12:31	252841	667.603	856.732	94.2601	18.79	865	30.39	0	0.826	16.7	25.38		
2014/07/04 12:32	252842	657.367	840.825	95.0835	18.77	865	31.13	0	1.568	52.3	37.55		
2014/07/04 12:33	252843	651.276	830.025	96.5386	18.67	865	31.23	0	0.75	310.6	21.91		
2014/07/04 12:34	252844	651.882	829.623	97.9447	18.93	865	30.54	0	0.374	264.1	37.8		
2014/07/04 12:35	252845	648.287	822.625	99.2894	19.29	865	30.03	0	1.756	333.2	27.29		
2014/07/04 12:36	252846	644.022	813.3	101.033	19.32	865	29.68	0	2.535	304.9	26.88		
2014/07/04 12:37	252847	645.298	812.438	102.648	18.69	865	31.77	0	2.332	299	27.3		
2014/07/04 12:38	252848	650.042	818.027	103.784	18.33	865	31.29	0	1.312	303	28.46		
2014/07/04 12:39	252849	650.967	819.201	104.208	18.06	865	31.89	0	2.87	300.4	23.79		
2014/07/04 12:40	252850	650.654	819.624	103.931	17.83	865	31.91	0	4.056	310.1	20.22	40.79°	9.6°
2014/07/04 12:41	252851	657.487	830.965	103.47	17.72	865	32.04	0	4.265	327.8	12.86		
2014/07/04 12:42	252852	657.279	832.827	102.597	17.77	865	32.27	0	2.572	305.2	26.92		
2014/07/04 12:43	252853	658.315	837.739	101.006	17.91	865	32.11	0	2.509	316.3	28.27		
2014/07/04 12:44	252854	661.051	844.885	99.3849	18.28	865	31.67	0	0.952	300.1	40.17		

A10

2014/07/04 12:45	252855	654.32	838.411	97.647	18.47	865	30.61	0	0.97	36.55	31.25		
2014/07/04 12:46	252856	647.974	832.362	96.0198	18.37	865	31.15	0	0.263	85.9	19.52		
2014/07/04 12:47	252857	645.994	831.771	95.0066	18.7	865	30.79	0	0.207	77.31	23.74		
2014/07/04 12:48	252858	648.88	837.944	94.1286	19.05	865	30.19	0	1.444	336	23.97		
2014/07/04 12:49	252859	648.651	837.04	94.6199	18.86	865	30.71	0	2.416	316.7	23.7		
2014/07/04 12:50	252860	647.494	835.134	95.0618	18.73	865	31.04	0	1.56	254.5	62.75	41.11°	6.58°
2014/07/04 12:51	252861	650.314	839.757	95.0492	18.82	865	30.37	0	1.617	274.6	48.85		
2014/07/04 12:52	252862	654.061	845.447	95.0491	18.34	865	31.12	0	1.395	277.4	42.56		
2014/07/04 12:53	252863	656.808	852.023	94.6433	18.11	865	32.57	0	1.137	270.9	34.13		
2014/07/04 12:54	252864	656.447	853.061	94.3112	18.27	865	31.1	0	1.739	294	19.38		
2014/07/04 12:55	252865	651.987	846.511	94.8018	18.37	865	31.88	0	1.493	280.1	14.8		
2014/07/04 12:56	252866	649.428	846.008	93.223	18.78	865	30.46	0	0.647	262	51.73		
2014/07/04 12:57	252867	647.701	845.253	92.099	18.99	865	31.36	0	0.931	239.9	67.96		
2014/07/04 12:58	252868	646.635	844.917	92.099	19.1	865	30.27	0	0.709	179.7	43.83		
2014/07/04 12:59	252869	644.03	840.926	92.4367	19.11	865	29.88	0	0.627	149	62.12		
2014/07/04 13:00	252870	645.398	844.218	92.2342	19.09	865	30.32	0	2.457	350.4	18.45	41.3°	3.53°
2014/07/04 13:01	252871	644.962	843.268	92.8419	18.52	865	31.12	0	3.732	18.57	28.78		
2014/07/04 13:02	252872	645.249	844.165	93.4743	18.11	865	31.5	0	4.17	336.5	21.52		
2014/07/04 13:03	252873	646.839	846.354	94.0453	17.77	865	31.9	0	4.294	12.55	27.79		
2014/07/04 13:04	252874	646.914	847.46	94.309	17.52	865	32.51	0	3.041	355.9	25.55		
2014/07/04 13:05	252875	649.112	851.884	94.3085	17.49	865	32.14	0	3.891	17.98	11.58		
2014/07/04 13:06	252876	648.867	852.697	94.1791	17.35	865	32.23	0	4.196	357.2	25.3		
2014/07/04 13:07	252877	645.92	849.978	93.5708	17.36	865	32.71	0	1.998	348.5	18.58		
2014/07/04 13:08	252878	644.875	850.316	93.564	17.6	865	31.99	0	3.038	354.4	23.3		
2014/07/04 13:09	252879	644.277	850.579	93.1704	17.54	865	32.29	0	2.04	328.1	13.06		
2014/07/04 13:10	252880	642.358	849.648	93.0716	17.72	865	32.1	0	1.254	300.2	33.72	41.38°	0.47°
2014/07/04 13:11	252881	644.672	855.166	92.7887	18.27	865	31.38	0	1.321	287.2	45.68		
2014/07/04 13:12	252882	643.174	853.293	92.8495	18.55	865	30.71	0	4.528	328.2	18.55		
2014/07/04 13:13	252883	627.448	828.885	93.5427	18.16	865	31.51	0	4.002	296.6	29.11		
2014/07/04 13:14	252884	610.861	803.545	94.0089	17.94	865	31.62	0	3.976	290.1	24.97		
2014/07/04 13:15	252885	598.386	785.143	94.3462	17.78	865	32.61	0	0.675	216.7	67.72		
2014/07/04 13:16	252886	575.186	750.976	94.5484	18.03	865	31.65	0	0.601	247.4	71.38		
2014/07/04 13:17	252887	565.487	736.535	95.1312	18.33	865	30.94	0	3.624	336.2	18.02		
2014/07/04 13:18	252888	554.506	717.171	96.4387	18.01	865	31.01	0	6.078	345.3	10.48		
2014/07/04 13:19	252889	503.47	637.586	97.6356	17.57	864	31.93	0	2.643	346.3	28.56		
2014/07/04 13:20	252890	472.146	588.298	99.3359	17.76	864	31.46	0	3.884	317.1	20.09	41.34°	357.4°
2014/07/04 13:21	252891	480.87	596.139	103.025	17.76	865	31.4	0	2.626	293.5	25.41		
2014/07/04 13:22	252892	531.642	668.513	108.379	17.52	865	32.32	0	2.05	289	41.1		
2014/07/04 13:23	252893	583.952	742.637	114.07	17.74	865	30.76	0	1.712	311.4	28.26		
2014/07/04 13:24	252894	599.775	760.932	118.551	17.8	865	30.69	0	1.178	284	41.87		
2014/07/04 13:25	252895	608.972	774.93	119.994	17.78	864	31.13	0	1.241	267	67.41		
2014/07/04 13:26	252896	606.705	776.622	117.802	18.07	864	30.53	0	0.951	299.7	32.77		
2014/07/04 13:27	252897	608.172	785.791	114.474	18.31	864	30.59	0	2.527	7.186	21.39		

A11

2014/07/04 13:28	252898	604.578	786.709	110.729	17.98	864	31.05	0	2.486	349.1	17.74		
2014/07/04 13:29	252899	602.254	789.56	107.911	17.59	864	31.92	0	4.428	17.63	14.26		
2014/07/04 13:30	252900	597.792	785.518	106.425	17.43	864	31.74	0	4.532	356.1	10.65	41.18°	354.34°
2014/07/04 13:31	252901	600.306	790.96	106.088	17.15	864	32.63	0	5.191	345.3	8.48		
2014/07/04 13:32	252902	603.517	798.05	106.063	17	864	32.73	0	3.562	352.4	17.98		
2014/07/04 13:33	252903	600.51	795.985	105.381	17.07	864	32.55	0	3.507	335.2	12.49		
2014/07/04 13:34	252904	596.092	790.981	105.105	17.17	864	32.41	0	3.208	338.7	19.13		
2014/07/04 13:35	252905	591.451	786.968	104.344	17.22	864	32.37	0	1.682	307.8	26.11		
2014/07/04 13:36	252906	588.624	785.334	103.877	17.63	864	31.58	0	2.375	356.1	31.76		
2014/07/04 13:37	252907	590.162	790.177	103.337	17.69	864	32.07	0	1.841	349.2	24.9		
2014/07/04 13:38	252908	589.632	790.87	103.521	17.81	864	31.87	0	1.748	304.9	29.82		
2014/07/04 13:39	252909	590.078	794.97	102.404	18.18	864	30.76	0	0.787	210.7	62.14		
2014/07/04 13:40	252910	589.58	795.772	102.404	18.26	864	30.86	0	2.079	294.4	34.42	40.9°	351.31°
2014/07/04 13:41	252911	592.402	801.345	102.729	18.26	864	31.27	0	1.119	226	63.07		
2014/07/04 13:42	252912	594.814	806.189	103.146	18.29	864	31.19	0	2.091	288.4	31.03		
2014/07/04 13:43	252913	594.291	807.327	103.14	18.33	864	30.41	0	0.97	275.5	53.62		
2014/07/04 13:44	252914	590.052	801.826	103.146	18.29	864	31	0	2.866	281.9	31.41		
2014/07/04 13:45	252915	586.905	798.609	103.466	18.35	864	30.48	0	2.055	299.1	35.48		
2014/07/04 13:46	252916	577.26	784.61	103.294	18.41	864	31.01	0	1.308	295.8	35		
2014/07/04 13:47	252917	569.122	773.427	103.177	18.5	864	30.62	0	2.311	285.7	56.97		
2014/07/04 13:48	252918	563.843	766.562	103.14	18.52	864	31.02	0	0.946	152.2	47.61		
2014/07/04 13:49	252919	556.892	757.137	103.14	18.5	864	34.06	0	0.688	224.6	40.77		
2014/07/04 13:50	252920	548.472	745.304	103.14	18.62	864	30.1	0	1.062	145.1	67.65	40.5°	348.32°
2014/07/04 13:51	252921	533.351	721.698	103.189	18.66	864	29.63	0	1.176	276.1	40.94		
2014/07/04 13:52	252922	522.595	705.897	103.14	18.56	864	30.86	0	0.88	205.8	60.85		
2014/07/04 13:53	252923	501.952	672.31	103.883	18.68	864	30.05	0	0.534	182.6	51.16		
2014/07/04 13:54	252924	486.294	648.835	103.46	18.86	864	29.99	0	1.864	335.3	26.18		
2014/07/04 13:55	252925	475.941	632.166	103.84	18.73	864	30.16	0	3.409	319.2	25.04		
2014/07/04 13:56	252926	457.053	599.608	105.203	18.43	864	30.34	0	3.912	350.3	18.63		
2014/07/04 13:57	252927	472.366	623.623	107.266	18.11	864	31.18	0	2.884	323.6	29.88		
2014/07/04 13:58	252928	489.773	650.352	109.758	18.17	864	30.65	0	3.136	306.1	24.23		
2014/07/04 13:59	252929	496.807	659.055	112.3	17.9	864	31.15	0	4.32	311.4	12.66		
2014/07/04 14:00	252930	508.942	677.803	114.566	17.68	864	31.01	0	3.023	307.2	19.55	39.99°	345.37°
2014/07/04 14:01	252931	523.636	701.651	116.248	17.54	864	31.18	0	3.892	323.9	10.55		
2014/07/04 14:02	252932	531.066	715.241	117.138	17.31	864	31.64	0	2.638	302.9	14.32		
2014/07/04 14:03	252933	531.506	718.831	117.138	17.55	864	31.55	0	1.994	350.5	32.78		
2014/07/04 14:04	252934	531.723	722.354	116.714	18.04	864	30.13	0	2.845	337.1	29.27		
2014/07/04 14:05	252935	530.076	723.106	115.278	17.93	864	30.75	0	3.048	336.2	12.74		
2014/07/04 14:06	252936	525.602	722.325	112.877	17.77	864	30.84	0	0.688	297.5	39.88		
2014/07/04 14:07	252937	530.804	737.469	110.986	18.1	864	30.2	0	1.542	318.7	31.1		
2014/07/04 14:08	252938	537.653	753.497	109.654	18.3	864	29.61	0	1.708	321.6	27.41		
2014/07/04 14:09	252939	537.43	757.939	108.512	18.33	864	29.74	0	0.949	27.57	29.28		
2014/07/04 14:10	252940	529.744	749.594	106.953	18.44	864	29.63	0	0.609	56.3	66.81	39.37°	342.49°

A12

2014/07/04 14:11	252941	520.77	740.198	104.786	18.71	864	29.32	0	0.612	101.5	38.16		
2014/07/04 14:12	252942	517.865	738.498	103.877	18.98	864	29.3	0	0.861	301.6	43.76		
2014/07/04 14:13	252943	514.648	734.756	103.877	18.97	864	30.33	0	1.308	262.4	52.42		
2014/07/04 14:14	252944	510.454	729.445	104.135	19.07	864	29.01	0	1.336	224.2	70.99		
2014/07/04 14:15	252945	503.599	717.518	104.712	18.99	864	28.91	0	3.931	294.9	23.34		
2014/07/04 14:16	252946	492.767	700.863	104.491	18.47	864	30.21	0	1.643	288.2	54.66		
2014/07/04 14:17	252947	489.275	699.061	103.877	18.43	864	29.91	0	1.168	236.6	56.06		
2014/07/04 14:18	252948	474.945	675.52	103.38	18.25	864	30.65	0	3.758	319.2	23.68		
2014/07/04 14:19	252949	471.434	672.303	103.177	18.06	864	30.57	0	3.618	315.8	23.25		
2014/07/04 14:20	252950	491.879	710.66	103.816	17.9	864	30.81	0	3.765	316.1	25.55	38.64°	339.68°
2014/07/04 14:21	252951	491.382	711.47	103.908	18.05	864	30.92	0	1.452	265.7	52.65		
2014/07/04 14:22	252952	490.424	712.615	103.902	18.33	864	30.42	0	0.967	285.5	59.05		
2014/07/04 14:23	252953	484.883	705.495	103.877	18.6	864	30.38	0	0.573	143.4	72.59		
2014/07/04 14:24	252954	478.143	696.829	103.417	18.96	864	31.07	0	0.843	263.7	53.69		
2014/07/04 14:25	252955	479.107	701.665	103.177	19.19	864	29.48	0	0.475	183.7	65.63		
2014/07/04 14:26	252956	476.1	699.389	102.52	19.08	864	29.16	0	1.72	289.4	41.39		
2014/07/04 14:27	252957	474.664	700.345	101.894	18.77	864	29.63	0	0.733	297.6	27.88		
2014/07/04 14:28	252958	470.528	698.069	100.955	18.64	864	29.54	0	0.942	338.2	11.47		
2014/07/04 14:29	252959	472.104	705.977	99.8865	18.95	864	29.01	0	0.511	327.5	26		
2014/07/04 14:30	252960	471.587	709.792	98.5665	19.15	864	29.22	0	0.885	311.9	32.27	37.81°	336.95°
2014/07/04 14:31	252961	468.172	708.698	97.1852	19.3	864	28.83	0	1.803	290.8	23.37		
2014/07/04 14:32	252962	467.183	711.229	96.3809	19.32	864	28.62	0	1.08	303.3	11.54		
2014/07/04 14:33	252963	465.6	712.491	95.6872	19.18	864	29.09	0	0.564	296.3	28.25		
2014/07/04 14:34	252964	466.666	719.867	94.5821	19.37	864	28.87	0	0.761	275.7	22.89		
2014/07/04 14:35	252965	466.819	725.25	93.4586	19.64	864	28.83	0	0.64	297.7	45.37		
2014/07/04 14:36	252966	467.496	730.43	92.8263	19.75	864	28.99	0	1.419	289.5	42.59		
2014/07/04 14:37	252967	465.725	729.601	92.8441	19.6	864	27.7	0	1.45	286.7	40.53		
2014/07/04 14:38	252968	466.081	730.445	93.7709	19.04	864	28.57	0	4.056	288.2	22.27		
2014/07/04 14:39	252969	464.044	729.867	93.7461	18.48	864	29.41	0	2.445	282.8	26.05		
2014/07/04 14:40	252970	462.492	732.142	92.8435	18.38	864	29.15	0	2.189	291.2	33.46	36.88°	334.3°
2014/07/04 14:41	252971	462.744	738.199	91.6948	18.39	864	29.52	0	2.832	293.6	17.36		
2014/07/04 14:42	252972	460.277	737.633	90.6567	18.34	864	29.8	0	2.189	281.3	32.9		
2014/07/04 14:43	252973	457.478	735.023	90.785	18.14	864	30.25	0	4.882	292.3	24.01		
2014/07/04 14:44	252974	456.363	735.68	91.3059	17.93	864	30.7	0	4.567	319.3	17.41		
2014/07/04 14:45	252975	456.08	739.658	90.7038	18.01	864	30.42	0	3.192	317.1	18.74		
2014/07/04 14:46	252976	457.877	747.161	90.5744	18.11	864	30.12	0	2.497	302.4	17.95		
2014/07/04 14:47	252977	457.62	752.088	89.5365	17.99	864	30.37	0	2.287	321.9	15.13		
2014/07/04 14:48	252978	456.827	756.784	88.4558	17.99	864	30.38	0	2.951	307.4	22.89		
2014/07/04 14:49	252979	457.029	761.952	87.5283	18.06	864	30.38	0	2.437	279.4	30.78		
2014/07/04 14:50	252980	455.547	763.337	86.9266	18.01	864	29.94	0	4.132	301.3	15.48	35.86°	331.73°
2014/07/04 14:51	252981	453.192	764.029	86.3004	17.88	864	30.3	0	3.004	306.7	20.51		
2014/07/04 14:52	252982	450.065	763.746	85.171	17.91	864	30.11	0	3.192	314.6	27.1		
2014/07/04 14:53	252983	445.341	759.061	84.4709	17.89	864	30.23	0	2.951	305.9	19.71		

A13

2014/07/04 14:54	252984	441.447	757.245	83.5379	17.93	864	30.25	0	1.106	285.7	28.28		
2014/07/04 14:55	252985	436.584	752.263	82.6477	18.27	864	29.84	0	2.202	296.2	31.66		
2014/07/04 14:56	252986	432.562	748.117	82.4879	18.18	864	30.19	0	2.577	308.3	24.57		
2014/07/04 14:57	252987	428.94	745.947	81.7938	18.29	864	29.62	0	1.576	296.8	31.32		
2014/07/04 14:58	252988	425.927	744.028	81.4069	18.5	864	29.8	0	0.668	199.4	61.14		
2014/07/04 14:59	252989	423.374	742.416	81.0325	18.56	864	28.69	0	4.054	325	11.96		
2014/07/04 15:00	252990	420.573	740.762	81.0327	18.26	864	29.06	0	3.174	344.6	13.8	34.75°	329.26°
2014/07/04 15:01	252991	417.273	737.952	80.787	17.92	864	30.36	0	3.99	334.6	13.07		
2014/07/04 15:02	252992	414.929	737.461	80.2957	17.95	864	29.51	0	3.739	336.4	9.92		
2014/07/04 15:03	252993	410.799	732.718	80.2279	17.78	864	30.08	0	3.7	338.2	7.544		
2014/07/04 15:04	252994	406.931	728.984	79.8044	17.67	864	30.09	0	3.794	323.2	19.62		
2014/07/04 15:05	252995	404.217	726.903	79.5647	17.76	864	30.2	0	3.417	316	20.63		
2014/07/04 15:06	252996	401.671	725.408	79.5586	17.87	864	30.17	0	3.459	315.2	15.67		
2014/07/04 15:07	252997	399.501	725.488	79.5586	17.94	864	30.51	0	2.59	305.4	25.07		
2014/07/04 15:08	252998	397.528	726.311	78.9999	18.21	864	30.81	0	0.991	273.4	44.57		
2014/07/04 15:09	252999	393.794	722.986	78.7176	18.51	864	30.17	0	1.178	274.7	39.12		
2014/07/04 15:10	253000	388.988	717.945	77.9625	18.77	864	29.62	0	0.405	150.4	34.24	33.56°	326.87°
2014/07/04 15:11	253001	385.713	716.149	77.3177	18.94	864	30.46	0	0.35	192.4	36.16		
2014/07/04 15:12	253002	381.474	712.703	76.6238	19.09	864	29.12	0	0.595	272.1	58.88		
2014/07/04 15:13	253003	379.512	713.976	75.9543	19.32	864	28.63	0	0.374	287	42.23		
2014/07/04 15:14	253004	378.668	717.438	75.5427	19.44	864	28.43	0	0.781	195.9	68.14		
2014/07/04 15:15	253005	376.617	718.645	74.9652	19.42	864	28.57	0	0.222	200.8	49.85		
2014/07/04 15:16	253006	373.294	717.2	74.3014	19.62	864	28.22	0	0.673	291.8	39.26		
2014/07/04 15:17	253007	369.895	714.561	73.6685	19.73	864	28.01	0	3.082	325.4	19.28		
2014/07/04 15:18	253008	367.455	713.389	73.6619	19.45	864	28.7	0	0.825	277.8	58.24		
2014/07/04 15:19	253009	365.174	712.808	73.6614	19.45	864	27.96	0	0.812	141.8	66.93		
2014/07/04 15:20	253010	362.522	710.43	73.5195	19.26	864	28.19	0	3.668	317	24.75	32.29°	324.58°
2014/07/04 15:21	253011	359.766	708.101	73.586	18.63	864	29.15	0	3.347	321.2	10.5		
2014/07/04 15:22	253012	357.324	707.568	72.9714	18.26	864	29.67	0	3.111	304.2	15.3		
2014/07/04 15:23	253013	355.106	708.363	72.8294	18.26	863	29.87	0	1.096	301	30.17		
2014/07/04 15:24	253014	353.742	711.533	72.1778	18.44	864	30.69	0	0.83	270.5	57.21		
2014/07/04 15:25	253015	351.841	712.829	71.5077	18.79	864	29.86	0	0.444	300	48.38		
2014/07/04 15:26	253016	348.985	711.895	71.2922	19.06	864	29.55	0	0.859	147.6	37.45		
2014/07/04 15:27	253017	345.874	708.956	70.7206	19.24	864	28.88	0	1.168	173.9	64.6		
2014/07/04 15:28	253018	342.743	704.806	70.7137	19	863	28.75	0	0.635	140	56.14		
2014/07/04 15:29	253019	339.083	700.693	70.7068	18.64	864	29.26	0	0.879	278.4	37.67		
2014/07/04 15:30	253020	333.981	693.336	70.602	18.47	864	29.49	0	0.728	285.5	65.48	30.95°	322.38°
2014/07/04 15:31	253021	329.71	688.7	70.0122	18.53	863	29.36	0	0.622	159.6	53.4		
2014/07/04 15:32	253022	326.657	688.323	69.3734	18.79	864	28.99	0	0.596	174	72.67		
2014/07/04 15:33	253023	324.089	688.077	68.5996	18.87	864	28.97	0	2.481	316.9	31.04		
2014/07/04 15:34	253024	320.412	684.638	68.2801	18.58	864	28.9	0	0.577	282.2	37.36		
2014/07/04 15:35	253025	317.207	682.185	67.7581	18.66	863	28.87	0	2.114	290.4	35.11		
2014/07/04 15:36	253026	315.317	682.298	67.7577	18.54	864	29.35	0	1.483	293	32.22		

A14

2014/07/04 15:37	253027	312.316	681.113	67.3278	18.48	863	29.43	0	0.889	281.2	44.22		
2014/07/04 15:38	253028	308.876	677.246	67.0207	18.54	863	29.29	0	2.445	286.5	27.37		
2014/07/04 15:39	253029	305.557	673.634	66.9653	18.38	864	29.75	0	1.148	275.8	51.22		
2014/07/04 15:40	253030	302.333	671.466	66.3759	18.42	863	30.22	0	2.091	269.6	35.75	29.54°	320.27°
2014/07/04 15:41	253031	299.856	671.647	65.8724	18.53	863	29.17	0	0.751	184.3	53.86		
2014/07/04 15:42	253032	296.691	669.071	65.4856	18.56	864	28.93	0	0.769	289.6	45.4		
2014/07/04 15:43	253033	292.689	665.54	64.7122	18.66	864	28.95	0	0.467	158.9	33.33		
2014/07/04 15:44	253034	289.722	664.511	64.0124	18.8	863	29.05	0	0.55	254.7	66.02		
2014/07/04 15:45	253035	286.141	661.906	63.3618	18.78	864	29.04	0	0.972	208.9	64.21		
2014/07/04 15:46	253036	283.18	659.148	62.9566	18.65	864	29.09	0	2.166	285.8	28.74		
2014/07/04 15:47	253037	280.378	657.937	62.6006	18.35	863	29.41	0	0.949	280	36.44		
2014/07/04 15:48	253038	278.317	659.927	61.9684	18.35	864	29.51	0	1.111	275.3	24.97		
2014/07/04 15:49	253039	275.286	659.774	61.1827	18.47	863	29.5	0	0.557	131.1	39.84		
2014/07/04 15:50	253040	270.698	654.216	60.3603	18.83	863	29.06	0	0.73	253.6	59.31	28.08°	318.24°
2014/07/04 15:51	253041	266.735	649.22	59.6974	18.99	863	28.46	0	0.64	155.2	61.69		
2014/07/04 15:52	253042	263.576	645.049	59.6544	18.68	863	29.03	0	1.001	248.6	59.41		
2014/07/04 15:53	253043	260.909	643.291	59.6544	18.48	863	29.18	0	1.16	262.1	54.86		
2014/07/04 15:54	253044	258.892	644.362	59.0529	18.45	864	29.06	0	0.673	255	50.46		
2014/07/04 15:55	253045	256.186	643.232	58.8627	18.49	863	28.82	0	1.325	275.1	41.77		
2014/07/04 15:56	253046	251.337	635.253	58.2428	18.43	863	28.61	0	1.761	315.4	28.72		
2014/07/04 15:57	253047	245.919	625.116	58.1568	18.33	863	29.48	0	1.16	277.1	28.89		
2014/07/04 15:58	253048	242.429	621.047	57.5063	18.47	863	29.62	0	1.202	274.6	43.2		
2014/07/04 15:59	253049	239.704	618.465	57.4449	18.53	863	29.09	0	0.926	253.6	58.28		
2014/07/04 16:00	253050	237.107	615.869	57.4449	18.47	863	29.35	0	0.608	241.8	70.42	26.55°	316.3°

A15